**THE EUROPEAN
PHYSICAL JOURNAL C**

Regular Article - Experimental Physics

Precise measurements of W- and Z-boson transverse momentum spectra with the ATLAS detector using pp collisions at $\sqrt{s} = 5.02$ TeV and 13 TeV

ATLAS Collaboration[*]

CERN, 1211 Geneva 23, Switzerland

© The Author(s) 2024

Abstract This paper describes measurements of the transverse momentum spectra of W and Z bosons produced in proton–proton collisions at centre-of-mass energies of $\sqrt{s} = 5.02$ TeV and $\sqrt{s} = 13$ TeV with the ATLAS experiment at the Large Hadron Collider. Measurements are performed in the electron and muon channels, $W \to \ell\nu$ and $Z \to \ell\ell$ ($\ell = e$ or μ), and for W events further separated by charge. The data were collected in 2017 and 2018, in dedicated runs with reduced instantaneous luminosity, and correspond to 255 and 338 pb^{-1} at $\sqrt{s} = 5.02$ TeV and 13 TeV, respectively. These conditions optimise the reconstruction of the W-boson transverse momentum. The distributions observed in the electron and muon channels are unfolded, combined, and compared to QCD calculations based on parton shower Monte Carlo event generators and analytical resummation. The description of the transverse momentum distributions by Monte Carlo event generators is imperfect and shows significant differences largely common to W^-, W^+ and Z production. The agreement is better at $\sqrt{s} = 5.02$ TeV, especially for predictions that were tuned to Z production data at $\sqrt{s} = 7$ TeV. Higher-order, resummed predictions based on DYTURBO generally match the data best across the spectra. Distribution ratios are also presented and test the understanding of differences between the production processes.

Contents

1 Introduction

Measurements of W- and Z-boson production in proton–proton (pp) collisions at the Large Hadron collider (LHC)

[*] e-mail: atlas.publications@cern.ch

Springer

constitute a sensitive test of Quantum Chromodynamics (QCD). The transverse momentum (p_T^V) of the gauge bosons V (W, Z) with respect to the initial proton beam arises from higher order corrections to the leading order Drell–Yan processes, and from non-perturbative effects such as the primordial k_T of the incoming partons. Precise measurements and predictions of the spectra in the region $p_T^V \lesssim 30$ GeV are of particular interest for the measurement of the W-boson mass at hadron colliders [1–4].

Over the last years, theoretical predictions have been calculated including increasingly higher order corrections. These comprise the fixed-order corrections, known up to third order in the strong coupling α_S [5–7], and the resummation of logarithmic terms from soft and collinear emissions using complex formalisms to obtain reliable predictions in the low p_T^V region. Analytic approaches based e.g. on transverse momentum resummation [8] have been extended up to fourth order [9–11]. Parton shower and hadronisation models, such as those implemented in PYTHIA [12], HERWIG [13] or SHERPA [14] provide an alternative approach and predict the complete event topology.

Experimentally, a measurement of the Z-boson p_T spectrum (p_T^Z) is relatively straightforward through the transverse momentum of the pair of charged decay leptons, $p_T^{\ell\ell}$. It was measured previously in pp collisions at the LHC by the ATLAS Collaboration at centre-of-mass energies of $\sqrt{s} = 7$, 8, and 13 TeV [15–17]. Similar measurements were performed by CMS [18–20] and LHCb [21–23].

Even though precise data on p_T^Z spectra exist, these can only be employed in a measurement of the W-boson mass (m_W) through a theoretical modelling of the differences between the W and Z production processes, e.g. those induced by different energy scales, couplings, and flavour and momentum fractions of the initial-state quarks. A direct measurement of the W-boson p_T distribution (p_T^W) is therefore of significant interest to test this modelling and reduce the related uncertainties in a measurement of m_W. While samples of W-boson events are easily selected using the leptonic decays $W \to \ell\nu$, a measurement of the p_T^W spectrum is a much more significant challenge, as the decay neutrino escapes direct detection. The measurement requires the reconstruction of the hadronic system the boson recoils against, the *hadronic recoil*. Additional pp interactions occurring in the same bunch crossing as the signal (pileup), degrade the resolution and constitute the main limitation in this measurement. Consequently, previous measurements at the LHC used relatively small, low pile-up datasets, at $\sqrt{s} = 7$ TeV by ATLAS [24] and at $\sqrt{s} = 8$ TeV by CMS [25], with integrated luminosities of 31 pb^{-1} and 18 pb^{-1}, respectively.

This paper presents measurements of the W- and Z-boson p_T^V distributions in pp collisions, using data collected in dedicated LHC runs with low instantaneous luminosity at centre-of-mass energies of $\sqrt{s} = 5.02$ TeV and $\sqrt{s} = 13$ TeV. These datasets respectively correspond to about 255 and 338 pb^{-1}; two inelastic pp collisions take place on average in the same bunch crossing. The clean experimental conditions optimise the resolution on the hadronic recoil while maintaining high yields of signal events, allowing a precise measurement of the p_T^W distribution. The required calibrations for the detector response to electrons, muons and the hadronic recoil are derived or cross-checked with $Z \to \ell\ell$ events in the same datasets.

The analysis is performed in leptonic final states, where lepton refers to electrons and muons ($\ell = e, \mu$). The W-boson measurement is performed separately for W^- and W^+ production, and p_T^W is unfolded from the hadronic recoil, $\vec{u}_T$, reconstructed in the plane transverse to the beam using charged-particle tracks and energy deposits in the calorimeter. For $Z \to \ell\ell$ events, the p_T^Z spectrum is primarily measured through the dilepton system, $p_T^{\ell\ell}$. An alternative measurement, based on $\vec{u}_T$, is compared to the $p_T^{\ell\ell}$ result and used to validate the reconstruction and measurement techniques. The measurements in the electron and muon channels are combined accounting for correlations of statistical and systematic uncertainties.

2 The ATLAS detector and datasets

2.1 ATLAS detector

The ATLAS detector [26] at the LHC covers nearly the entire solid angle around the collision point.[1] It consists of an inner tracking detector surrounded by a thin superconducting solenoid, electromagnetic and hadronic calorimeters, and a muon spectrometer incorporating three large superconducting air-core toroidal magnets.

The inner-detector system (ID) is immersed in a 2 T axial magnetic field and provides charged-particle tracking in the range $|\eta| < 2.5$. The high-granularity silicon pixel detector covers the vertex region and typically provides four measurements per track, the first hit generally being in the insertable B-layer (IBL) installed before Run 2 [27,28]. It is followed by the SemiConductor Tracker (SCT), which usually provides eight measurements per track. These silicon detectors are complemented by the transition radiation tracker (TRT),

---

[1] ATLAS uses a right-handed coordinate system with its origin at the nominal interaction point (IP) in the centre of the detector and the z-axis along the beam pipe. The x-axis points from the IP to the centre of the LHC ring, and the y-axis points upwards. Polar coordinates (r, ϕ) are used in the transverse plane, ϕ being the azimuthal angle around the z-axis. The pseudorapidity is defined in terms of the polar angle θ as $\eta = -\ln\tan(\theta/2)$ and is equal to the rapidity $y = \frac{1}{2}\ln\left(\frac{E+p_z}{E-p_z}\right)$ in the relativistic limit. Angular distance is measured in units of $\Delta R \equiv \sqrt{(\Delta y)^2 + (\Delta \phi)^2}$.

which enables radially extended track reconstruction up to $|\eta| = 2.0$. The TRT also provides electron identification information based on the fraction of hits (typically 30 in total) above a higher energy-deposit threshold corresponding to transition radiation.

The calorimeter system covers the pseudorapidity range $|\eta| < 4.9$. Within the region $|\eta| < 3.2$, electromagnetic calorimetry is provided by barrel and endcap high-granularity lead/liquid-argon (LAr) calorimeters, with an additional thin LAr presampler covering $|\eta| < 1.8$ to correct for energy loss in material upstream of the calorimeters. Hadronic calorimetry is provided by the steel/scintillator-tile calorimeter, segmented into three barrel structures within $|\eta| < 1.7$, and two copper/LAr hadronic endcap calorimeters. The solid angle coverage is completed with forward copper/LAr and tungsten/LAr calorimeter modules optimised for electromagnetic and hadronic energy measurements respectively.

The muon spectrometer (MS) comprises separate trigger and high-precision tracking chambers measuring the deflection of muons in a magnetic field generated by the superconducting air-core toroidal magnets. The field integral of the toroids ranges between 2.0 and 6.0 Tm across most of the detector. Three layers of precision chambers, each consisting of layers of monitored drift tubes, cover the region $|\eta| < 2.7$, complemented by cathode-strip chambers in the forward region, where the background is highest. The muon trigger system covers the range $|\eta| < 2.4$ with resistive-plate chambers in the barrel, and thin-gap chambers in the endcap regions.

The luminosity is measured mainly by the LUCID–2 [29] detector that records Cherenkov light produced in the quartz windows of photomultipliers located close to the beampipe.

Events are selected by the first-level trigger system implemented in custom hardware, followed by selections made by algorithms implemented in software in the high-level trigger [30]. The first-level trigger accepts events from the 40 MHz bunch crossings at a rate below 100 kHz, which the high-level trigger further reduces in order to record complete events to disk at about 1 kHz.

A software suite [31] is used in data simulation, in the reconstruction and analysis of real and simulated data, in detector operations, and in the trigger and data acquisition systems of the experiment.

2.2 Data sets

The analysis is conducted using datasets corresponding to integrated luminosities of $254.9 \pm 2.6 \, pb^{-1}$ at $\sqrt{s} = 5.02$ TeV and $338.1 \pm 3.1 \, pb^{-1}$ at $\sqrt{s} = 13 \, pb^{-1}$. The luminosity determination for the 5.02 TeV data sample was carried out in a similar way to that described for the low-instantaneous-luminosity 13 TeV dataset in Ref. [32], and

has similar uncertainties. They were collected in 2017 and 2018 during dedicated LHC low pile-up runs with an average number of pp interactions, $\langle \mu \rangle$, of about two, as compared to $\langle \mu \rangle \sim 34$ for the nominal LHC Run 2 operation between 2015 and 2018. To fully exploit these conditions, the thresholds applied to suppress noise in the reconstruction of clusters of energy in the calorimeters were lowered, optimising the reconstruction of the hadronic recoil as described in Sect. 4. The data was collected with triggers that require at least one electron or muon with transverse momentum thresholds of $p_T^e > 15$ GeV and $p_T^\mu > 14$ GeV, respectively [30,33,34]. Loose identification criteria are applied at the trigger level for electron or muon candidates.

2.3 Signal and background simulation

Samples of Monte Carlo (MC) simulated events are used to model the signal and background processes. All MC samples were processed through the full ATLAS detector simulation [35] based on GEANT4 [36] using settings specific to the low pile-up run conditions. The effects of pile-up collisions in the same or neighbouring bunch crossings were included in the MC simulation by overlaying inelastic pp interactions produced using PYTHIA 8 with the NNPDF2.3LO set of parton distribution functions (PDFs) [37] and the A3 set of tuned parameters [38].

The main signal event samples for W and Z production were generated using the POWHEG event generator at next-to-leading order in QCD (NLO) [39–42] using the CT10 PDF [43], interfaced to PYTHIA 8 [12] using the AZNLO tune [15]. These POWHEG+PYTHIA 8 samples were interfaced to PHOTOS++[44] to simulate the effect of final-state QED radiation. The effective sample size is typically 10–20 times larger than the data to minimise the impact of MC statistical uncertainties. Alternative signal samples were prepared with SHERPA 2.2.1 ($\sqrt{s} = 13$ TeV) and 2.2.5 ($\sqrt{s} = 5.02$ TeV) [14] using the NNPDF3.0 NNLO PDFs [45] and merging matrix element calculations from Comix [46] and OPENLOOPS [47–49] for $V+0, 1, 2$ partons at NLO accuracy with $V+3, 4$ partons at leading order (LO) accuracy in the MEPS@NLO scheme [50–54]. These samples are used to evaluate the uncertainty arising from the choice of the program used to simulate the signal events. The W and Z samples are normalised to next-to-next-to-leading (NNLO) calculations performed using the DYTURBO [55] program, an optimised version of DYNNLO [56,57] using the MMHT2014 NNLO PDF set [58]. A conservative total uncertainty of 5% is taken as normalisation uncertainty in background predictions or control regions, covering the uncertainties in PDFs, α_S and missing higher order corrections.

Backgrounds from top-antitop-quark pair ($t\bar{t}$) production and single-top-quark production (Wt associated production, t-channel, s-channel) were generated with POWHEG+

PYTHIA 8 [59] and normalised to the NNLO predictions with resummation at next-to-next-to-leading-logarithmic (NNLL) accuracy [60–66]. Diboson production $VV(V = W, Z)$ was generated with SHERPA in all decay channels with at least one real lepton in the final state and treated as background [67].

3 Lepton and event selection

This analysis relies on the reconstruction and selection of electrons and muons. The calibrations and efficiency measurements used for the low pile-up datasets are briefly summarised in this section. The methodology closely follows that established for the full ATLAS Run 2 dataset [68,69], referred to as the high pile-up dataset. A full set of corrections are determined from the low pile-up datasets. However, where possible, corrections determined from the large high pile-up dataset are used instead to benefit from their better statistical precision. Corrections derived from the high pile-up dataset are complemented by additional corrections or uncertainties reflecting the extrapolation to the low pile-up regime.

The W- and Z-boson event selections are also described in this section, as well as the determination of the primary vertex reconstruction efficiency. The hadronic recoil, $\vec{u}_\mathrm{T}$, is a detector-level measure of p_T^W, and is used to infer the transverse momentum of the decay neutrino. Its reconstruction and calibration are specific to this analysis and are described in Sect. 4.

3.1 Electrons

Electron candidates are reconstructed from clusters of energy deposited in the electromagnetic calorimeter and associated with at least one track in the ID. Electrons are required to be within the coverage of the ID and the precision region of the EM calorimeter, $|\eta| < 2.47$. Electrons in the transition region between the barrel and endcap calorimeters, $1.37 < |\eta| < 1.52$, are excluded. Electron candidates are required to have a transverse momentum of $p_\mathrm{T}^\ell > 25\,\mathrm{GeV}$ and pass the *Medium* likelihood identification requirements [68]. They are also required to be isolated from nearby activity, as measured by tracks in a cone of size $\Delta R < 0.2$ around the candidate. The scalar sum of the p_T of these tracks is required to be less than 10% of the electron p_T^ℓ and may not exceed 5 GeV for electrons with $p_\mathrm{T}^\ell > 50\,\mathrm{GeV}$, i.e. $p_\mathrm{T}^{\mathrm{cone20}}/\min(p_\mathrm{T}^\ell, 50\,\mathrm{GeV}) < 0.1$.

Corrections and uncertainties in the electron energy calibration are estimated by using a combination of simulation-based and data-driven procedures as described in Ref. [68]. The energy scale and resolution differences between data and simulation are determined in the low pile-up datasets using

$Z \to ee$ decays and the statistical uncertainties are dominant. Smaller systematic uncertainties on the simulation of the material and on the relative calibration of the calorimeter layers are taken from the analysis of the high pile-up dataset instead.

Corrections to the electron trigger, identification and isolation efficiencies are determined separately in the 13 and 5.02 TeV low pile-up data from Z-boson events using tag-and-probe methods [68]. The electron reconstruction efficiency corrections are instead extrapolated from the high pile-up dataset.

3.2 Muons

The muon reconstruction is performed independently in the ID and in the MS, and a muon candidate is formed from the combination of a muon spectrometer track with an ID track. The muon candidates are required to have an absolute pseudorapidity of $|\eta| < 2.4$, a transverse momentum of $p_\mathrm{T}^\ell > 25\,\mathrm{GeV}$ and to satisfy the *Medium* identification criteria [69]. Muons are required to be isolated from nearby activity with the same criterion as electrons.

Corrections are applied to the reconstructed muon momentum in simulation to precisely match the data. The corrections to the simulated momentum resolution and momentum scale are determined using both $Z \to \mu\mu$ and $J/\psi \to \mu\mu$ events in the high pile-up dataset as described in Ref. [69]. They are cross-checked with the low pile-up dataset and good agreement is found. A dedicated correction for charge-dependent momentum biases in data is determined in situ and applied as a function of muon η using a combination of different methods [69,70]. These correlated systematic biases can be introduced either by detector deformations to which the alignment procedure has little sensitivity or by the procedure used to determine the alignment parameters [71].

The efficiency of the selection criteria for muon candidates is measured using tag-and-probe methods [69] in $Z \to \mu\mu$ events separately for the 13 and 5.02 TeV data. Efficiency correction factors for muon trigger and isolation are evaluated as a function of muon η and p_T in the low pile-up dataset with a precision limited by the size of the $Z \to \mu\mu$ data samples. The muon reconstruction efficiency correction is instead determined with the high pile-up dataset and extrapolated to low pile-up.

3.3 Primary vertex reconstruction

Primary vertices are reconstructed requiring at least two charged-particle tracks [72] and the hard-scatter vertex is chosen as the one with the largest sum of squared track transverse momenta. Lepton candidates are required to originate from this vertex. The significance of the track's transverse impact parameter calculated relative to the beam line,

$|d_0/\sigma_{d_0}|$, must be smaller than three for muons and smaller than five for electrons. Furthermore, the longitudinal impact parameter, z_0 (the difference between the z-coordinate of the point on the track at which d_0 is defined and the longitudinal position of the primary vertex), is required to satisfy $|z_0 \cdot \sin(\theta)| < 0.5$ mm.

The efficiency of this requirement in $Z \rightarrow \ell\ell$ events is generally above 99% and included in the tag-and-probe procedures described above. However, for W-boson events at low p_T, the reconstruction of the correct primary vertex is more challenging as it requires at least one additional charged-particle track from hadronic activity in addition to the lepton. A dedicated measurement of this efficiency is therefore derived. It is performed in $Z \rightarrow \ell\ell$ events as function of the number of reconstructed additional tracks, i.e. excluding the leptons, and the boson p_T. The data measurement can then be applied to the $W \rightarrow \ell\nu$ simulation. The vertex reconstruction inefficiency in W-boson events with $p_T^W < 5$ GeV at $\sqrt{s} = 5.02$ TeV (13 TeV) is found to be about 5% (3%) for the electron channels and 3% (2%) for the muon channels. It decreases towards higher p_T^W, and asymptotically reaches about 1% in the electron channel and 0.5% in the muon channel. The inefficiency is larger in the electron channels because bremsstrahlung complicates the track reconstruction and track-to-vertex association. The modelling of the soft activity at low W boson p_T is the main source of uncertainty on the vertex efficiency and its effect is estimated by observing the closure between different generators, as discussed in Sect. 6.2.

3.4 Selection of W- and Z-boson candidate events

The $W \rightarrow \ell\nu$ event selection requires exactly one reconstructed and isolated electron or muon satisfying the criteria described in Sects. 3.1 or 3.2, respectively. Events with additional leptons of the same flavour with transverse momentum $p_T^\ell > 20$ GeV are discarded to reduce the Z background; the identification requirement for these veto leptons is loosened with respect to the nominal selection to make the veto more effective. There are no requirements on the number of leptons with flavour different than the channel under study. The missing transverse momentum, $\vec{p}_T^{\,\text{miss}}$, and its magnitude E_T^{miss} are defined from $\vec{p}_T^\ell$ and $\vec{u}_T$ following $\vec{p}_T^{\,\text{miss}} = -\left(\vec{p}_T^\ell + \vec{u}_T\right)$, and represent a measure of the transverse momentum of the neutrino. The background from QCD multijet events is reduced by the requirement $E_T^{\text{miss}} > 25$ GeV. Furthermore, the W-boson transverse mass $m_T = \sqrt{2p_T^\ell E_T^{\text{miss}}(1 - \cos \Delta\phi_{\ell\nu})}$ must exceed 50 GeV, where $\Delta\phi_{\ell\nu}$ is the azimuthal angle between $\vec{p}_T^\ell$ and $\vec{p}_T^{\,\text{miss}}$. After all selections, a total number of 7.1×10^5 (2.2×10^6) W-boson candidate events are selected in the $W \rightarrow e\nu$ channel and 7.5×10^5 (2.2×10^6) in the $W \rightarrow \mu\nu$ channel for the 5.02 TeV (13 TeV) data.

$Z \rightarrow \ell\ell$ events are selected by requiring exactly two same-flavour, opposite-charge leptons. The same reconstruction and isolation criteria as discussed above are applied, and the lepton-pair invariant mass is restricted to the range $66 < m_{\ell\ell} < 116$ GeV. A total of 5.2×10^4 (1.7×10^5) Z-boson candidates are found in the electron channel and 7.0×10^4 (2.1×10^5) in the muon channel for the 5.02 TeV (13 TeV) data.

4 Hadronic recoil reconstruction and calibration

The final state of a $W \rightarrow \ell\nu$ or $Z \rightarrow \ell\ell$ event naturally separates into the leptonic system and the associated QED radiation, and the hadronic recoil, $\vec{u}_T$, defined in the plane transverse to the beam from the remaining reconstructed particles in the event. Up to the detector resolution, the transverse momentum of the hadronic recoil is equal in magnitude to the vector boson transverse momentum and points in the opposite direction, $\vec{u}_T = -\vec{p}_T^V$.

In $Z \rightarrow \ell\ell$ events, the Z-boson transverse momentum can be estimated from both the lepton pair $p_T^{\ell\ell}$ and u_T. The well-measured dilepton system can thus be used to calibrate the hadronic recoil response, and the unfolded $p_T^{\ell\ell}$ distribution provides a cross-check of the p_T^Z spectrum measured from u_T.

4.1 Hadronic recoil reconstruction

The hadronic recoil was used successfully in ATLAS analyses with $\sqrt{s} = 7$ TeV data [24,70]. For these measurements, the reconstruction was based on calorimetric energy deposits reconstructed using a topological clustering algorithm [73]. In this analysis, the hadronic recoil is reconstructed from *Particle Flow Objects* (PFOs) [74,75] that combine information from ID tracks and the calorimeters in an optimal way and avoid double counting. Compared to the calorimeter-based measurement, the particle flow technique improves the recoil resolution by 3% at low p_T^V, increasing to 15% at $p_T^V \approx 50$ GeV.

The recoil vector $\vec{u}_T$ is computed from the vector sum of all charged and neutral PFO momenta. To reject pile-up contributions, charged PFOs are required to be associated with the same primary vertex as the W lepton candidate. PFOs within $\Delta R = 0.2$ around identified electrons and muons are not included in the recoil, to avoid energy deposits originating from charged leptons and accompanying photons. This procedure also removes small underlying event and pile-up contributions. To compensate this bias, the PFO momentum measured in a region at the same η as the lepton, and randomly chosen ϕ, with the constraint of being separated from the lepton and recoil directions by $\Delta\phi > 0.4$, is rotated to the lepton axis and added to the recoil.

The resolution of $u_{\rm T}$ primarily depends on the event activity variable $\Sigma E_{\rm T}$, the scalar sum of the transverse energies of all PFOs included in the recoil. The quantity $\Sigma \bar{E}_{\rm T} = \Sigma E_{\rm T} - u_{\rm T}$ is a modified event activity variable with reduced correlation to the vector boson dynamics, and that mostly represents the underlying event and pile-up. Events are characterised by the vector boson transverse momentum and $\Sigma \bar{E}_{\rm T}$.

In $Z \to \ell\ell$ events, the projections of the hadronic recoil on the axes parallel and perpendicular to the momentum of the lepton pair are denoted $u_{\parallel}$ and $u_{\perp}$, respectively. These projections are used to calibrate the hadronic recoil scale and resolution. The perpendicular component $u_{\perp}$ is expected to have a mean of zero and a width given by the resolution. The sum of $u_{\parallel}$ and $p_{\rm T}^{\ell\ell}$ is also called *bias*,

$$b = u_{\parallel} + p_{\rm T}^{\ell\ell}, \tag{1}$$

and would ideally be close to zero. However, $b > 0$ is observed on average, due to particles escaping detection, energy losses in passive detector material and the non-compensating nature of the calorimeters.

4.2 Hadronic recoil calibration

The hadronic recoil scale, resolution and direction need to be calibrated before the measurement is performed. The $Z \to \ell\ell$ final state is the primary reference, since the final-state kinematics are fully determined through the precise reconstruction of the decay lepton pair. The calibration derived from the Z-boson sample at a given value of dilepton transverse momentum $p_{\rm T}^{\ell\ell}$, is applied to the $W \to \ell\nu$ simulation at the same value in the generated transverse momentum $p_{\rm T}^{{\rm true},V}$ of the W-boson. This replacement is possible as the lepton resolution is better than that of the hadronic recoil by about one order of magnitude. The corrections are derived in four sequential steps:

- the modelling of the modified event activity $\Sigma \bar{E}_{\rm T}$ in the signal simulation is corrected, separately in W- and Z-boson events;
- the simulated azimuthal distribution of the recoil is corrected to that observed in data;
- the simulated recoil scale and core resolution are corrected to those observed in data, using the $u_{\perp}$ and $u_{\parallel}$ projections in Z-boson events;
- residual corrections for non-Gaussian resolution tails are derived in data and applied to the simulation.

All corrections are obtained separately for $\sqrt{s} = 5.02$ TeV and $\sqrt{s} = 13$ TeV data. As the recoil response is independent of the decay lepton flavour, the $Z \to ee$ and $Z \to \mu\mu$ samples are merged to derive the corrections. The corrections are then applied to the $W \to \ell\nu$ MC samples, and the closure

of the calibration is verified by application to $Z \to \ell\ell$ samples. Small differences in the hadronic activity between W and Z bosons, for example induced by the different initial-state quark flavours and momentum fractions, are accounted for by dedicated corrections or systematic uncertainties, as explained at the end of this section.

Modelling of $\Sigma \bar{E}_{\rm T}$

Three event weights are obtained for the POWHEG+PYTHIA 8 MC samples to model the observed $\Sigma \bar{E}_{\rm T}$ distribution and its correlation with the $p_{\rm T}^V$ distribution. A first two-dimensional reweighting of the ($\Sigma \bar{E}_{\rm T}$, $p_{\rm T}^{\ell\ell}$) distribution is derived from the ratio of data and simulation for the Z-boson sample. The weights are applied to the W simulation as a function of $p_{\rm T}^{{\rm true},V}$, as explained above. After this correction, the $\Sigma \bar{E}_{\rm T}$ distributions in W-boson data and simulation agree at the percent level.

The residual disagreement in the W-boson sample remaining after the first reweighting using the Z-boson data, is removed using a second event weight obtained from the W-boson sample itself. This correction is performed separately for each charge, as a function of $\Sigma \bar{E}_{\rm T}$ and in bins of $u_{\rm T}$ after a first calibration of $u_{\rm T}$ in the simulation using the resolution and response corrections discussed below.

The application of these weights to the Z and W samples modifies the generated transverse momentum spectrum of the bosons in the simulation. The initial spectrum is restored using a third, one-dimensional weight as a function of $p_{\rm T}^{{\rm true},V}$. The total weight applied to simulated $W \to \ell\nu$ events is the product of the three weights described above. Only the first and third weight are applied to Z events. The whole procedure is equivalent to making a reweighting in slices of $p_{\rm T}^V$ (and then $u_{\rm T}$ for $W \to \ell\nu$ events), which is why it is not required to have the same distribution of $p_{\rm T}^V$ in data and in simulation. The total number of events is preserved, as only shapes are used.

A closure test is performed using simulated SHERPA Z and W events as pseudo-data, to verify that the correlation between $\Sigma \bar{E}_{\rm T}$ and $p_{\rm T}^{{\rm true},V}$ in POWHEG+PYTHIA8 is corrected to that present in SHERPA. A good closure is observed and the small residual non-closure is taken as a systematic uncertainty. This uncertainty also allows to check that in this procedure, there is no dependence on how well the distribution of $p_{\rm T}^V$ is modelled in POWHEG+PYTHIA8, as the two generators differ significantly in their predicted $p_{\rm T}^V$ spectra.

Azimuthal correction

The azimuthal direction of the recoil, $\phi(\vec{u_{\rm T}})$, is not uniformly distributed due to effects not fully modelled by the simulation, such as non-uniformity in the calorimeter response, the calorimeter mechanical deformation, the beam displacement

from the nominal beam line in (x, y), or the beam-crossing angle. An empirical correction is obtained from the differences between the mean values of the x and y components of the recoil in Z events in data and in the simulation ($\langle u_x \rangle$ and $\langle u_y \rangle$). A small dependence on $\Sigma \bar{E}_T$ is observed and included in the correction. The components of the recoil in the simulation are then corrected accordingly.

The impact of this stage of the calibration on the measured u_T distribution in W simulated events is at most 0.5%, giving confidence that the correlation between the direction and the magnitude of the recoil is weak.

Resolution and response corrections

The data-to-MC resolution correction for $u_\perp$ is derived as a ratio of $\sigma(u_\perp)$ values following

$$r(\Sigma \bar{E}_T, p_T^{\ell\ell}) = \frac{\sigma_{u_\perp}(\Sigma \bar{E}_T, p_T^{\ell\ell})^{\text{data}}}{\sigma_{u_\perp}(\Sigma \bar{E}_T, p_T^{\ell\ell})^{\text{MC}}}, \qquad (2)$$

where $\sigma_{u_\perp}$ is derived from Gaussian fits to the $u_\perp$ distributions in $Z \rightarrow \ell\ell$ events, in bins of $\Sigma \bar{E}_T$ and $p_T^{\ell\ell}$. The distribution of $u_\perp$ in the W-boson simulation is then corrected following

$$u_\perp^{\text{MC,corr}} = u_\perp^{\text{MC}} \cdot r(\Sigma \bar{E}_T, p_T^{\text{true},V}). \qquad (3)$$

The data-to-MC corrections for $u_\parallel$ (r') use the standard deviation and mean of the *bias* defined in Eq. (1) that relate to the resolution and scale, respectively. The corrections are extracted in $Z \rightarrow \ell\ell$ events, $r'(\Sigma \bar{E}_T, p_T^{\ell\ell})$, and transferred to the W-boson MC, $r'(\Sigma \bar{E}_T, p_T^{\text{true},V})$, as:

$$\begin{aligned} u_\parallel^{\text{MC,corr}} &= \langle u_\parallel^{\text{data}} \rangle + (\langle b^{\text{data}} \rangle - \langle b^{\text{MC}} \rangle) \cdot r' \\ &\quad + \left(u_\parallel^{\text{MC}} - \langle u_\parallel^{\text{data}} \rangle \right) \cdot r', \end{aligned} \qquad (4)$$

where all quantities are defined in bins of $\Sigma \bar{E}_T$ and $p_T^{\ell\ell}$ or $p_T^{\text{true},V}$.

Tail correction

The resolution corrections discussed above only correct the core Gaussian parts of the $u_\parallel$ and $u_\perp$ distributions. Non-Gaussian effects appear in the tails, mostly driven by hadronic activity out of the detector acceptance. A final step in the recoil calibration therefore corrects the resolution tails in simulation to that in data after applying all previous corrections. The correction is derived in bins of $p_T^{\ell\ell}$ from the cumulants of the $u_\parallel$ and $u_\perp$ distributions in data and simulation with an inverse transform sampling (*Smirnoff transform*) [76]. The full transformation is parameterised by empirical functions with two (four) parameters for $u_\perp$ ($u_\parallel$). The transformation gives corrected values as of $u_\parallel$ and $u_\perp$ as a function of these

same variables for each event. For $u_\perp$ this results in a symmetric stretching around zero and for $u_\parallel$ in an asymmetric stretching around the median of the distribution.

Summary of recoil calibration

Figure 1 shows the comparison of $\sigma_{u_\perp}$ and $\langle b \rangle$ as a function of $p_T^{\ell\ell}$ in the $Z \rightarrow \mu\mu$ simulated and data samples. Using PFOs instead of calorimeter-based inputs only improves the recoil resolution, *e.g* at 13 TeV $\sigma_{u_\perp}$ decreases from ≈ 12.1 GeV to ≈ 10.5 GeV around $p_T^V \approx 50$ GeV, once it is calibrated and corrected for the scale. Good closure of the calibration is observed. Similar results are obtained in the $Z \rightarrow ee$ samples. The uncertainty in the extrapolation from the Z to the W is estimated from the differences between the standard deviation and mean of the $u_\perp$ and $u_\parallel$ distributions in the simulation, at given values of $(\Sigma \bar{E}_T, p_T^{\text{true},V})$, to derive alternative sets of resolution and response corrections r and r'.

A final systematic uncertainty in the recoil calibration is estimated by using SHERPA signal events as pseudo data in the calibration procedure. The POWHEG+PYTHIA 8 sample is calibrated to SHERPA, the full analysis described in Sect. 6 is performed and the difference between the measured p_T^V distribution and the generated spectrum gives the closure of the correction. To simplify the procedure and avoid double-counting the extrapolation from Z to W, the calibration of each process uses only the corresponding signal sample from both event generators. The p_T^V spectrum of SHERPA is also reweighted to POWHEG+PYTHIA 8 to avoid double-counting the unfolding prior uncertainty, i.e. the effects tested are residual differences in the simulation of hadronic jet production beyond the hardest emission, the underlying event, fragmentation and hadronisation. The difference between the two generators in observables relevant to the description of the recoil is larger than the one between data and POWHEG+PYTHIA 8 in Z events, which gives confidence that this uncertainty component is not accidentally underestimated.

5 Background estimates and event yields

5.1 Background in the $W \rightarrow \ell\nu$ selection

Background contributions from single-boson and diboson production (electroweak background) and $t\bar{t}$ and single-top-quark production (top-quark background) are directly estimated from the MC simulated samples described earlier. They are dominated by $W \rightarrow \tau\nu$ events with $\tau \rightarrow \ell\nu\nu$ at low u_T and top-quark pair production at higher u_T. In the electron channels there is an additional background contribution from $W \rightarrow e\nu$ events where the reconstructed electron charge is mismeasured.
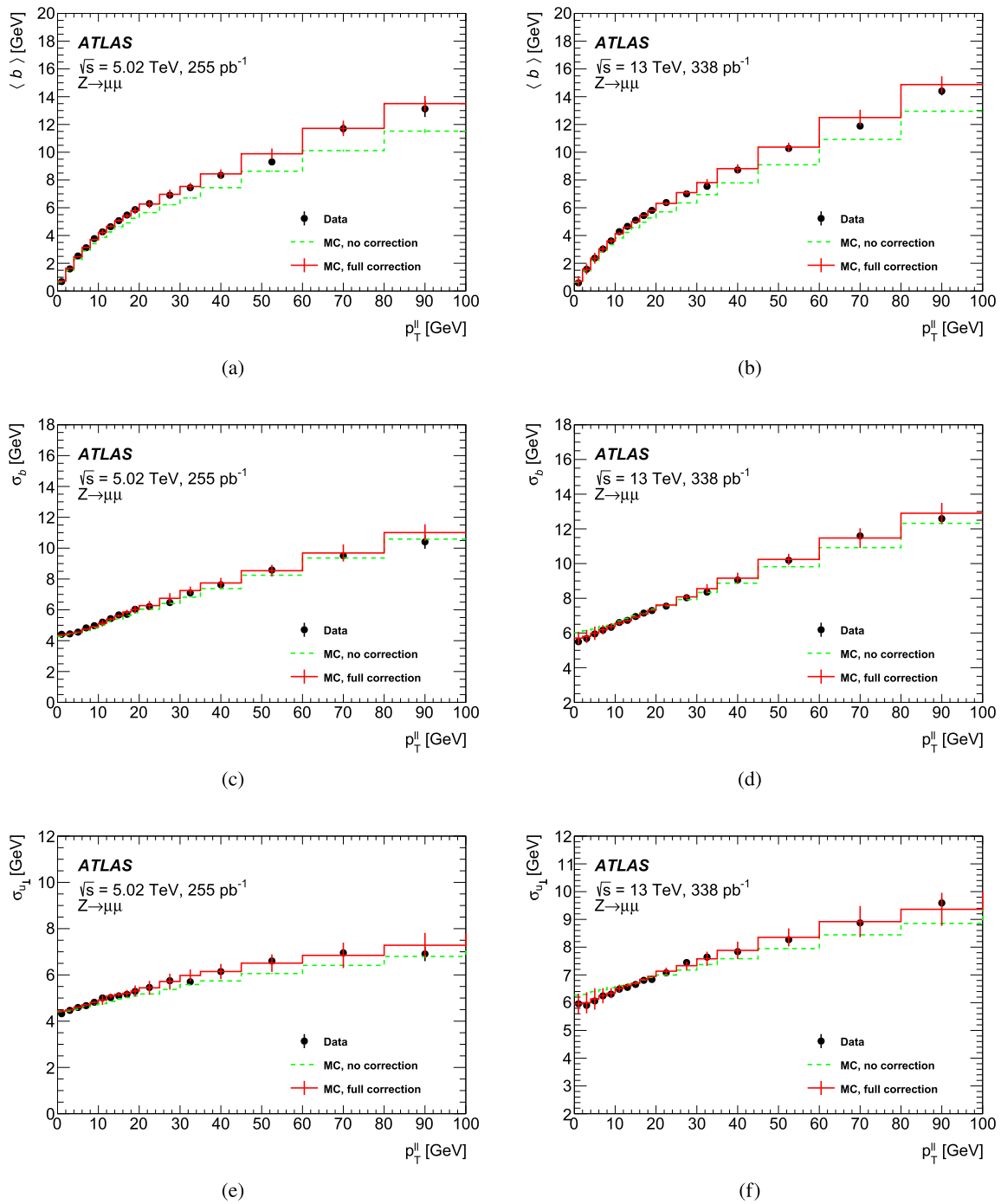
(a)

(b)

(c)

(d)

(e)

(f)

Fig. 1 Mean value for the bias $b = u_\parallel + p_T^{\ell\ell}$ at **a** $\sqrt{s}$ = 5.02 TeV and **b** $\sqrt{s}$ = 13 TeV, standard deviation of the bias at **c** $\sqrt{s}$ = 5.02 TeV and **d** $\sqrt{s}$ = 13 TeV, and standard deviation of $u_\perp$ at **e** $\sqrt{s}$ = 5.02 TeV and **f** $\sqrt{s}$ = 13 TeV in $Z \to \mu\mu$ events. Data (black dots) are compared to the simulation before (green dotted histogams) and after (red histograms) correction. The values are shown as a function of $p_T^{\ell\ell}$. Error bars show the sum of statistical uncertainties and systematic uncertainties from recoil calibration and from the choice of event generator (the difference between SHERPA and POWHEG+PYTHIA 8)

Background from QCD multijet (MJ) production cannot be reliably simulated and has to be derived from data. Depending on the lepton flavour, the MJ background has significant contributions from leptons produced in semileptonic decays of heavy quarks, pion and kaon decays, or photon conversions, and is referred to as fake leptons below. The multijet yields in the electron and muon selections of the W-boson analysis are estimated separately for positively and negatively charged samples. As multijet production is concentrated at lower values of p_T^ℓ, E_T^{miss} and m_T as compared to the signal, this background is estimated with a template fit in these kinematic distributions in a phase-space region with relaxed E_T^{miss} and m_T selections, called the *fit region*. The p_T^ℓ, E_T^{miss} and m_T templates in the fit region for the $W \to \ell\nu$ signal and electroweak and top-quark backgrounds are obtained using simulation. The multijet templates are built from events passing the same kinematic selections as the nominal selection except that the lepton isolation requirement is inverted. In the final step, the multijet yields in the signal region are determined by multiplying the fit region yields by a transfer factor that corrects for the acceptance of the E_T^{miss} and m_T selections and the impact of the inverted isolation requirements needed to extract the multijet background templates.

The multijet yield is estimated three times using the p_T^ℓ, E_T^{miss} and m_T distributions separately. The three results are found to be compatible, and the final yield estimate is derived from their unweighted mean, neglecting the correlations. As the shape of the multijet templates depends on the anti-isolation criterion, mutually exclusive intervals in the isolation variable are chosen to create statistically independent multijet templates. These samples are designed to be progressively closer to the signal-candidate selection and are used to study the dependence of the multijet extraction on the considered isolation.

Several improvements are included in this background estimate with respect to a similar method described in Ref. [70]. In particular, the removal of all energy in the cone around lepton candidates from the hadronic recoil calculation, as described in Sect. 4.1, is problematic for the case where leptons are required to fail the isolation selection. The correct properties in the multijet-enriched sample are restored by adding back a fraction of the hadronic activity around the lepton candidate and recalculating the kinematic variables u_T, E_T^{miss}, and m_T accordingly. Another significant improvement on the MJ yield estimate is the use of MJ templates in the fits that have their shapes corrected. This correction is achieved by combining the shapes from different anti-isolation intervals to extrapolate into the fit region. Instead of repeating the template fit in different anti-isolation intervals, it is carried out only once for a given kinematic distribution, and the corresponding dependence of the measured multijet yield is entirely located in the transfer factor. Example results of template fits in the electron and muon channels

are shown in Fig. 2. The disagreement observed in Fig. 2e is not a major concern, since the estimation of the multijet yield using m_T is always still consistent with the ones using p_T^ℓ and E_T^{miss}. In the final signal selection, the background-dominated region ($m_T < 50$ GeV) is removed. In Fig. 3, the transfer factors accounting for the efficiency of the kinematic cuts and the isolation requirements to extrapolate from the *fit region* to the signal region are shown as a function of anti-isolation intervals. The extrapolation was also tested with alternative function forms, which produced estimations of yields consistent with the linear extrapolation within the yield uncertainty.

The final MJ background yield and total uncertainty is presented in Table 1. The dominant MJ yield uncertainties arise from: the statistical uncertainty from the limited data and MC events in the fit region, the linear extrapolation procedure to the average isolation value in the signal region, and the possible mis-modelling of the jet activity in the anti-isolated regions. The uncertainty arising from the latter effect is studied by categorising events in broad bins of u_T.

Corrections to the shape of the multijet background contributions and corresponding uncertainties in the distributions used in the final measurement are estimated with a similar procedure. The MJ kinematic distributions in the signal region are determined by linearly extrapolating the shape of the distributions observed in the mutually exclusive anti-isolation intervals into the isolated region. Uncertainties in the extrapolated distributions are dominated by the statistical uncertainty. The resulting multijet background distribution is propagated to the final analysis. A smoothing is applied to the MJ u_T spectra for $u_T > 100$ GeV to avoid large fluctuations due to low event counts in the data samples.

The estimated multijet background fractions in the 5.02 TeV dataset represent 0.8 and 0.1% of the total number of observed W^- candidate events in the electron and muon channels, respectively. In the 13 TeV dataset the corresponding fractions are larger at 2.9 and 0.6% because the gluon-induced multijet production rises faster with $\sqrt{s}$ than the quark-induced signal. For W^+ candidate events the background yields are found to be similar to the W^- channels within uncertainties, and the relative fractions are lower by the size of the W^+/W^- cross-section ratio. The different sources of the MJ uncertainty components in yield and shape are treated as correlated across the channels, while the statistical uncertainties are uncorrelated.

The total impact of the uncertainties in the background estimation on the cross-section measurements is shown in Figs. 24 and 25 in Appendix A, and is at the level of 0.1–1% in the low $p_T^W < 63$ GeV region, depending on the channel.
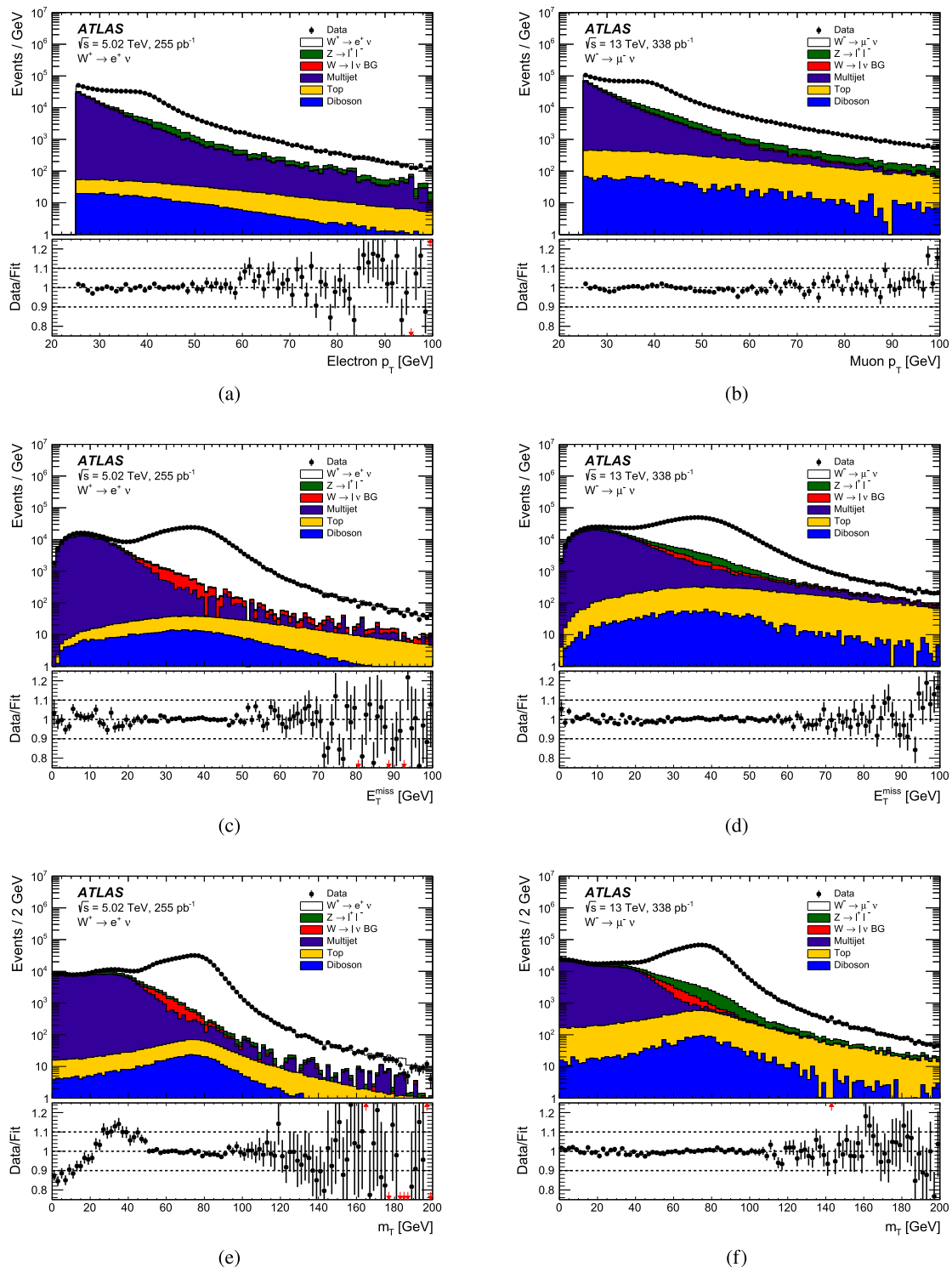
Fig. 2 Distributions of **a**, **b** p_T^ℓ, **c**, **d** E_T^{miss} and **e**, **f** m_T in a phase-space region without E_T^{miss} and m_T selections (*fit region*) used to extract multijet yields in template fits in the $W^+ \rightarrow e^+\nu$ in the **a**, **c**, **e** $\sqrt{s} = 5.02$ TeV dataset and $W^+ \rightarrow \mu^+\nu$ in the **b**, **d**, **f** $\sqrt{s} = 13$ TeV dataset. Multijet templates are derived from the data combining the shape information from different anti-isolation intervals. The data are compared to the simulation including signal and background contributions. The category $W \rightarrow \ell\nu$ BG refers to background from $W \rightarrow \tau\nu$ and charge misidentification in the electron channels
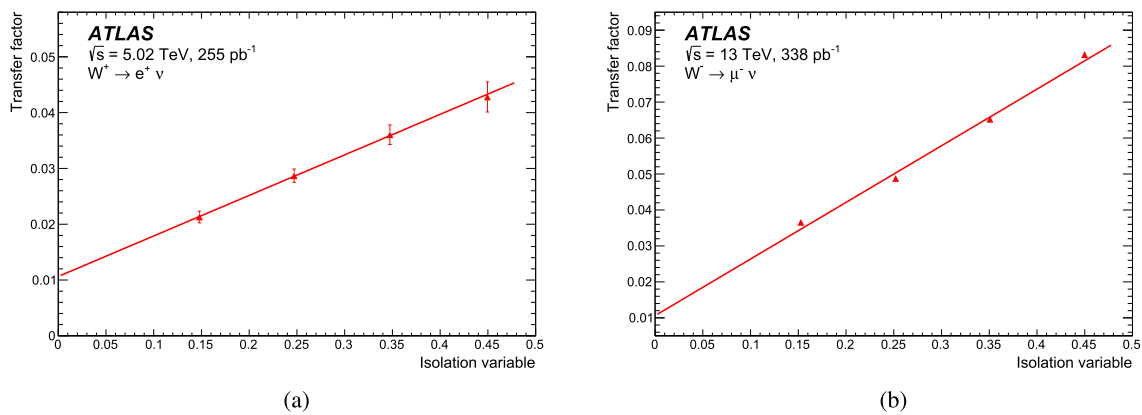
(a)

(b)

Fig. 3 Illustration of the multijet yield transfer factors to account for the different kinematic selections in E_T^{miss} and m_T and isolation requirements from the *fit region* to the signal region. The transfer factors are shown as a function of the lower bound of the range of the isolation variable $p_T^{cone20}/\min(p_T^\ell, 50\,\text{GeV})$ used to define the anti-isolation inter-

vals, for **a** the $W^+ \to e^+\nu$ channel at $\sqrt{s} = 5.02\,\text{TeV}$ and **b** the $W^- \to \mu^-\nu$ channel at $\sqrt{s} = 13\,\text{TeV}$. The data point are reasonably described by the linear fits indicated by the solid lines. The uncertainties in the data points are statistical only

5.2 Background in the $Z \to \ell\ell$ selection

As in the $W \to \ell\nu$ analysis, the electroweak and top-quark backgrounds are directly estimated from the MC simulated samples described earlier. They are dominated by diboson and top-quark pair production at higher u_T, but very small overall.

A data-driven two-dimensional sideband method is employed to estimate MJ background. The signal region A is complemented by three orthogonal control regions B, C, and D enriched in events produced from background processes with fake leptons. For both channels, events in region B have the nominal requirements except that the subleading lepton is required to fail the isolation selection. For events to be registered in region C in the electron channel, the primary requirement is to fail the *Medium* identification requirement, but pass the *Loose* criteria. In addition, only same-charge pairs are selected and the p_T^ℓ requirement is loosened to 20 GeV. For the muon channel, region C is defined to contain only same-charge muon pairs and also here the p_T^ℓ requirement is loosened to 20 GeV. Finally, for region D events are selected with the modifications of the B and C regions applied at the same time.

Multijet event yields N_{MJ} in each control region are estimated from data by subtracting the contribution from prompt leptons predicted by the simulation. Because of the very high signal contamination in the background-enriched regions in the $Z \to ee$ channel, the events with $80 < m_{\ell\ell} < 100\,\text{GeV}$ are excluded. The total MJ yield in the signal region is then estimated through $N_{MJ}^A = N_{MJ}^B \cdot N_{MJ}^C/N_{MJ}^D$. In the electron channel the final MJ yield is also scaled back to the full $m_{\ell\ell}$ range.

The final MJ event yield and uncertainty for each channel are summarised in Table 2. In all channels, the MJ event

estimate is below 0.1% with respect to the expected signal. In the $Z \to ee$ channel at 5.02 TeV the final MJ event estimate was found to be consistent with zero. An upper limit on the MJ yield in this channel is derived from the statistical uncertainties of the yields in the background-enriched regions.

The shape of the MJ events is taken from the corresponding distributions in the background-enriched regions. To suppress statistical fluctuations for the $p_T^{\ell\ell}$ and u_T distributions, the templates are smoothed with a Landau function and normalised to the inclusive number of MJ events for each channel.

The total impact of the background estimation on the unfolded $p_T^{\ell\ell}$ and u_T distributions for the 5.02 and 13 TeV datasets is provided in Figs. 26 and 27 in Appendix A and is generally well below 0.1%.

5.3 Detector-level event yields and distributions

The final observed and expected event yields for the full W and Z selections obtained in the electron and muon channels for both datasets are summarised in Tables 1 and 2. All calibrations and efficiency corrections discussed in Sects. 3 and 4 are applied.

Detector-level distributions for the 5.02 TeV dataset and for the 13 TeV dataset are provided in Figs. 4, 5, 6 and 7 and Figs. 8, 9, 10 and 11 for the W-boson analyses and in Figs. 12 and 13 for the Z-boson analyses. To better visualise the agreement in the shapes, the MC predictions are normalised to the integral of the data distribution. The underlying $p_T^{true,V}$ distributions have been reweighted with a smooth function as described in detail in Sect. 6.1 to match the data as closely as possible in the p_T^V range of 0–100 GeV.

Table 1 Observed and expected event yield comparison for the W-boson selections in the $\sqrt{s} = 5.02\,\text{TeV}$ and $\sqrt{s} = 13\,\text{TeV}$ datasets for the electron and muon channels split by the charge of the reconstructed lepton. The uncertainties in the multijet background correspond to the total uncertainties, while for backgrounds estimated from MC simulation only statistical uncertainties are given. The category $W \to \ell\nu$ BG refers to background from $W \to \tau\nu$ as well as charge misidentification in the electron channels

Channel	Observed	Signal	$W \to \ell\nu$ BG	$Z \to \ell\ell$	Top	Diboson	Multijet
$\sqrt{s} = 5.02\,\text{TeV}$ $W \to \ell\nu$							
$W^- \to e^-\nu$	274375	264510 ± 170	7303 ± 29	1031 ± 6	862.7 ± 2.1	340.5 ± 2.9	2200 ± 700
$W^+ \to e^+\nu$	430662	417090 ± 210	9064 ± 32	1102 ± 7	951.4 ± 2.9	376.2 ± 2.3	2300 ± 900
$W^- \to \mu^-\nu$	288026	273900 ± 170	5160 ± 25	8517 ± 21	799.0 ± 2.0	339.1 ± 1.9	300 ± 340
$W^+ \to \mu^+\nu$	457223	438020 ± 210	7854 ± 30	9773 ± 22	890.6 ± 2.8	384.6 ± 2.3	500 ± 400
$\sqrt{s} = 13\,\text{TeV}$ $W \to \ell\nu$							
$W^- \to e^-\nu$	949297	876490 ± 270	22360 ± 60	6546 ± 21	12780 ± 50	1720 ± 50	27000 ± 5000
$W^+ \to e^+\nu$	1207652	1116800 ± 300	24680 ± 60	6883 ± 21	13260 ± 50	1720 ± 50	29000 ± 5000
$W^- \to \mu^-\nu$	964514	897400 ± 270	14650 ± 50	33940 ± 40	11950 ± 50	1620 ± 40	6000 ± 2000
$W^+ \to \mu^+\nu$	1245755	1153400 ± 300	18390 ± 50	37690 ± 40	12520 ± 50	1720 ± 50	6000 ± 2000

Table 2 Observed and expected event yield comparison for Z-boson selections in the $\sqrt{s} = 5.02\,\text{TeV}$ and $\sqrt{s} = 13\,\text{TeV}$ datasets for the electron and muon channels. The uncertainties in the multijet background correspond to the total uncertainties, while for backgrounds estimated from MC simulation only statistical uncertainties are given

Channel	Observed	Signal	$Z \to \tau\tau$	Top	Diboson	Multijet
$\sqrt{s} = 5.02\,\text{TeV}$ $Z \to \ell\ell$						
$Z \to ee$	51772	51310 ± 40	23 ± 4	35.5 ± 0.4	109.1 ± 2.0	0 ± 100
$Z \to \mu\mu$	70447	69820 ± 60	39 ± 5	44.0 ± 0.4	144.9 ± 2.1	16 ± 8
$\sqrt{s} = 13\,\text{TeV}$ $Z \to \ell\ell$						
$Z \to ee$	165027	158000 ± 100	80 ± 8	500 ± 10	324 ± 15	110 ± 70
$Z \to \mu\mu$	214035	207900 ± 100	80 ± 8	554 ± 9	414 ± 17	180 ± 40

In the ratio panels, the grey band is the total systematic uncertainty, while for the brown band the typically small statistical uncertainty in the MC simulation is added in quadrature. The systematic uncertainty shown is the experimental uncertainty excluding luminosity, since the MC simulation is normalised to the data integral, and excluding the uncertainty derived from the alternative signal simulation using SHERPA. The χ^2/dof shown includes all shown uncertainties and is calculated with the corresponding covariance matrix taking into account bin-to-bin correlations of the systematic uncertainties.

Overall, good agreement is observed between the data and the MC simulation estimates in all the kinematic distributions. Several channels at 13 TeV show a modest mismodelling of the high p_T tails by a few percent, such as the lepton p_T distributions for the W boson (Fig. 10). These are due to imperfections in the $p_\text{T}^{\text{true},V}$ reweighting. However, the spectra are sufficiently well modelled to perform the p_T^V measurements and corresponding uncertainties are assessed in the unfolding.

6 Cross-section measurement

The W^-, W^+ and Z-boson transverse momentum distributions are measured separately for the electron and muon decay channels. Results are reported in a fiducial phase space close to the experimental acceptance, and defined by particle-level kinematics as follows:

- $W \to \ell\nu$: $p_\text{T}^\ell > 25$ GeV, $|\eta^\ell| < 2.5$, $p_\text{T}^\nu > 25$ GeV, and $m_\text{T} > 50$ GeV;
- $Z \to \ell\ell$: $p_\text{T}^\ell > 25$ GeV, $|\eta^\ell| < 2.5$, and 66 GeV $< m_{\ell\ell} < 116$ GeV.

The lepton kinematics used in the definition of the cross sections corresponds to the Born level for QED final-state radiation effects. The primary signal model, POWHEG+PYTHIA8, uses PHOTOS++ to simulate QED FSR. This setup has been benchmarked extensively in the past, at the sub-permille level on the distributions [77]. No explicit uncertainties are included, although the comparison to SHERPA implicitly uses another QED FSR model. The Z-boson measurements
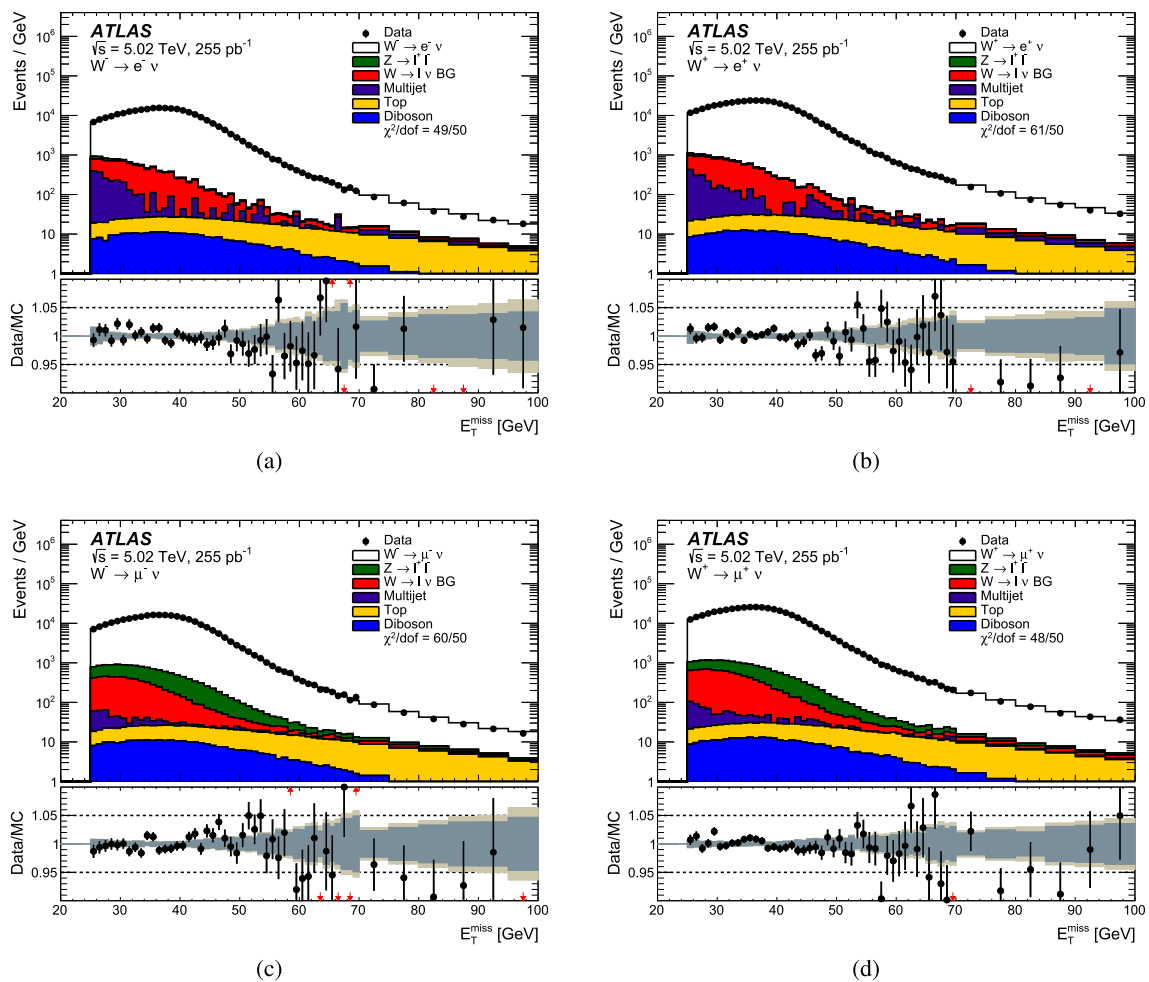
Fig. 4 Missing transverse momentum E_T^{miss} distributions in the **a** $W^- \to e^- \nu$, **b** $W^+ \to e^+ \nu$, **c** $W^- \to \mu^- \nu$ and **d** $W^+ \to \mu^+ \nu$ channels for the $\sqrt{s} = 5.02$ TeV dataset. The data (black points) is compared to the sum of all expected background and signal contributions, shown as a solid line, normalised to the total data yield. The lower panel shows the ratio of the data to the full prediction (black points) as well as the prediction uncertainties around 1 excluding (including) the MC simulation statistical component as dark (light) band. The prediction uncertainties shown exclude those from the luminosity measurement and the alternative signal modelling, see text. The χ^2/dof is computed using the full covariance matrix of all shown statistical and systematic uncertainties. The category $W \to \ell\nu$ BG refers to background from $W \to \tau\nu$ and charge misidentification in the electron channels

include the small virtual photon contributions, i.e. the full $Z/\gamma^* \to \ell\ell$ process is measured. The measured differential cross sections are also used to derive integrated cross sections and ratios.

The measurement bins are chosen by taking into consideration competing demands on the analysis, namely sensitivity to the underlying physics, the statistical precision in each bin, and detector resolution effects. The latter are particularly important for the hadronic recoil observable at low boson transverse momentum and require a minimum bin size of 7 GeV at low p_T^V to ensure that the unfolding systematic uncertainties are around 1% or lower. The measurement is performed in $p_T^{\mathrm{true}, V}$ bins with bin edges as follows:

- p_T^W at 5.02 TeV: [0, 7, 14, 21, 28, 35, 42, 49, 56, 63, 77, 92, 115, 145, 175, 220] GeV;

- p_T^W at 13 TeV: [0, 7, 14, 21, 28, 35, 42, 49, 56, 63, 77, 92, 115, 145, 175, 220, 310, 600] GeV;

- p_T^Z at 5.02 TeV: [0, 2, 4, 6, 8, 10, 12, 14, 17, 20, 23, 26, 29, 33, 37, 41, 47, 53, 60, 70, 80, 92, 115, 145, 175, 220] GeV;

- p_T^Z at 13 TeV: [0, 2, 4, 6, 8, 10, 12, 14, 17, 20, 23, 26, 29, 33, 37, 41, 47, 53, 60, 70, 80, 92, 115, 145, 175, 220, 310, 600] GeV.

The p_T^Z distribution is measured separately using the u_T and the $p_T^{\ell\ell}$ observables. The former is used to validate the measurement procedures in the same bins as the respective p_T^W measurements, as discussed in Sect. 6.3, while the latter is used in the main p_T^Z measurements with the finer binning given above. For the differential W/Z ratio measure-
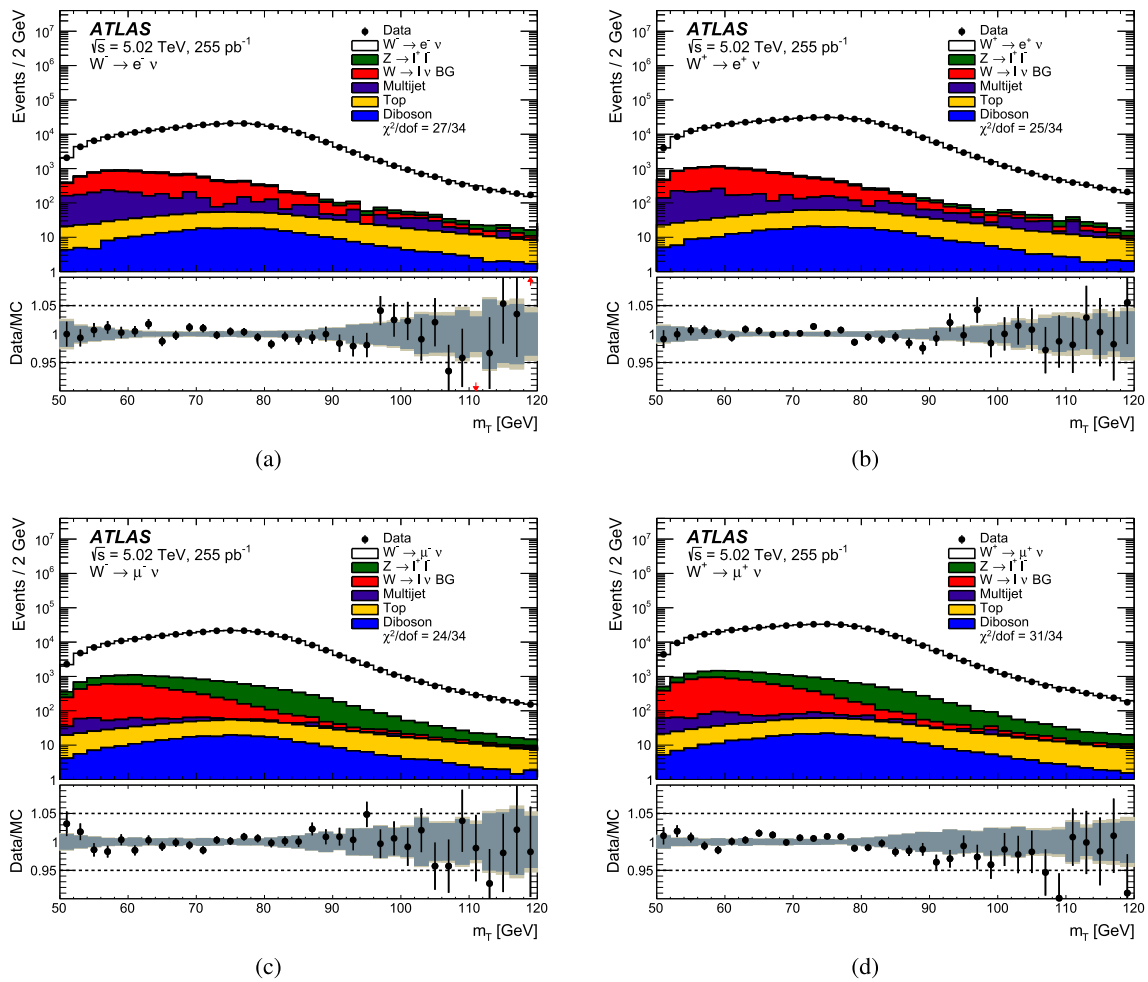
Fig. 5 Transverse mass m_T distribution of the W boson in the **a** $W^- \to e^- \nu$, **b** $W^+ \to e^+ \nu$, **c** $W^- \to \mu^- \nu$ and **d** $W^+ \to \mu^+ \nu$ channels for the $\sqrt{s} = 5.02$ TeV dataset. The data (black points) is compared to the sum of all expected background and signal contributions, shown as a solid line, normalised to the total data yield. The lower panel shows the ratio of the data to the full prediction (black points) as well as the prediction uncertainties around 1 excluding (including) the MC simulation statistical component as dark (light) band. The prediction uncertainties shown exclude those from the luminosity measurement and the alternative signal modelling, see text. The $\chi^2/$dof is computed using the full covariance matrix of all shown statistical and systematic uncertainties. The category $W \to \ell\nu$ BG refers to background from $W \to \tau\nu$ and charge misidentification in the electron channels

ments, the Z boson distribution is also measured using the $p_T^{\ell\ell}$ observable in the same bins as the W distributions.

6.1 Unfolding

The distributions observed after analysis selections and background subtraction are corrected for detector effects using an iterative Bayesian unfolding method [78,79]. First, the data are corrected for events that pass the detector-level selection but not the particle-level selection. The iterative Bayesian unfolding technique is then used to correct for the finite detector acceptance, resolution and reconstruction efficiency and estimate the true underlying distribution.

Simulated events are used to determine the response matrices needed to correct for the migration between bins in the

detector- and particle-level distributions. The hadronic recoil resolution leads to significant migrations in u_T. The effect of the detector resolution on the event migrations is illustrated in Fig. 14, which compares the observed $p_T^{\ell\ell}$ and u_T distributions for given intervals in $p_T^{\text{true},V}$, in simulated $Z \to \mu\mu$ events at 13 TeV. Significant differences are observed in the corresponding reconstructed distributions. The particle-level binning is therefore optimised separately for each observable. The number of iterations in the unfolding procedure is optimised to minimise the total measurement uncertainty, and specifically the uncertainty related to possible biases induced by the unfolding prior. Methods to estimate the unfolding bias and the optimisation of the number of iterations are discussed further in this section.
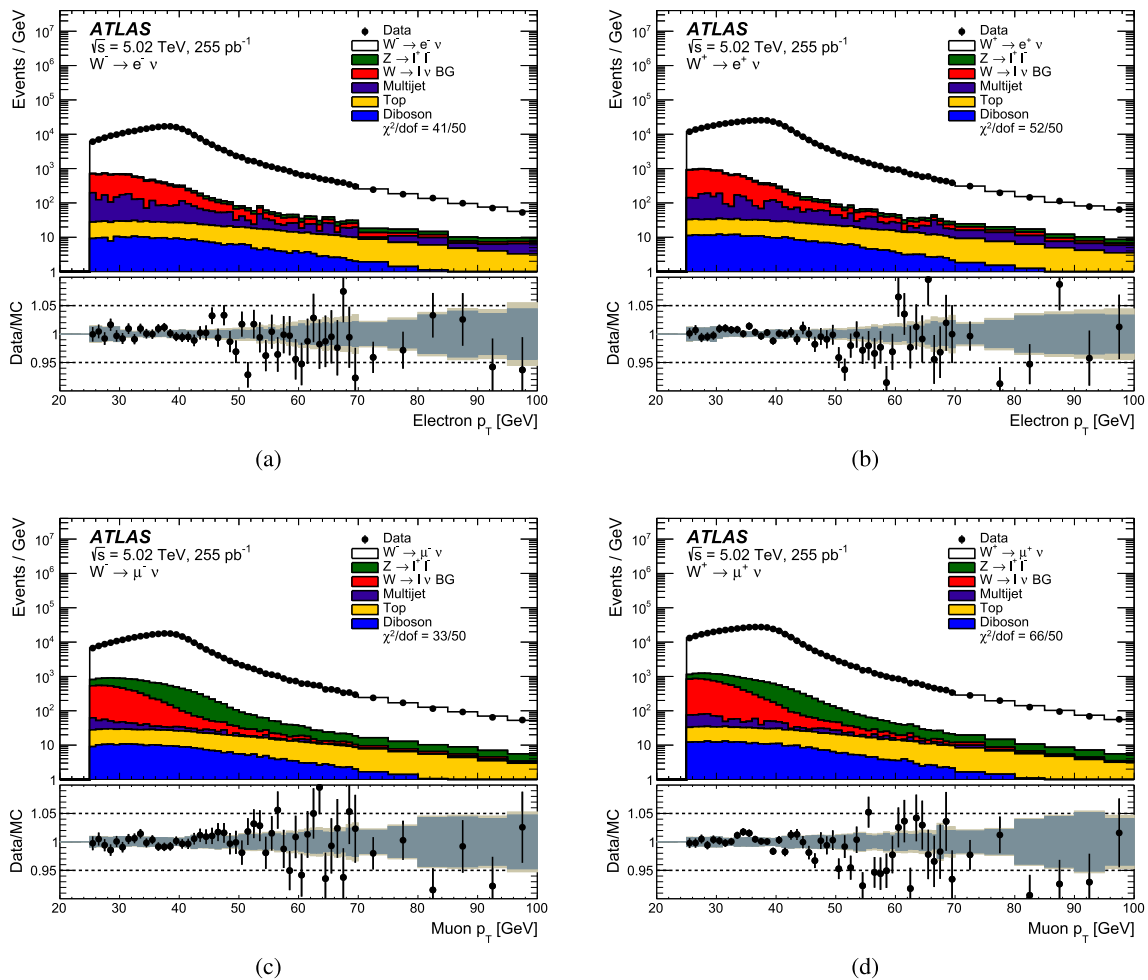
(a)

(b)

(c)

(d)

Fig. 6 Lepton transverse momentum p_T distributions in the **a** $W^- \to e^- \nu$, **b** $W^+ \to e^+ \nu$, **c** $W^- \to \mu^- \nu$ and **d** $W^+ \to \mu^+ \nu$ channels for the $\sqrt{s} = 5.02$ TeV dataset. The data (black points) is compared to the sum of all expected background and signal contributions, shown as a solid line, normalised to the total data yield. The lower panel shows the ratio of the data to the full prediction (black points) as well as the prediction uncertainties around 1 excluding (including) the MC simulation statistical component as dark (light) band. The prediction uncertainties shown exclude those from the luminosity measurement and the alternative signal modelling, see text. The χ^2/dof is computed using the full covariance matrix of all shown statistical and systematic uncertainties. The category $W \to \ell \nu$ BG refers to background from $W \to \tau \nu$ and charge misidentification in the electron channels

After calibration corrections, the detector-level transverse momentum distributions in data and MC are found to disagree, i.e. the difference is found to be significantly larger than the experimental sensitivity, especially at 13 TeV. To minimise the related uncertainties, the simulation is reweighted in $p_T^{\mathrm{true},V}$ to optimise the agreement between data and MC for the reconstructed u_T (or $p_T^{\ell\ell}$) distributions for W (and Z) analyses.[2] This procedure ensures that the unfolding bias is kept as low as possible.

The agreement between data and simulation is optimised for the u_T distribution by minimising the following χ^2:

$$\chi^2 = \sum_{ij} \Delta_i \, (C^{-1})_{ij} \, \Delta_j, \qquad (5)$$

$$\Delta_i = (D_i - B_i) - \sum_k T_{ik} \times w_k. \qquad (6)$$

Here $(C^{-1})_{ij}$ denotes the inverted total covariance between detector-level bins i and j, including statistical and systematic uncertainties in the observed and simulated u_T distributions; Δ_i is the difference between the background-subtracted data distribution in bin i, $D_i - B_i$, and the corresponding reconstruction-level simulated distribution. The latter is obtained from the product between a generator-level

---

[2] To achieve this, the analysis including some background estimates is iterated. Object calibrations, including the hadronic recoil are performed such that they are to first order insensitive to the p_T^V modelling in the MC simulation.
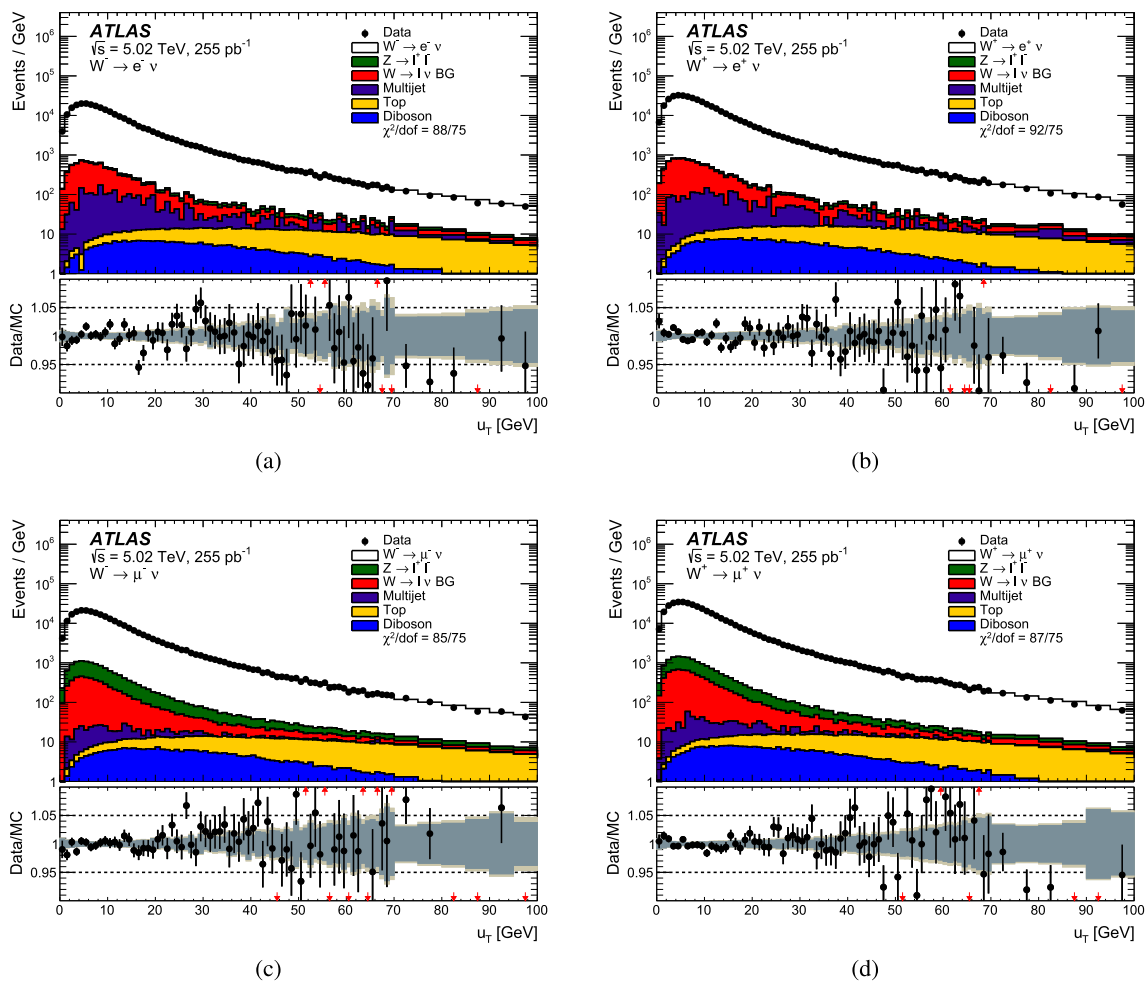
(a)

(b)

(c)

(d)

Fig. 7 Hadronic recoil u_T distributions (boson transverse momentum) in the **a** $W^- \to e^- \nu$, **b** $W^+ \to e^+ \nu$, **c** $W^- \to \mu^- \nu$ and **d** $W^+ \to \mu^+ \nu$ channels for the $\sqrt{s} = 5.02$ TeV dataset. The data (black points) is compared to the sum of all expected background and signal contributions, shown as a solid line, normalised to the total data yield. The lower panel shows the ratio of the data to the full prediction (black points) as well as the prediction uncertainties around 1 excluding (including) the MC

simulation statistical component as dark (light) band. The prediction uncertainties shown exclude those from the luminosity measurement and the alternative signal modelling, see text. The χ^2/dof is computed using the full covariance matrix of all shown statistical and systematic uncertainties. The category $W \to \ell\nu$ BG refers to background from $W \to \tau\nu$ and charge misidentification in the electron channels

weighting coefficient w_k and the transfer matrix T_{ik} that is filled with the number of entries in bins i, k at detector and particle level, respectively. The weight, w_k, is the average in particle-level bin k of a continuous weighting function $w(p_T^{\text{true},V})$ that modifies the p_T^W distribution in the MC sample. The parameters of $w(p_T^{\text{true},V})$ are the degrees of freedom in the minimisation procedure. A satisfactory agreement is obtained using the empirical function

$$w(p_T) = N \left[\left(1 + a \, p_T^{\text{true},V} + b \left(p_T^{\text{true},V} \right)^2 \right) \right.$$
$$\left. \times \left(1 - c + c \times r_{\text{NNPDF/CT10}}(p_T^{\text{true},V}) \right) \right], \quad (7)$$

where N is an overall normalisation factor and $r_{\text{NNPDF/CT10}}$ $(p_T^{\text{true},V})$ represents the ratio of DYTURBO predictions

obtained using NNPDF3.0 and CT10NLO in the full phase space. The additional parameters (a, b, c) provide more flexibility to minimise the χ^2 of Eq. (5).

The reweighting functions are optimised separately for each process and each centre-of-mass energy. They are derived over the $p_T^{\text{true},V}$ range of $0 - 100$ GeV where a good modelling of the spectrum is critical. The value of the correction at $p_T^{\text{true},V} = 100$ GeV is used for $p_T^{\text{true},V} > 100$ GeV, as the impact on the final results in this region is found to be negligible. Using the $W^- \to \ell^- \nu$ at 13 TeV as example, the two reweighting functions for the electron and muon channels are shown in Fig. 15a. Since the e and μ channel are compatible for all final states, the averages of the respective two reweighting functions are later applied to both chan-
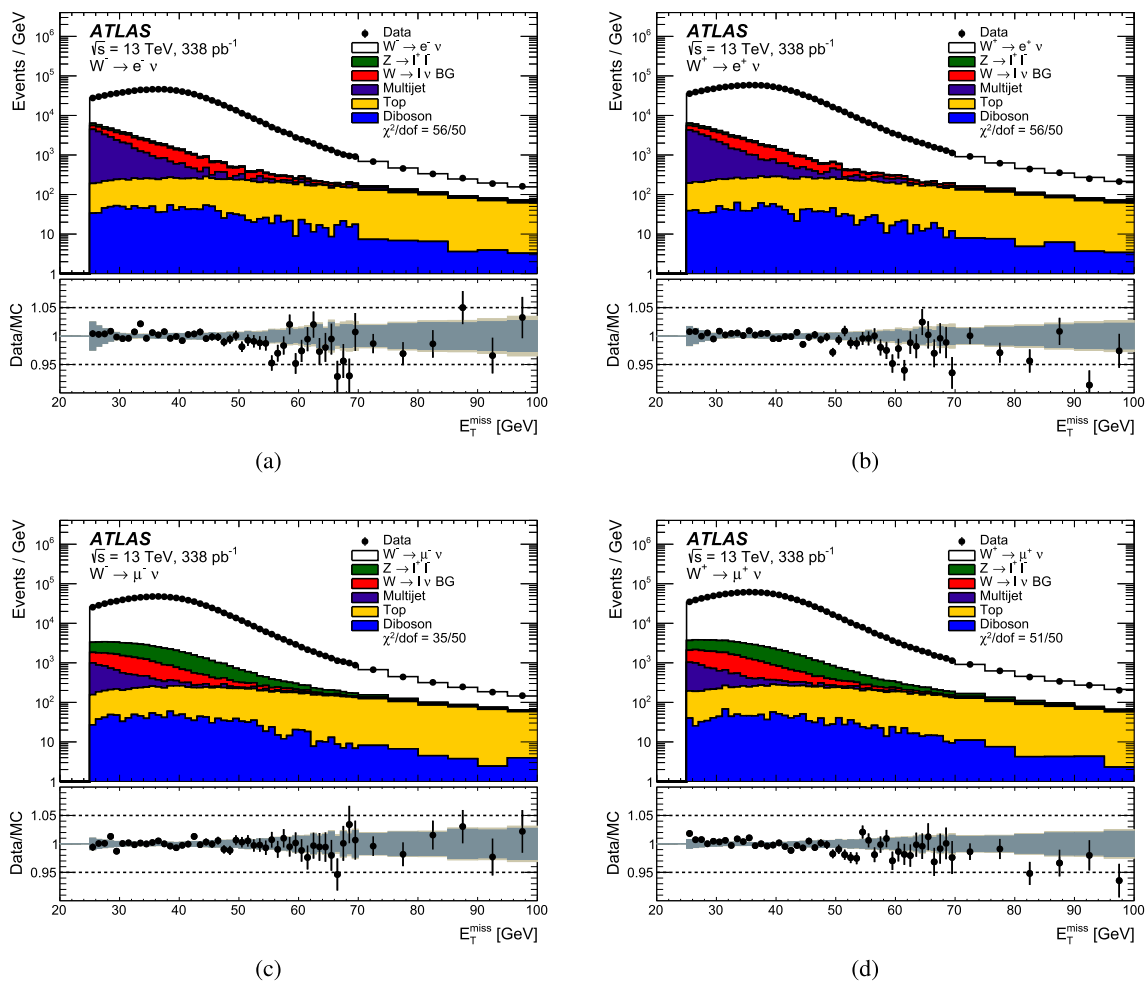
Fig. 8 Missing transverse momentum E_T^{miss} distributions in the **a** $W^- \rightarrow e^- \nu$, **b** $W^+ \rightarrow e^+ \nu$, **c** $W^- \rightarrow \mu^- \nu$ and **d** $W^+ \rightarrow \mu^+ \nu$ channels for the $\sqrt{s} = 13$ TeV dataset. The data (black points) is compared to the sum of all expected background and signal contributions, shown as a solid line, normalised to the total data yield. The lower panel shows the ratio of the data to the full prediction (black points) as well as the prediction uncertainties around 1 excluding (including) the MC simulation statistical component as dark (light) band. The prediction uncertainties shown exclude those from the luminosity measurement and the alternative signal modelling, see text. The χ^2/dof is computed using the full covariance matrix of all shown statistical and systematic uncertainties. The category $W \rightarrow \ell \nu$ BG refers to background from $W \rightarrow \tau \nu$ and charge misidentification in the electron channels

nels. The corresponding effect of this p_T^V reweighting on the reconstructed u_T distributions is shown in Fig. 15b.

The reweighed simulation is used to determine the response matrix used in the unfolding. Both the bin size at low p_T^W and the number of unfolding iterations are optimised given the considerations discussed above. More unfolding iterations increase the statistical uncertainty while reducing the unfolding bias. Since the statistical uncertainty is relatively small compared with the unfolding bias, a larger number of iterations is favoured and allows to obtain a small unfolding bias at the price of a little increase in the statistical uncertainties. The choice of number of iterations is made by achieving the lowest quadratic sum of statistical uncertainty, systematic uncertainty and unfolding bias. A number of 25 iterations is found to be optimal for the 13 TeV analysis

to minimise the total uncertainties. In the smaller 5.02 TeV samples the optimal number of iterations is found to be nine.

For the Z process the same approach is used, with the addition that separate reweightings are derived using the $p_T^{\ell\ell}$ and u_T distributions for the respective measurements.[3] Because of the far better resolution in $p_T^{\ell\ell}$, only two unfolding iterations are used. Uncertainties related to the assumed prior for the p_T^V spectrum in the unfolding are discussed in the next section.

---

[3] The measurement of p_T^Z using the u_T distribution is only used in the validation of the measurement procedure presented in Sect. 6.3.

(a)

(b)
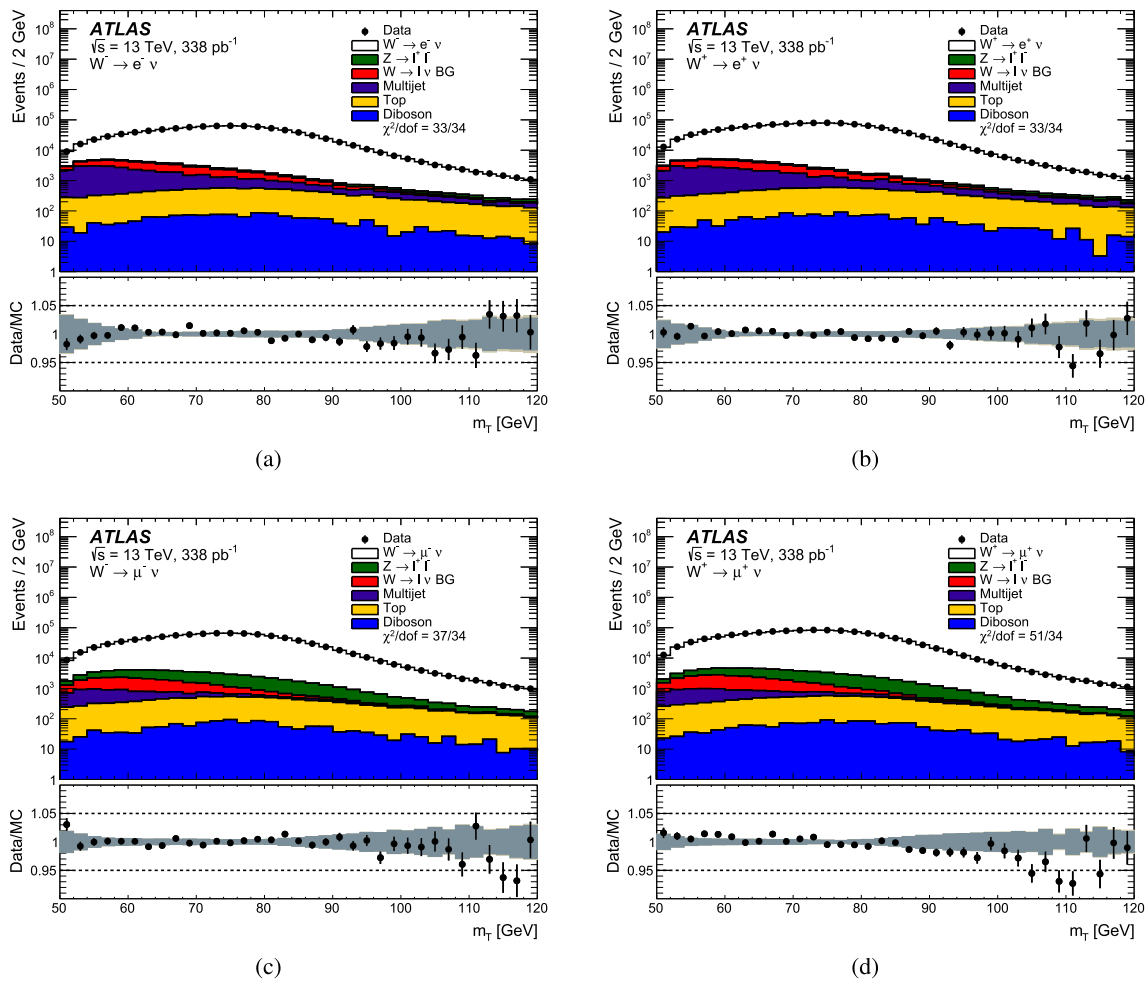
(c)

(d)

Fig. 9 Transverse mass m_T distributions of the W boson in the **a** $W^- \to e^- \nu$, **b** $W^+ \to e^+ \nu$, **c** $W^- \to \mu^- \nu$ and **d** $W^+ \to \mu^+ \nu$ channels for the $\sqrt{s} = 13$ TeV dataset. The data (black points) is compared to the sum of all expected background and signal contributions, shown as a solid line, normalised to the total data yield. The lower panel shows the ratio of the data to the full prediction (black points) as well as the prediction uncertainties around 1 excluding (including) the MC simulation statistical component as dark (light) band. The prediction uncertainties shown exclude those from the luminosity measurement and the alternative signal modelling, see text. The χ^2/dof is computed using the full covariance matrix of all shown statistical and systematic uncertainties. The category $W \to \ell \nu$ BG refers to background from $W \to \tau \nu$ and charge misidentification in the electron channels

6.2 Systematic uncertainties

The present measurement is affected by statistical uncertainties as well as systematic uncertainties related to detector calibration, the background estimate, the definition of the response matrix and to the unfolding procedure. For each uncertainty, the corresponding source of uncertainty is varied to estimate the effect on the final result. A graphical representation of the uncertainties is given in Appendix A.

The effect on the measurement from the finite size of the data and MC simulated samples is estimated by generating pseudo-experiment variations of the respective samples [80]. The resulting statistical uncertainties are uncorrelated between channels, but partially correlated between bins due to the unfolding. In the p_T^W measurement at 5.02 TeV, where

the event samples are smaller than at 13 TeV, the statistical uncertainty of the data is the co-dominant uncertainty beyond $p_T^W = 20$ GeV, going from about 0.5% below this region to $\approx 2.5\%$ at $p_T^W = 60$ GeV. At 13 TeV, it becomes dominant around $p_T^W = 60$ GeV. For the p_T^Z measurements, the statistical uncertainty of the data is the dominant source of uncertainty.

Uncertainties in the scale and resolution of the hadronic recoil are among the dominant uncertainties in the p_T^W measurement. They are estimated by propagating the statistical uncertainties in the calibration procedure and systematic effects as discussed in Sect. 4. In the first p_T^W bin these are usually the largest or second-largest systematic uncertainties reaching typically 0.6%. They grow moderately with p_T^W depending on the boson charge and on the centre of mass
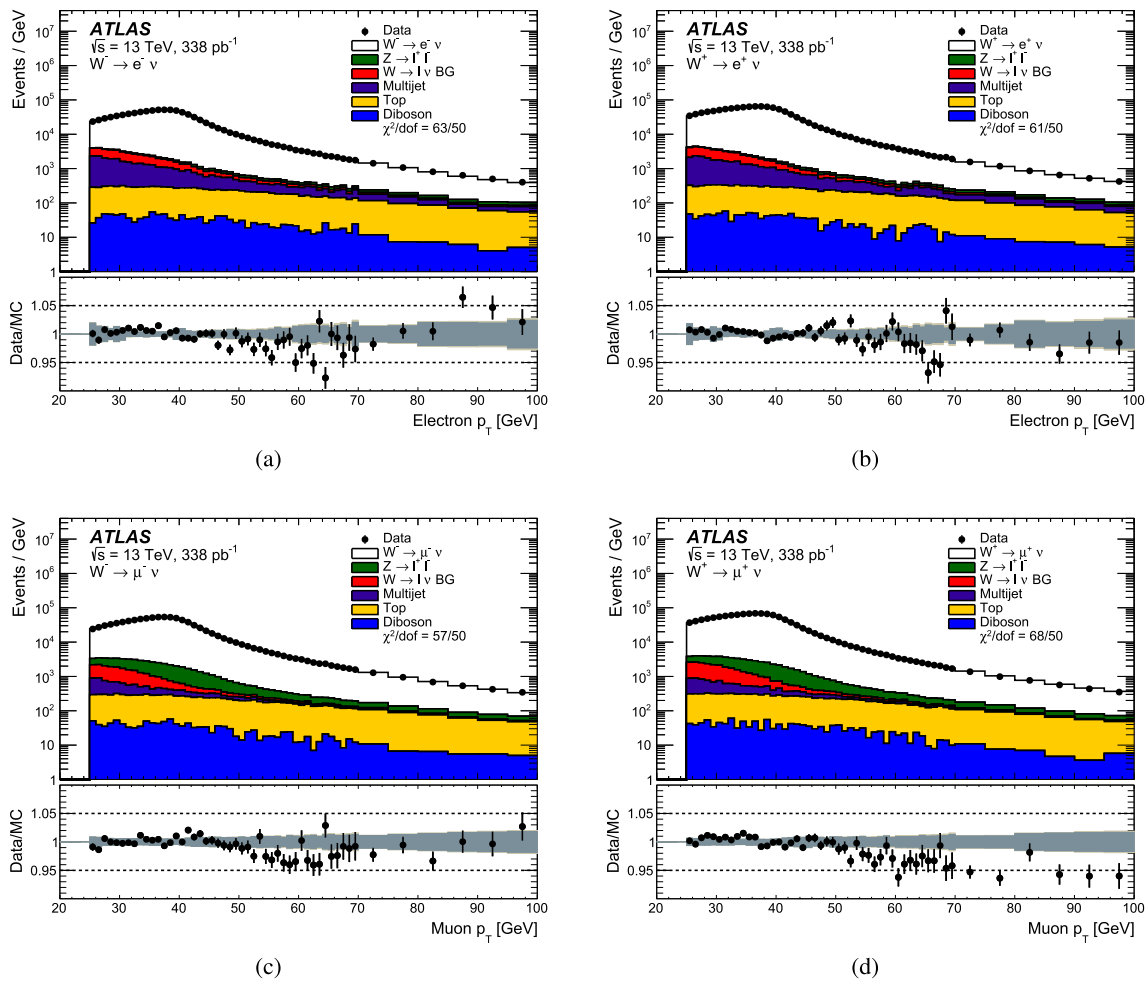
Fig. 10 Lepton transverse momentum p_T distributions in the **a** $W^- \to e^-\nu$, **b** $W^+ \to e^+\nu$, **c** $W^- \to \mu^-\nu$ and **d** $W^+ \to \mu^+\nu$ channels for the $\sqrt{s} = 13$ TeV dataset. The data (black points) is compared to the sum of all expected background and signal contributions, shown as a solid line, normalised to the total data yield. The lower panel shows the ratio of the data to the full prediction (black points) as well as the prediction uncertainties around 1 excluding (including) the MC simulation statistical component as dark (light) band. The prediction uncertainties shown exclude those from the luminosity measurement and the alternative signal modelling, see text. The χ^2/dof is computed using the full covariance matrix of all shown statistical and systematic uncertainties. The category $W \to \ell\nu$ BG refers to background from $W \to \tau\nu$ and charge misidentification in the electron channels

energy. In the p_T^W range of 30–50 GeV, the uncertainty in the measurement for W^- events is slightly higher than for W^+ events, due to observed differences between the extrapolation uncertainties from the Z-boson. In the 5.02 TeV data, it reaches 1.5% at 50 GeV, and goes up to $\approx 3\%$ at 100 GeV. At 13 TeV, since more Z events are available for the calibration, the uncertainty is smaller, and increases slowly to reach 1.5% at 100 GeV.

Lepton-related systematic uncertainties due to energy scale and resolution as well as reconstruction and selection efficiency corrections are propagated considering the statistical and systematic uncertainties in the procedures described in Sects. 3.1 and 3.2. They have only a small effect on both the p_T^W and the p_T^Z measurements.

Uncertainties in the background estimation are only significant in the W analysis. Uncertainties induced by the simulated backgrounds are obtained by independently varying the corresponding cross sections. The uncertainty in the multijet background is dominant in the electron channel. The estimated multijet background yields are treated as correlated between the channels since the same techniques are used.

The uncertainty assigned to the unfolding procedure itself is estimated from the dependence of the results on the assumed priors for the p_T^V distributions. The nominal particle-level spectrum, obtained from the reweighting procedure described in Sect. 6.1, is varied within the fit uncertainties, taking correlations between the fit parameters into account. Alternative functional forms are used to test the influence of the p_T^V distribution at low values. The base-
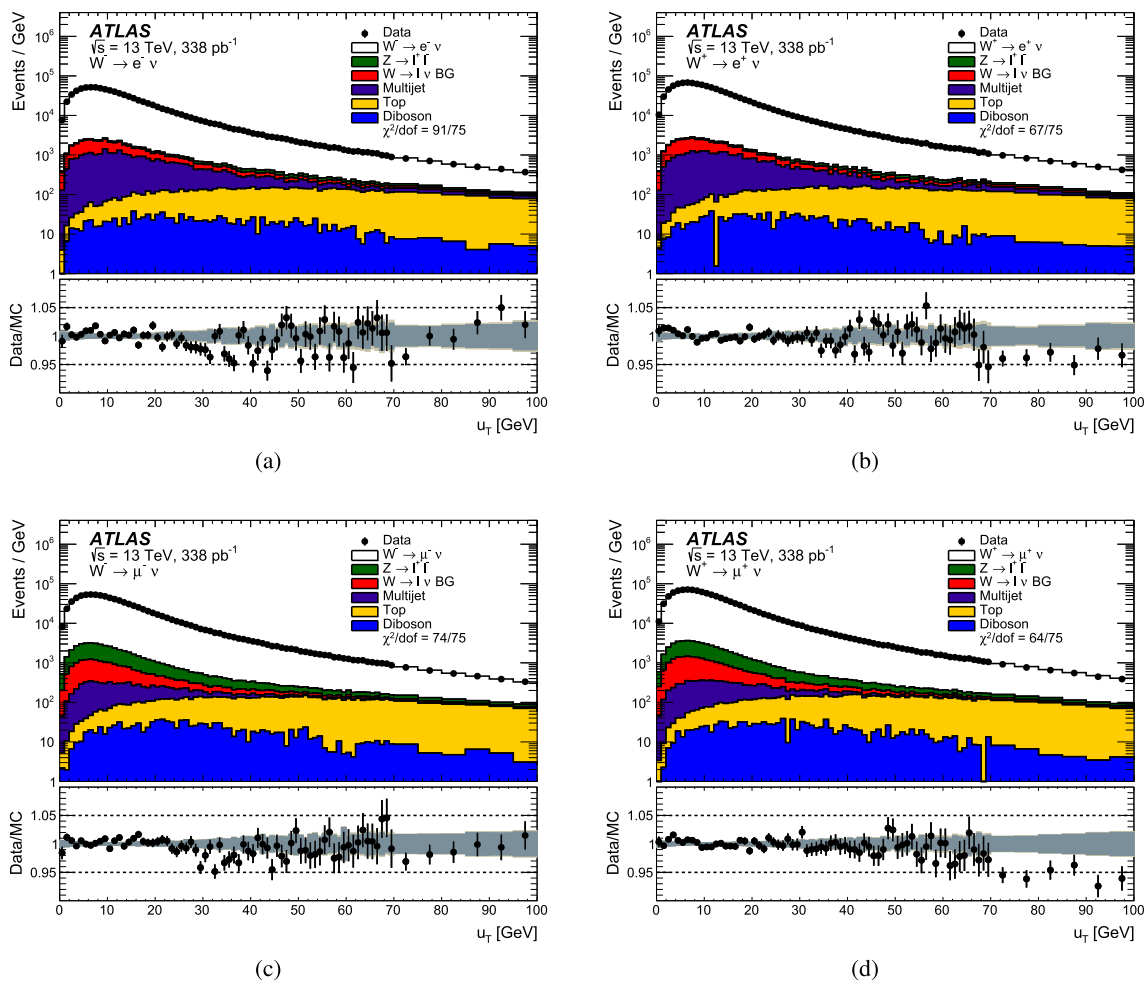
Fig. 11 Hadronic recoil u_T distributions (boson transverse momentum) in the **a** $W^- \to e^- \nu$, **b** $W^+ \to e^+ \nu$, **c** $W^- \to \mu^- \nu$ and **d** $W^+ \to \mu^+ \nu$ channels for the $\sqrt{s} = 13$ TeV dataset. The data (black points) is compared to the sum of all expected background and signal contributions, shown as a solid line, normalised to the total data yield. The lower panel shows the ratio of the data to the full prediction (black points) as well as the prediction uncertainties around 1 excluding (including) the MC simulation statistical component as dark (light) band. The prediction uncertainties shown exclude those from the luminosity measurement and the alternative signal modelling, see text. The χ^2/dof is computed using the full covariance matrix of all shown statistical and systematic uncertainties. The category $W \to \ell\nu$ BG refers to background from $W \to \tau\nu$ and charge misidentification in the electron channels

line particle-level distribution at a given rapidity is modified using alternative predictions. A binning in rapidity prevents any modeling bias, since the p_T^V spectra depend on rapidity. Four alternative predictions are chosen: DYTURBO with the NNPDF3.1 and CT10 PDF sets; POWHEG+HERWIG 7, and PYTHIA 8, described in more detail in Sect. 7.3. The SHERPA samples introduced in Sect. 2.3 are considered but discarded due to the poor description of the data below 20 GeV.

The closure of the unfolding procedure is further tested using the alternative SHERPA model for the signal MC simulation, as discussed at the end of Sect. 4. The SHERPA samples represent a completely independent implementation of the physics of vector boson production and decay as compared to POWHEG+PYTHIA 8. In many respects, such as the vertex efficiency (Sect. 3.3) and the modelling of quantities relevant for the hadronic recoil (Sect. 4.2), the predictions of the two generators bracket the data. At 5.02 TeV, the resulting uncertainty stays subdominant in the region $p_T^W < 30$ GeV, whereas at 13 TeV, it is the largest or second-to-largest systematic uncertainty, reaching more than 1% in the second bin.

The uncertainties in the integrated luminosities are 1.0 and 0.92% for the 5.02 and 13 TeV datasets, following the methodology discussed in Ref. [32], using the LUCID-2 detector [29] for the primary luminosity measurements, com-
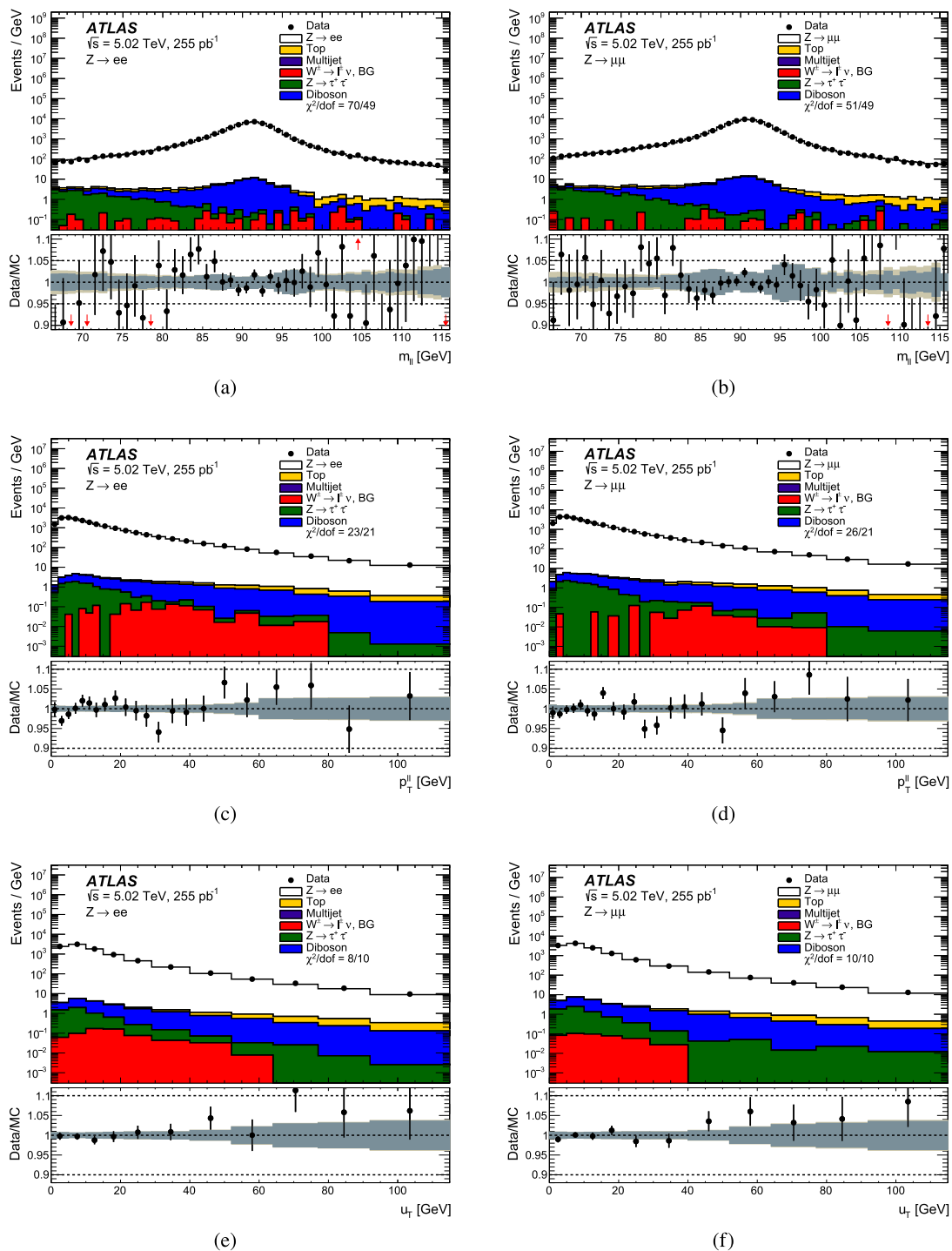
Fig. 12 Distributions of dilepton mass $m_{\ell\ell}$ in the **a** $Z \rightarrow ee$ and **b** $Z \rightarrow \mu\mu$ channels, of dilepton transverse momentum $p_T^{\ell\ell}$ in the **c** $Z \rightarrow ee$ and **d** $Z \rightarrow \mu\mu$ channels, and of hadronic recoil u_T in the **e** $Z \rightarrow ee$ and **f** $Z \rightarrow \mu\mu$ channels in the $\sqrt{s} = 5.02$ TeV analysis. The data (black points) is compared to the sum of all expected background and signal contributions, shown as a solid line, normalised to the total data yield. The lower panel shows the ratio of the data to the full prediction (black points) and the prediction uncertainties around 1 excluding (including) the MC simulation statistical component as dark grey (light brown) band. The prediction uncertainties shown exclude those from the luminosity measurement and the alternative signal modelling, see text. The χ^2/dof is computed using the full covariance matrix of all shown statistical and systematic uncertainties
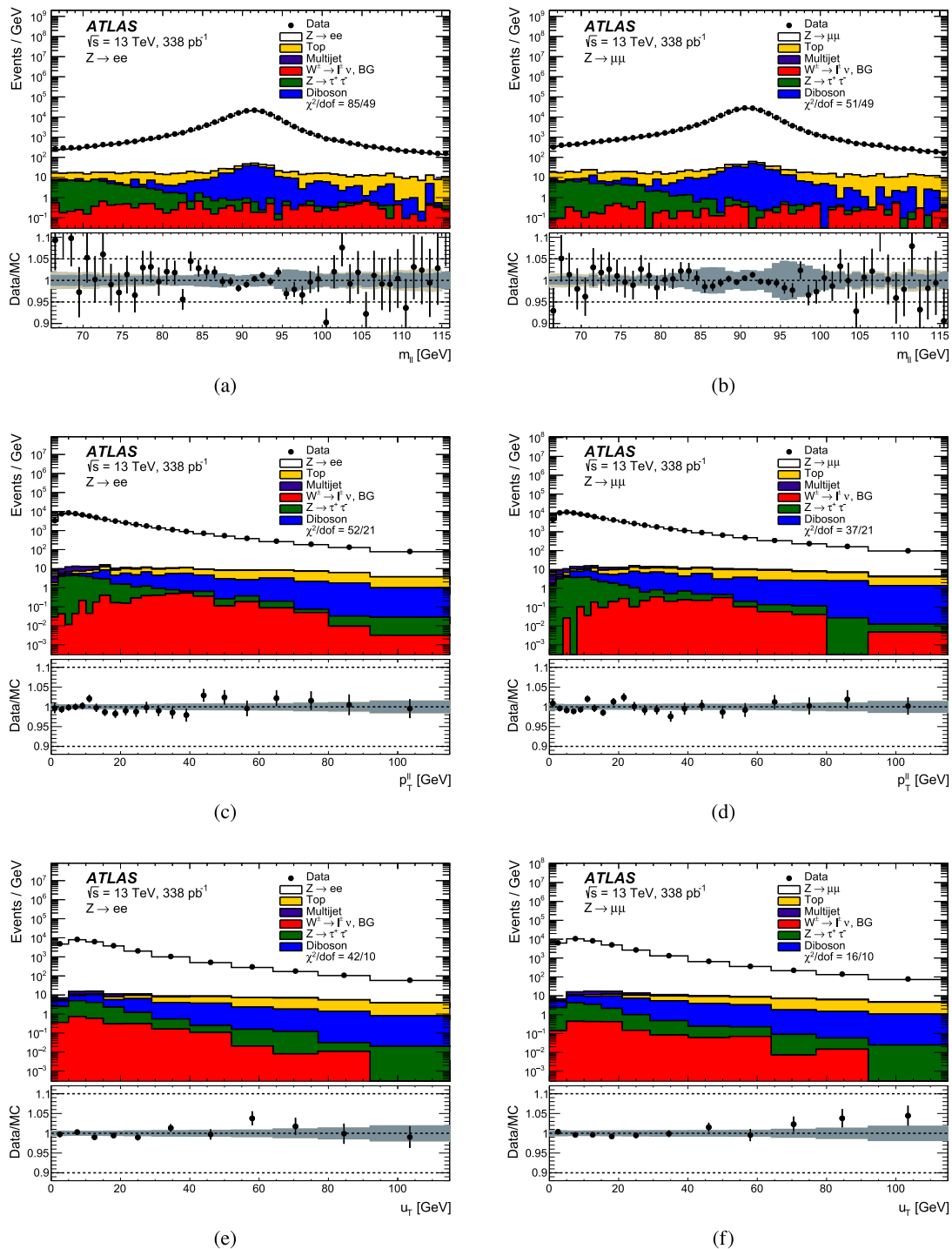
Fig. 13 Distributions of dilepton mass $m_{\ell\ell}$ in the **a** $Z \to ee$ and **b** $Z \to \mu\mu$ channels, of dilepton transverse momentum $p_T^{\ell\ell}$ in the **c** $Z \to ee$ and **d** $Z \to \mu\mu$ channels, and of hadronic recoil u_T in the **e** $Z \to ee$ and **f** $Z \to \mu\mu$ channels in the $\sqrt{s} = 13$ TeV analysis. The data (black points) is compared to the sum of all expected background and signal contributions, shown as a solid line, normalised to the total data yield. The lower panel shows the ratio of the data to the full predic-tion (black points) and the prediction uncertainties around 1 excluding (including) the MC simulation statistical component as dark grey (light brown) band. The prediction uncertainties shown exclude those from the luminosity measurement and the alternative signal modelling, see text. The χ^2/dof is computed using the full covariance matrix of all shown statistical and systematic uncertainties

Fig. 14 Distributions of measured **a** dilepton system $p_T^{\ell\ell}$ and **b** hadronic recoil u_T, shown in five intervals of the true boson transverse momentum p_T^Z, for $Z \to \mu\mu$ events at $\sqrt{s} = 13$ TeV
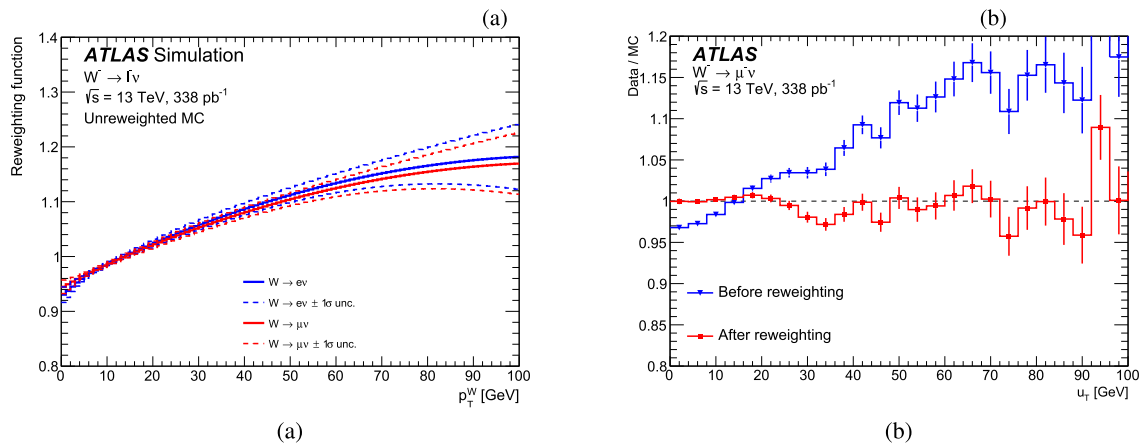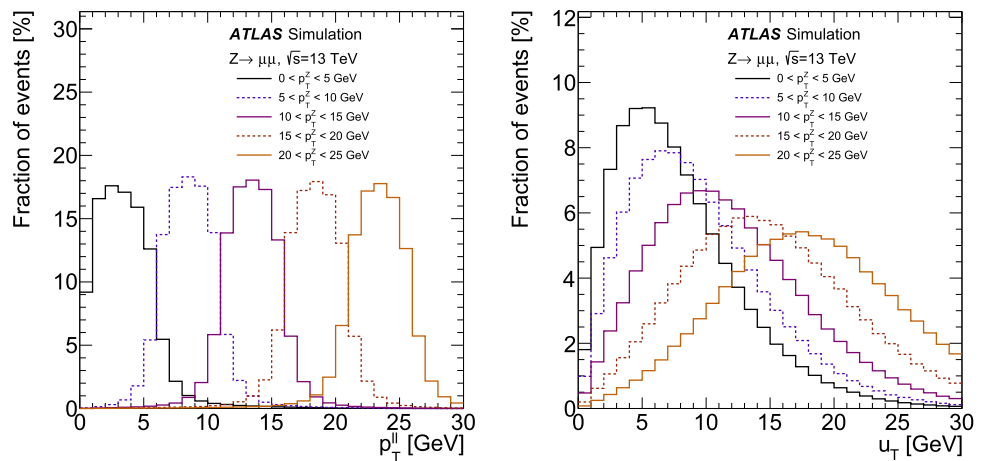

(a)

(b)

(a)

(b)

Fig. 15 **a** Fitted truth reweighting functions w_T in the electron and muon channels (full lines) for $W^- \to \ell^- \nu$ at $\sqrt{s} = 13$ TeV. The dashed lines represent the uncertainty on the reweighting functions from the fit. **b** The data-to-simulation ratios of the reconstructed u_T distributions before (blue triangles) and after (red squares) the reweighting. Error bars are statistical only

plemented by measurements using the inner detector and calorimeters.

6.3 Validation of recoil-based measurement with Z dilepton

In the Z samples, the transverse momentum spectra can be inferred either from the $p_T^{\ell\ell}$ or from the u_T distributions. As shown in Fig. 14, a sizeable difference is observed between the resolutions of the two observables. Therefore a comparison of the corresponding unfolded distributions is a powerful tool to validate the recoil calibration and the measurement of p_T^W.

For the validation, the p_T^Z spectra are unfolded from the $p_T^{\ell\ell}$ and u_T distributions using the same binning as used for the p_T^W measurement. The uncertainty in the difference can be represented in covariance matrix form, accounting for correlations where relevant. Since the two measurements are extracted from the same events, the statistical correlation is estimated by using the bootstrap method. The compatibility is estimated evaluating the χ^2 computed for the differences of the unfolded distributions. The electron and muon-channel measurements in a given bin are added. The leading uncertainties arise from data statistical uncertainties, hadronic recoil calibration and components of the unfolding uncertainty. Lepton calibrations are only significant at 13 TeV. The number of degrees of freedom is one less than the number of bins due to the additional constraint of the same total cross section extracted from the two observables. Figure 16 compares both measured spectra at each centre-of-mass energy. The χ^2/dof values computed with the 5.02 and 13 TeV datasets are 14.9/14 and 8.7/16, respectively, which represents an excellent compatibility.
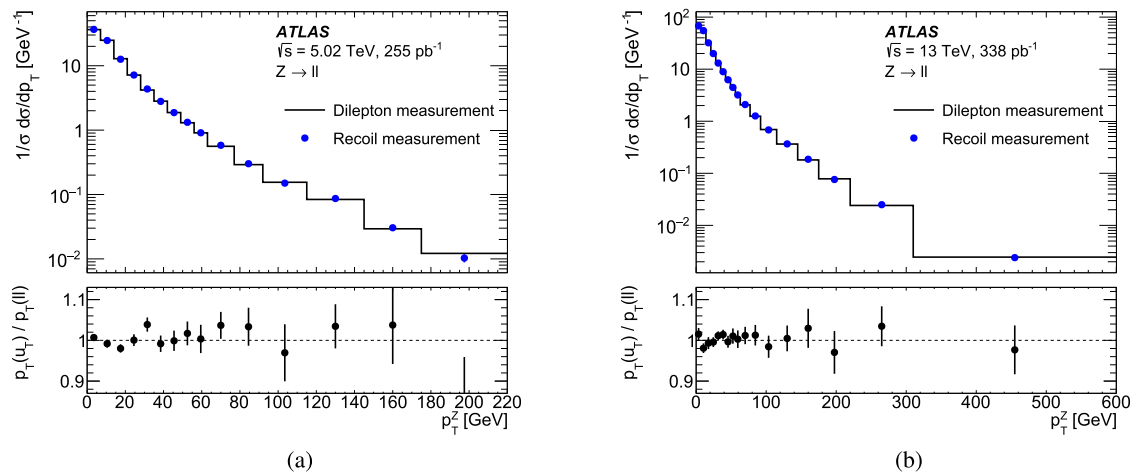
Fig. 16 Spectra of p_T^Z measured using either $p_T^{\ell\ell}$ (black line) or u_T (blue points), at **a** $\sqrt{s} = 5.02$ TeV and **b** $\sqrt{s} = 13$ TeV. The respective measurements, shown in the top panel, largely overlap. The lower panel shows the the ratio of the u_T over the $p_T^{\ell\ell}$ measurements with the uncertainties estimated from the square root of the diagonal elements of the total covariance matrix used to compute the compatibility between them

7 Results

7.1 Combination of electron and muon channels

The electron and muon channel cross sections are combined assuming Gaussian uncertainties, following the best linear unbiased estimator prescription (BLUE) [81,82]. The χ^2 to be minimised is:

$$\chi^2 = \sum_{i,j=1}^{2N} (m_i - \bar{m}_i)\,(C^{-1})_{ij}\,(m_j - \bar{m}_j),\tag{8}$$

where m_i are the measurements in the $i = 1\ldots N$ bins of the distributions in the electron and muon channels, i.e the $2N$-sized vector $\boldsymbol{m} = \{m_1^e, ..., m_N^e; m_1^\mu, ..., m_N^\mu\}$, $\bar{\boldsymbol{m}} = \{\bar{m}_1, ..., \bar{m}_N; \bar{m}_1, ..., \bar{m}_N\}$ is the vector of averages to be determined, and C^{-1} is the inverse of the $2N \times 2N$ measurement covariance matrix. The covariance matrix C is constructed as

$$C_{ij} = C_{ij}^{\text{stat}} + \sum_k C_{ij}^{\text{syst},k},\tag{9}$$

where C^{stat} is the statistical covariance and can be written as

$$C^{\text{stat}} = \begin{pmatrix} C_e^{\text{stat}} & 0 \\ 0 & C_\mu^{\text{stat}} \end{pmatrix},\tag{10}$$

and $C_{e(\mu)}^{\text{stat}}$ are non-diagonal, $N \times N$ covariance matrices resulting from the unfolding of the electron- and muon-channel distributions. For each systematic source of uncertainty k,

$$C_{ij}^{\text{syst},k} = \Gamma_i^k \Gamma_j^k\tag{11}$$

is the product of the effects of varying source k in bins i and j.

The vector $\bar{\boldsymbol{m}}$ that minimises the χ^2 is:

$$\bar{\boldsymbol{m}} = (H^T C^{-1} H)^{-1} H^T C^{-1} \boldsymbol{m},\tag{12}$$

where H is a $2N \times N$ matrix such that $H_{ij} = 1$ when measurement bin $i = 1\cdots 2N$ contributes to the combined value $j = 1\cdots N$, and $H_{ij} = 0$ otherwise. The covariance matrix of the combined measurement is given by:

$$\bar{C} = (H^T C^{-1} H)^{-1}.\tag{13}$$

This procedure is correct in the Gaussian limit and when the uncertainties do not depend on the value of the measured quantity. Many sources of uncertainty are, however, defined relative to the measurement; for example, luminosity or efficiency uncertainties are fixed fractions of the measured cross section. Such uncertainties are then smaller for lower measured values, biasing the average towards the lowest measured cross section. The combination procedure is therefore iterated and the covariance matrix elements are rescaled according to the combined uncertainties of the previous iteration [83]. Stable results are obtained after four iterations.

The uncertainty model is detailed, with about 1800 systematic sources. Lepton-related uncertainties are treated as uncorrelated between measurements at different $\sqrt{s}$, but fully correlated within one $\sqrt{s}$ sample. Recoil uncertainties are similarly correlated between the W^-, W^+ and Z measurements at a given $\sqrt{s}$, with the exception of the $\Sigma \bar{E}_T$ modelling that is only correlated for a type of vector boson. Background uncertainties are treated as fully correlated across all channels, except for the QCD multijet between W and Z sam-
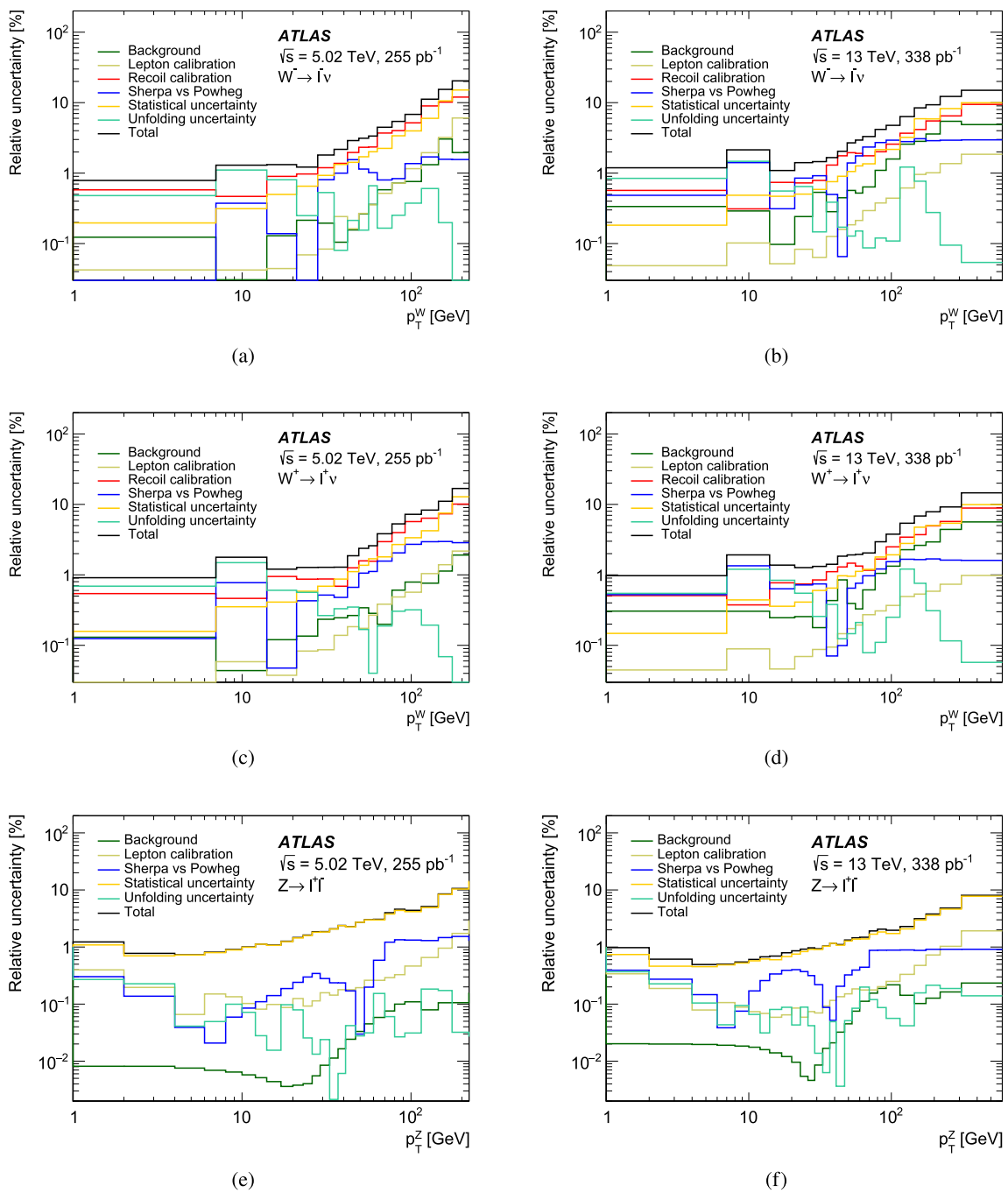
Fig. 17 Uncertainty contributions in the combined normalised p_T distributions for W^- at **a** $\sqrt{s} = 5.02$ TeV and **b** $\sqrt{s} = 13$ TeV, W^+ at **c** $\sqrt{s} = 5.02$ TeV and **d** $\sqrt{s} = 13$ TeV, and Z at **e** $\sqrt{s} = 5.02$ TeV and **f** $\sqrt{s} = 13$ TeV

Table 3 Integrated fiducial cross sections for W^-, W^+ and Z production at $\sqrt{s} = 5.02$ TeV and $\sqrt{s} = 13$ TeV

Process	$\sigma_{\mathrm{fid}}(\sqrt{s} = 5.02\,\mathrm{TeV})$ [pb]	$\sigma_{\mathrm{fid}}(\sqrt{s} = 13\,\mathrm{TeV})$ [pb]
$W^- \to \ell^- \nu$	1384 ± 2 (stat.) ± 5 (syst.) ± 15 (lumi.)	3486 ± 3 (stat.) ± 18 (syst.) ± 34 (lumi.)
$W^+ \to \ell^+ \nu$	2228 ± 3 (stat.) ± 8 (syst.) ± 23 (lumi.)	4571 ± 3 (stat.) ± 21 (syst.) ± 44 (lumi.)
$Z \to \ell\ell$	333.0 ± 1.2 (stat.) ± 2.2 (syst.) ± 3.3 (lumi.)	780.3 ± 2.6 (stat.) ± 7.1 (syst.) ± 7.1 (lumi.)

Table 4 Ratio of integrated fiducial cross sections at $\sqrt{s} = 13$ TeV and $\sqrt{s} = 5.02$ TeV

Process	$\sigma_{\text{fid}}(\sqrt{s} = 13\,\text{TeV})/\sigma_{\text{fid}}(\sqrt{s} = 5.02\,\text{TeV})$
$W^- \to \ell^- \nu$	$2.516 \pm 0.005\,\text{(stat.)} \pm 0.010\,\text{(syst.)} \pm 0.036\,\text{(lumi.)}$
$W^+ \to \ell^+ \nu$	$2.050 \pm 0.003\,\text{(stat.)} \pm 0.008\,\text{(syst.)} \pm 0.029\,\text{(lumi.)}$
$Z \to \ell\ell$	$2.344 \pm 0.011\,\text{(stat.)} \pm 0.011\,\text{(syst.)} \pm 0.032\,\text{(lumi.)}$

Table 5 Integrated fiducial cross sections ratios at $\sqrt{s} = 5.02$ TeV and $\sqrt{s} = 13$ TeV

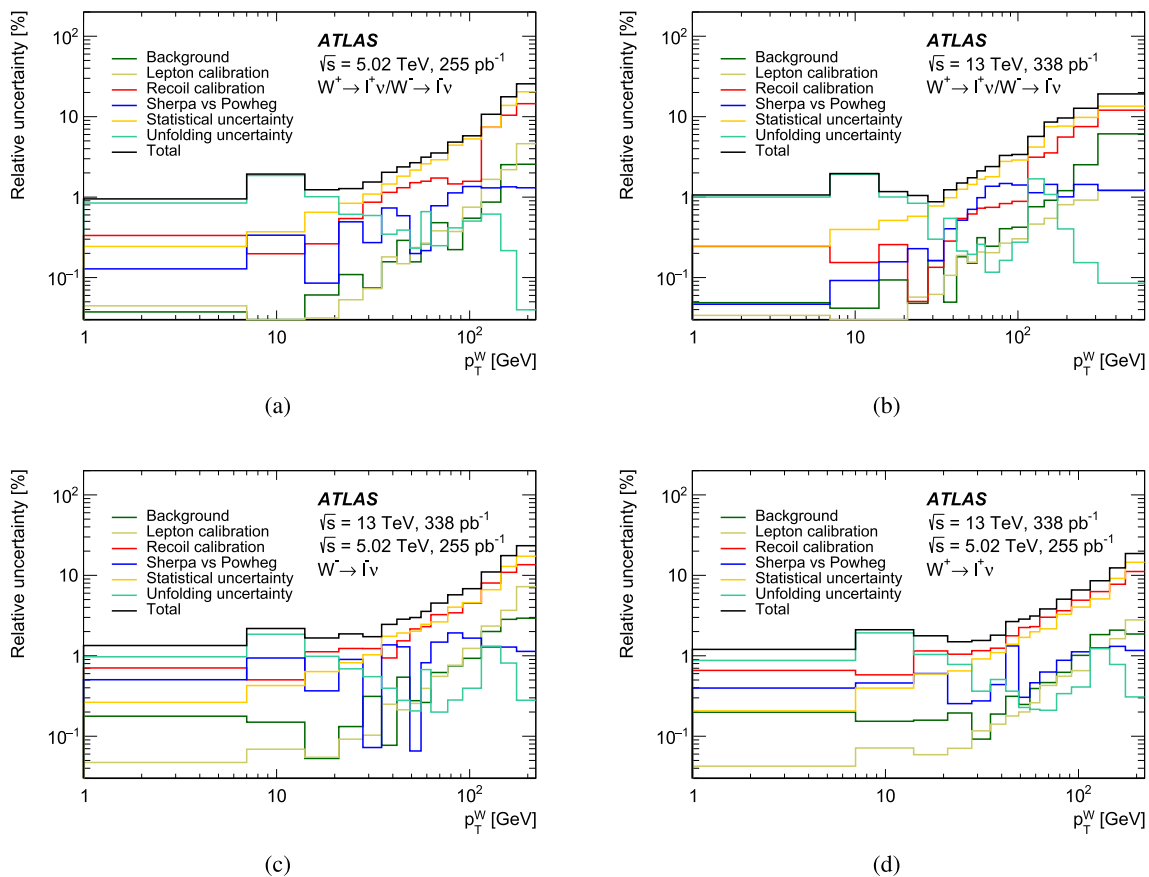| Processes	Cross-section ratio at $\sqrt{s} = 5.02$ TeV	Cross-section ratio at $\sqrt{s} = 13$ TeV
W^+/W^-	$1.609 \pm 0.003\,\text{(stat.)} \pm 0.004\,\text{(syst.)}$	$1.308 \pm 0.003\,\text{(stat.)} \pm 0.004\,\text{(syst.)}$
W^-/Z	$4.16 \pm 0.02\,\text{(stat.)} \pm 0.03\,\text{(syst.)}$	$4.46 \pm 0.02\,\text{(stat.)} \pm 0.05\,\text{(syst.)}$
W^+/Z	$6.69 \pm 0.02\,\text{(stat.)} \pm 0.05\,\text{(syst.)}$	$5.84 \pm 0.02\,\text{(stat.)} \pm 0.06\,\text{(syst.)}$
$W^\pm/Z$	$10.85 \pm 0.04\,\text{(stat.)} \pm 0.07\,\text{(syst.)}$	$10.30 \pm 0.04\,\text{(stat.)} \pm 0.10\,\text{(syst.)}$

Fig. 18 Uncertainty contributions in the ratios of combined normalised p_{T} distributions for W^+/W^- at **a** $\sqrt{s} = 5.02$ TeV and **b** $\sqrt{s} = 13$ TeV as well as the ratios of measurements at different centre-of-mass energies $\sqrt{s} = 13$ TeV to $\sqrt{s} = 5.02$ TeV for **c** W^- and **d** W^+

ples. Unfolding uncertainties are treated as correlated across a given spectrum as well as between the electron and muons channels, but uncorrelated otherwise. The generator uncertainties are separately correlated between all W and all Z analyses across both $\sqrt{s}$ datasets, but uncorrelated between W and Z. Finally, the luminosity systematic uncertainty is correlated among all analyses using a given $\sqrt{s}$ data sample, but treated as uncorrelated between the 5.02 and 13 TeV datasets.

Combinations are performed for absolute and normalised differential cross sections. The compatibility of the electron and muon channel measurements is generally good, as evidenced by combination χ^2 values close to the number of degrees of freedom. The combined uncertainties on the normalised spectra are shown as a function of p_{T}^W and p_{T}^Z in Fig. 17, with an overall precision of about 1% at low p_{T}, reaching about 10% towards the end of the spectrum. The W-boson uncertainties are dominated by unfolding system-

Table 6 Measured integrated fiducial cross sections for W^-, W^+ and Z production at $\sqrt{s} = 5.02$ TeV and $\sqrt{s} = 13$ TeV with total uncertainties ('Data') are compared to DYTURBO predictions at NNLO+NNLL using three different NNLO PDF sets: CT18, MSHT20 and NNPDF3.1. Uncertainties in the theoretical predictions correspond to those obtained by variations of the factorisation and renormalisation scales ('scale') and those computed from the variations in each PDF given by eigenvector or replica variations ('PDF')

PDF set	$W^- \to \ell^- \nu$	$W^+ \to \ell^+ \nu$	$Z \to \ell\ell$
$\sigma_{\text{fid}}(\sqrt{s} = 5.02\,\text{TeV})$ [pb]			
Data	1384 ± 16	2228 ± 25	333.0 ± 4.1
CT18	$1360 \pm 10 \,(\text{scale})^{+30}_{-40}\,(\text{PDF})$	$2200 \pm 10 \,(\text{scale})^{+40}_{-70}\,(\text{PDF})$	$320 \pm 1 \,(\text{scale})^{+5}_{-9}\,(\text{PDF})$
MSHT20	$1351^{+5}_{-6} \,(\text{scale})^{+22}_{-23}\,(\text{PDF})$	$2180 \pm 10 \,(\text{scale})^{+30}_{-40}\,(\text{PDF})$	$324 \pm 1 \,(\text{scale})^{+4}_{-5}\,(\text{PDF})$
NNPDF31	$1381 \pm 6 \,(\text{scale}) \pm 16 \,(\text{PDF})$	$2232^{+8}_{-9} \,(\text{scale}) \pm 25 \,(\text{PDF})$	$329 \pm 1 \,(\text{scale}) \pm 4 \,(\text{PDF})$
$\sigma_{\text{fid}}(\sqrt{s} = 13\,\text{TeV})$ [pb]			
Data	3486 ± 38	4571 ± 49	780.3 ± 10.4
CT18	$3410^{+40}_{-20} \,(\text{scale})^{+60}_{-100}\,(\text{PDF})$	$4460^{+40}_{-30} \,(\text{scale})^{+80}_{-130}\,(\text{PDF})$	$748^{+5}_{-4} \,(\text{scale})^{+18}_{-25}\,(\text{PDF})$
MSHT20	$3400^{+40}_{-20} \,(\text{scale})^{+40}_{-60}\,(\text{PDF})$	$4460^{+40}_{-30} \,(\text{scale})^{+60}_{-70}\,(\text{PDF})$	$763^{+6}_{-4} \,(\text{scale})^{+9}_{-12}\,(\text{PDF})$
NNPDF31	$3450^{+40}_{-20} \,(\text{scale}) \pm 30 \,(\text{PDF})$	$4510^{+40}_{-30} \,(\text{scale}) \pm 40 \,(\text{PDF})$	$769^{+6}_{-4} \,(\text{scale}) \pm 7 \,(\text{PDF})$

atic uncertainties at low p_T^W, and statistical uncertainties at high p_T^W. The generator dependence of the recoil calibration procedure is sizeable at 13 TeV. The Z-boson uncertainties are fully dominated by statistical uncertainties.

7.2 Integrated cross sections and distribution ratios

Integrated fiducial cross sections are obtained by summing the measured distributions over a given spectrum, and the corresponding uncertainty is given by summing the corresponding covariance matrix elements. The definition of the fiducial volume is given in Sect. 6, and the results are summarised in Table 3. Experimental systematic uncertainties excluding the luminosity are at the level of 0.4 and 0.5% for W-boson production at 5.02 and 13 TeV, respectively. The corresponding numbers for the Z-boson cross sections are 0.7 and 0.9%. The luminosity uncertainty is 1.0% at 5.02 TeV, and 0.9% at 13 TeV.

Similar measurements at 5.02 TeV previously published by ATLAS in Ref. [84] are not directly comparable to the new results due to small differences in the fiducial volume definition. However, the relative uncertainties are improved by about a factor of two due to the larger dataset and improved experimental calibrations, including the luminosity measurement. The measurements at 13 TeV are compatible with those performed by ATLAS with the very early Run 2 data with a luminosity of just 81 pb^{-1} [85] and improve the precision by a factor of 3.5 for the W measurement and a factor of 1.7 for the Z measurement. The 13 TeV Z-boson measurement is also compatible with the improved ATLAS measurement of Ref. [86] that has a slightly lower precision because of the preliminary luminosity calibration used then.

The measured ratios of integrated fiducial cross sections are given in Tables 4 and 5. As expected, all cross sections rise with $\sqrt{s}$, as lower parton momentum fractions x are probed and the densities of sea quarks and antiquarks rise towards low x. The increase in the W^+ cross section is the smallest because it has the largest contribution from higher x valence quarks that contribute less to the phase space measured at higher $\sqrt{s}$.

Cross-section ratios are also formed of the absolute and normalised differential distributions, both between different processes at a given $\sqrt{s}$ and between the same processes at different $\sqrt{s}$. Theoretically, ratios probe specific aspects of the modelling of W and Z production. The W^+/W^- and $W^\pm/Z$ ratios are expected to be relatively insensitive to universal resummation effects, but the low-p_T range is sensitive to the different initial quark flavours and specifically the contribution of heavy quarks. Experimentally, some of these ratios benefit from a partial cancellation of systematic uncertainties. Most notably, the recoil calibration at a given $\sqrt{s}$ is strongly correlated between the W^+ and W^- measurements as it stems from the same calibration, mostly using Z events. Figure 18a, b illustrates how the associated uncertainties largely cancel in the W^+/W^- ratios, resulting in a measurement uncertainty of around 1% at low p_T. By contrast, since this calibration is obtained independently at $\sqrt{s} = 5.02$ TeV and 13 TeV, the related uncertainty increases in a ratio, as shown in Fig. 18c, d and the typical precision is around 2% at lower p_T, increasing significantly towards higher p_T. The electron–muon combination of these ratios have generally very good χ^2/dof.

Table 7 Ratios of measured integrated fiducial cross sections at $\sqrt{s} =$ 13 TeV and $\sqrt{s} = 5.02$ TeV for W^-, W^+ and Z production with total uncertainties ('Data') are compared to DYTURBO predictions at NNLO+NNLL using three different NNLO PDF sets: CT18, MSHT20 and NNPDF3.1

PDF set	$W^- \to \ell^- \nu$	$W^+ \to \ell^+ \nu$	$Z \to \ell\ell$
$\sigma_{\text{fid}}(\sqrt{s} = 13\,\text{TeV})/\sigma_{\text{fid}}(\sqrt{s} = 5.02\,\text{TeV})$			
Data	2.516 ± 0.038	2.050 ± 0.030	2.344 ± 0.036
CT18	$2.499^{+0.017}_{-0.005}$ (scale)$^{+0.043}_{-0.046}$ (PDF)	$2.029^{+0.010}_{-0.007}$ (scale)$^{+0.029}_{-0.023}$ (PDF)	$2.335^{+0.012}_{-0.009}$ (scale)$^{+0.049}_{-0.038}$ (PDF)
MSHT20	$2.515^{+0.017}_{-0.005}$ (scale)$^{+0.018}_{-0.020}$ (PDF)	$2.040^{+0.010}_{-0.007}$ (scale)$^{+0.014}_{-0.015}$ (PDF)	$2.358^{+0.012}_{-0.009}$ (scale)$^{+0.018}_{-0.022}$ (PDF)
NNPDF31	$2.500^{+0.017}_{-0.005}$ (scale) ± 0.031 (PDF)	$2.022^{+0.010}_{-0.007}$ (scale) ± 0.029 (PDF)	$2.335^{+0.012}_{-0.009}$ (scale) ± 0.026 (PDF)

Table 8 Ratios of measured integrated fiducial cross sections of W^+/W^- and $W^\pm/Z$ for the $\sqrt{s} = 5.02$ TeV and $\sqrt{s} = 13$ TeV data with total uncertainties ('Data') are compared to DYTURBO predictions at NNLO+NNLL using three different NNLO PDF sets: CT18, MSHT20 and NNPDF3.1

PDF set	W^+/W^-	$W^\pm/Z$
Cross-section ratio at $\sqrt{s} = 5.02$ TeV		
Data	1.609 ± 0.005	10.85 ± 0.08
CT18	$1.612^{+0.001}_{-0.003}$ (scale)$^{+0.018}_{-0.028}$ (PDF)	$11.13^{+0.04}_{-0.06}$ (scale) ± 0.11 (PDF)
MSHT20	$1.618^{+0.001}_{-0.003}$ (scale) ± 0.008 (PDF)	$10.92^{+0.04}_{-0.06}$ (scale)$^{+0.07}_{-0.05}$ (PDF)
NNPDF31	$1.616^{+0.001}_{-0.003}$ (scale) ± 0.018 (PDF)	$10.98^{+0.04}_{-0.06}$ (scale) ± 0.15 (PDF)
Cross-section ratio at $\sqrt{s} = 13$ TeV		
Data	1.308 ± 0.005	10.30 ± 0.11
CT18	$1.309^{+0.000}_{-0.003}$ (scale)$^{+0.012}_{-0.007}$ (PDF)	10.53 ± 0.03 (scale)$^{+0.13}_{-0.15}$ (PDF)
MSHT20	$1.312^{+0.000}_{-0.003}$ (scale)$^{+0.005}_{-0.004}$ (PDF)	10.29 ± 0.03 (scale)$^{+0.07}_{-0.05}$ (PDF)
NNPDF31	$1.307^{+0.000}_{-0.003}$ (scale) ± 0.003 (PDF)	10.37 ± 0.03 (scale) ± 0.06 (PDF)

7.3 Comparison to predictions

The final measurements, obtained from the combination of electron and muon channels, are compared to an extensive list of predictions from higher-order resummed predictions and MC event generators. As a representative example of resummation predictions, calculations from DYTURBO v1.2.3 are presented. These predictions are computed by performing the resummation of logarithmically-enhanced contributions in the small q_T region of the lepton pairs at NNLL accuracy and also include the corresponding finite-order QCD contributions at NNLO (corrections up to α_S^2). Three different NNLO PDF sets are used: CT18 [87], MSHT20 [88] and NNPDF3.1 [89]. Theoretical uncertainties are estimated through variations of the nominal factorisation, renormalisation and resummation scales by a factor of two up and down, excluding variations in opposite directions, and taking the envelope of all variations. The PDF uncertainties for each set are estimated by calculating the variations for all eigenvector or replicas and combining the results following the prescriptions relevant for each PDF set. When computing the uncertainties in ratios or across differential spectra, the effect of a certain PDF eigenvector or replica variation is taken as correlated. Similarly, the effect of each scale variation is treated as fully correlated between all vector bosons, $\sqrt{s}$ and across

spectra. Additional comparisons at $\sqrt{s} = 13$ TeV to predictions by the RADISH program are presented in Appendix B.

The integrated cross-section measurements and ratios presented in Sect. 7.2 are compared to the integrated DYTURBO predictions in Table 6. Good agreement with the central values of the NNPDF3.1 already within the experimental uncertainties is seen, while the CT18 and MSHT20 predictions tend to underestimate the cross sections, similar to previous observations [84,86]. When considering the dominant PDF uncertainties, the agreement with all PDF sets is satisfactory. Table 7 compares the measured ratios of cross sections at $\sqrt{s} = 13$ TeV and $\sqrt{s} = 5.02$ TeV to the predictions. The increases in cross section are well predicted by all PDF sets. Table 8 then presents ratios at fixed $\sqrt{s}$, which are again generally compatible with the predictions. The $W^\pm/Z$ ratios predicted by CT18 are 1–2 standard deviations above the data, which is similar to an observation at $\sqrt{s} = 7$ TeV attributed to the strange-quark density [77].

Differential predictions are also obtained from MC event generators that combine LO or NLO matrix elements and match them to parton showers and models for underlying event, hadronisation and particle decay. The MC samples already described in Sect. 2.3, namely POWHEG+PYTHIA 8 with the AZNLO tune and SHERPA [2.2.1/2.2.5], are included, however without the reweighting to match the reconstruction-level data described in Sect. 6.1. A POWHEG+HERWIG 7 sam-
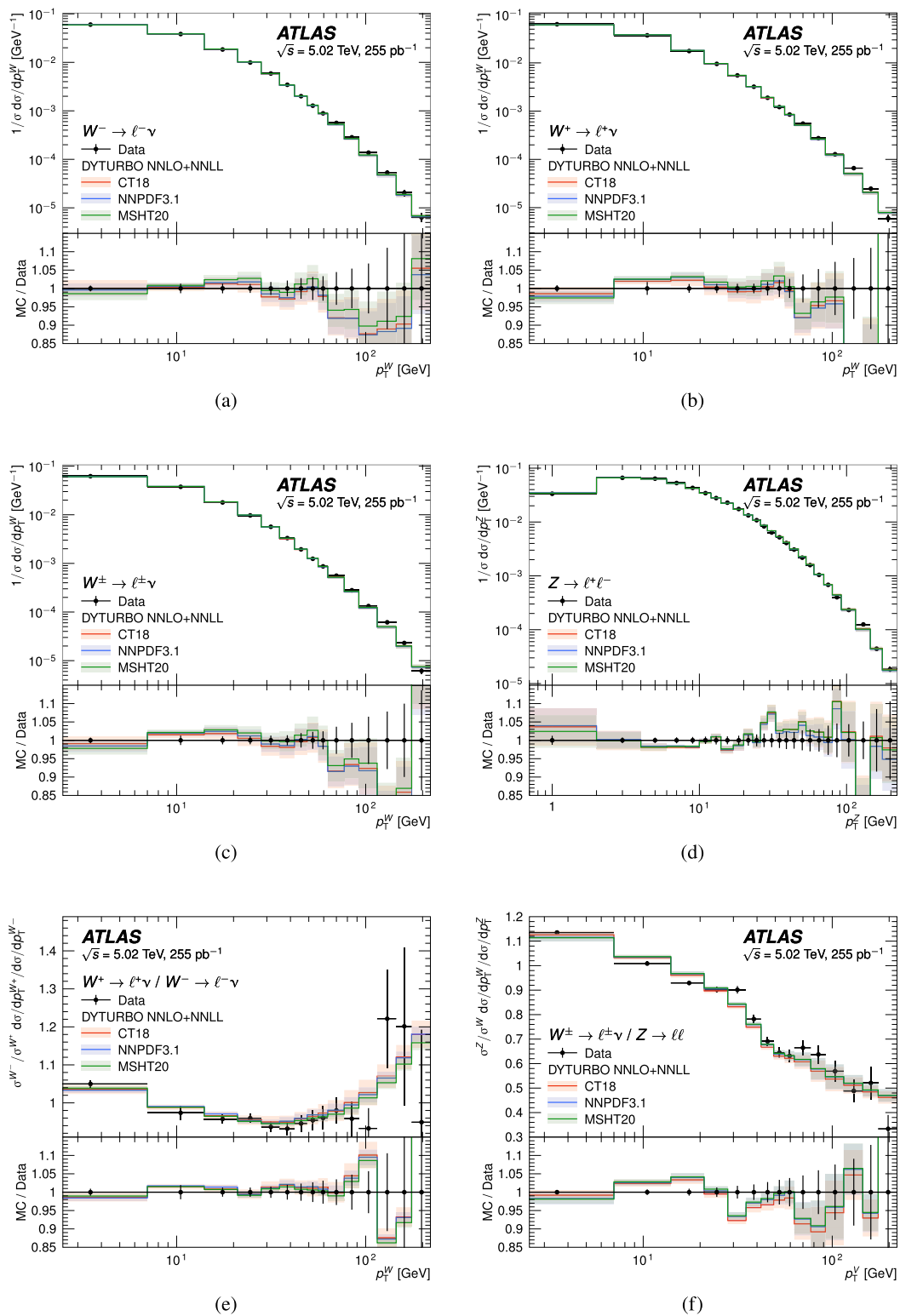
Fig. 19 Measurements of normalised differential distributions at $\sqrt{s} = 5.02$ TeV (black points) for **a** W^-, **b** W^+, **c** the sum $W^\pm$, **d** Z as well as the ratios, **e** W^+/W^- and **f** $W^\pm/Z$ compared to DYTURBO predictions with different PDF sets (coloured lines and PDF and scale uncertainties as shaded band) as described in the text. The lower panels show the ratio of prediction to data with data markers centred at one and error bars giving the size of the total measurement uncertainties

Fig. 20 Measurements of normalised differential distributions at $\sqrt{s} = 5.02$ TeV (black points) for **a** W^-, **b** W^+, **c** the sum $W^\pm$, **d** Z as well as the ratios, **e** W^+/W^- and **f** $W^\pm/Z$ compared to a variety of MC predictions (coloured lines) as described in the text. The lower panels show the ratio of prediction to data with data markers centred at one and error bars giving the size of the total measurement uncertainties
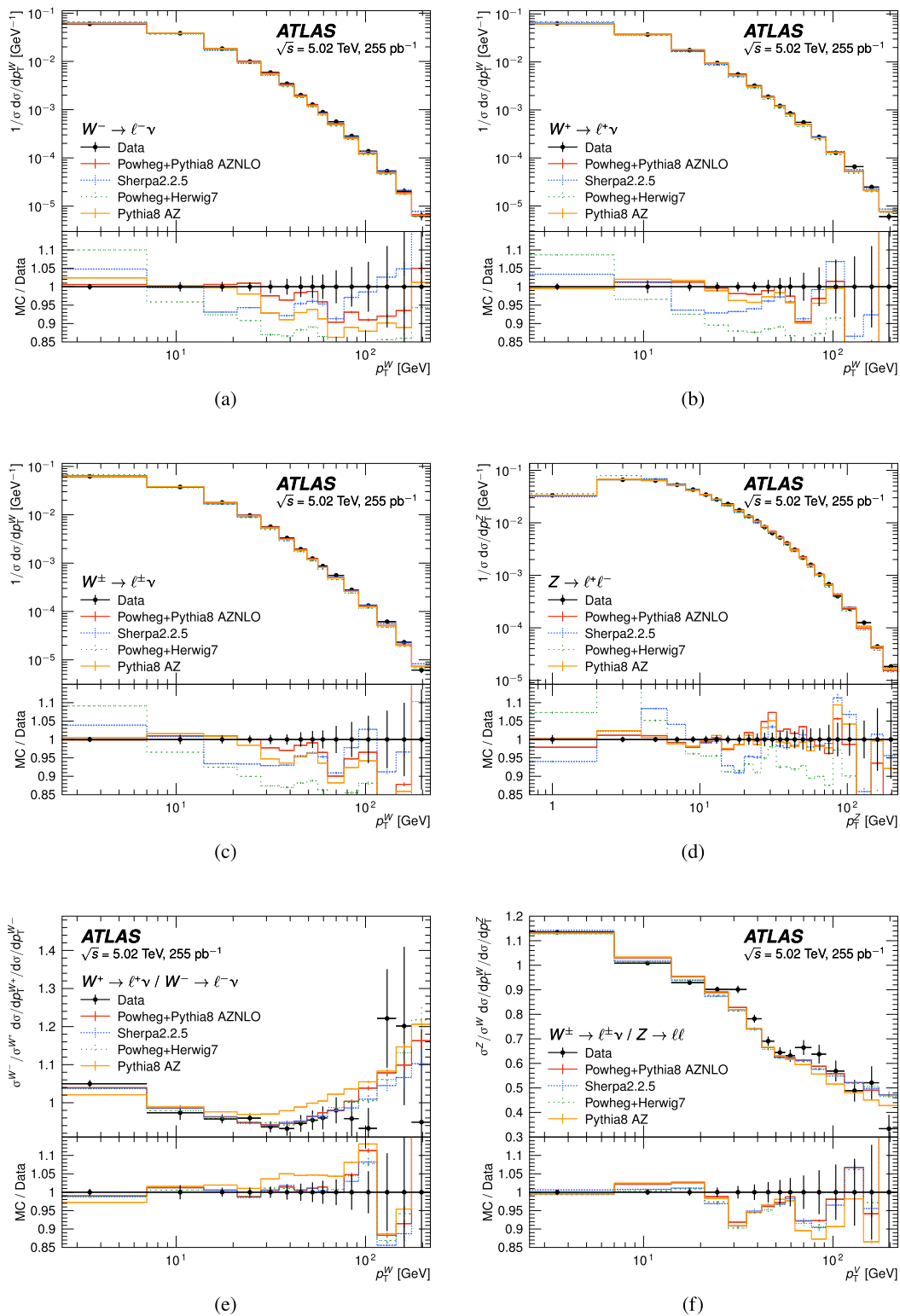
Fig. 21 Measurements of normalised differential distributions at $\sqrt{s} = 13$ TeV (black points) for **a** W^-, **b** W^+, **c** the sum $W^\pm$, **d** Z as well as the ratios, **e** W^+/W^- and **f** $W^\pm/Z$ compared to DYTURBO predictions with different PDF sets (coloured lines and PDF and scale uncertainties as shaded band) as described in the text. The lower panels show the ratio of prediction to data with data markers centred at one and error bars giving the size of the total measurement uncertainties
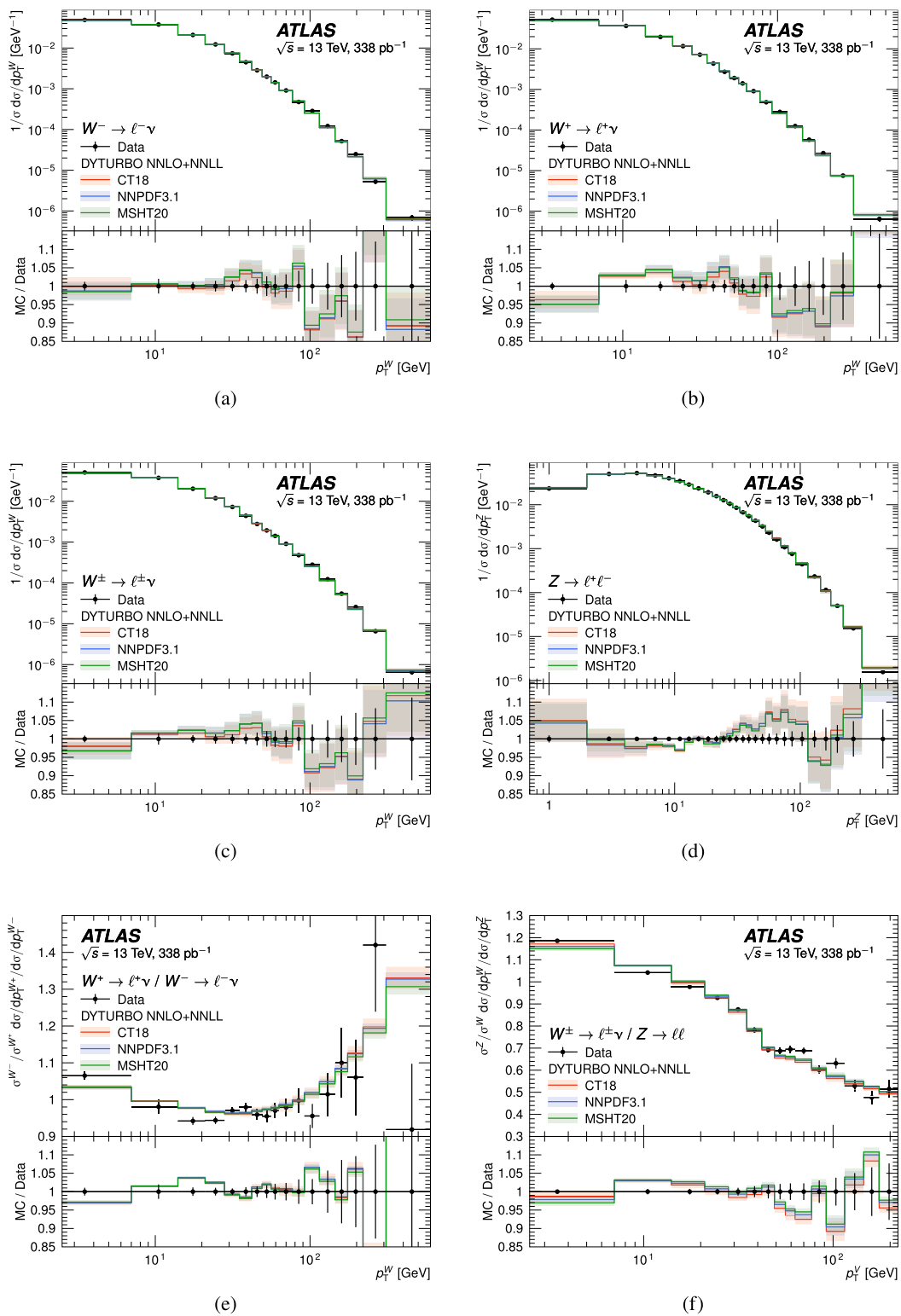
(a)

(b)

(c)

(d)

(e)

(f)

Fig. 22 Measurements of normalised differential distributions at $\sqrt{s} = 13$ TeV (black points) for **a** W^-, **b** W^+, **c** the sum $W^\pm$, **d** Z as well as the ratios, **e** W^+/W^- and **f** $W^\pm/Z$ compared to a variety of MC predictions (coloured lines) as described in the text. The lower panels show the ratio of prediction to data with data markers centred at one and error bars giving the size of the total measurement uncertainties
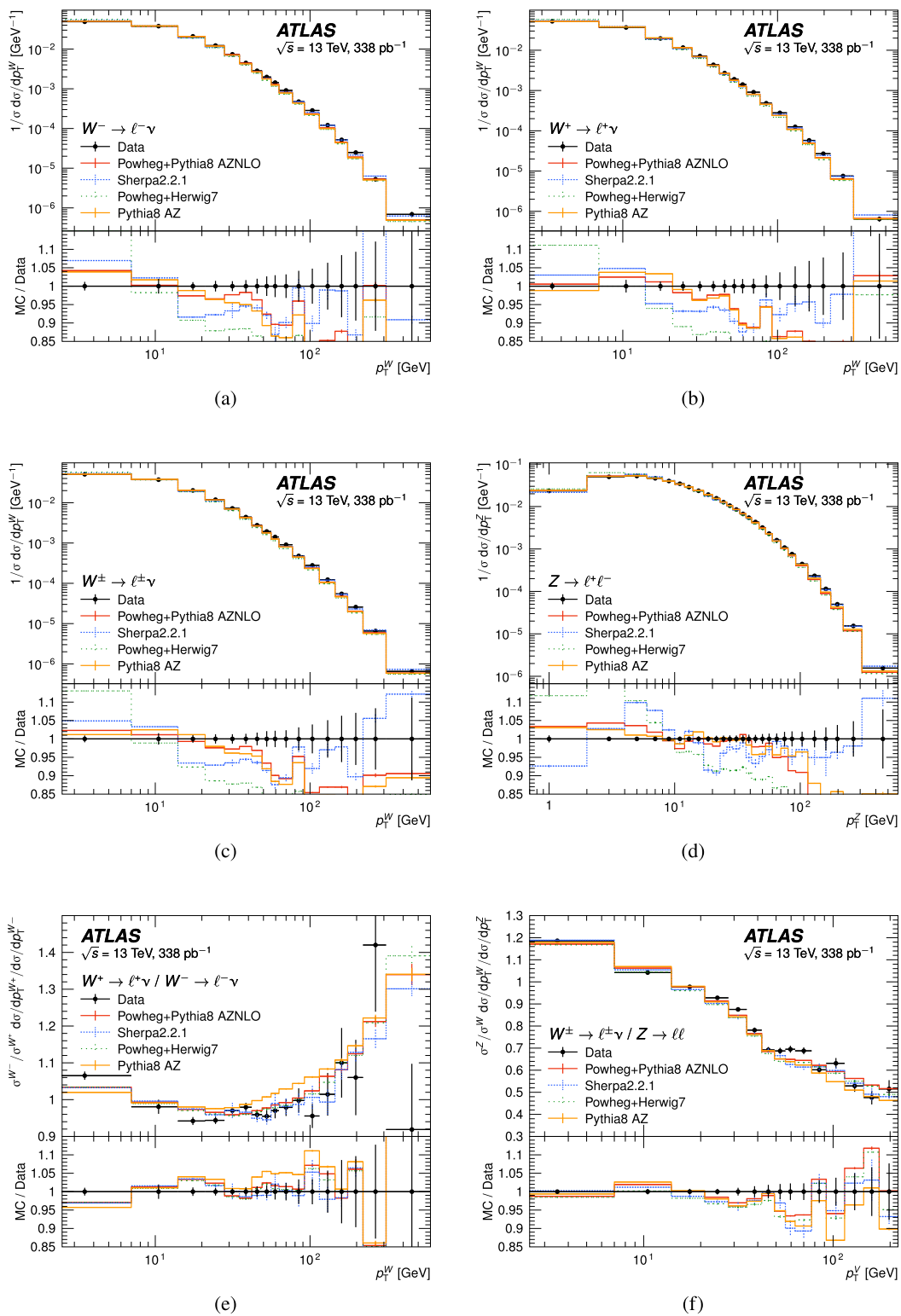
(a)   (b)

(c)   (d)

Fig. 23 Ratios of normalised differential distributions at $\sqrt{s} = 13$ TeV to $\sqrt{s} = 5.02$ TeV (black points) for **a**, **c** $W^{\pm}$ and **b**, **d** Z compared to **a**, **b** DYTURBO predictions with different PDF sets or **b**, **d** a variety of MC predictions (coloured lines, PDF and scale uncertainties as shaded band for DYTURBO) as described in the text. The lower panels show the ratio of prediction to data with data markers centred at one and error bars giving the size of the total measurement uncertainties
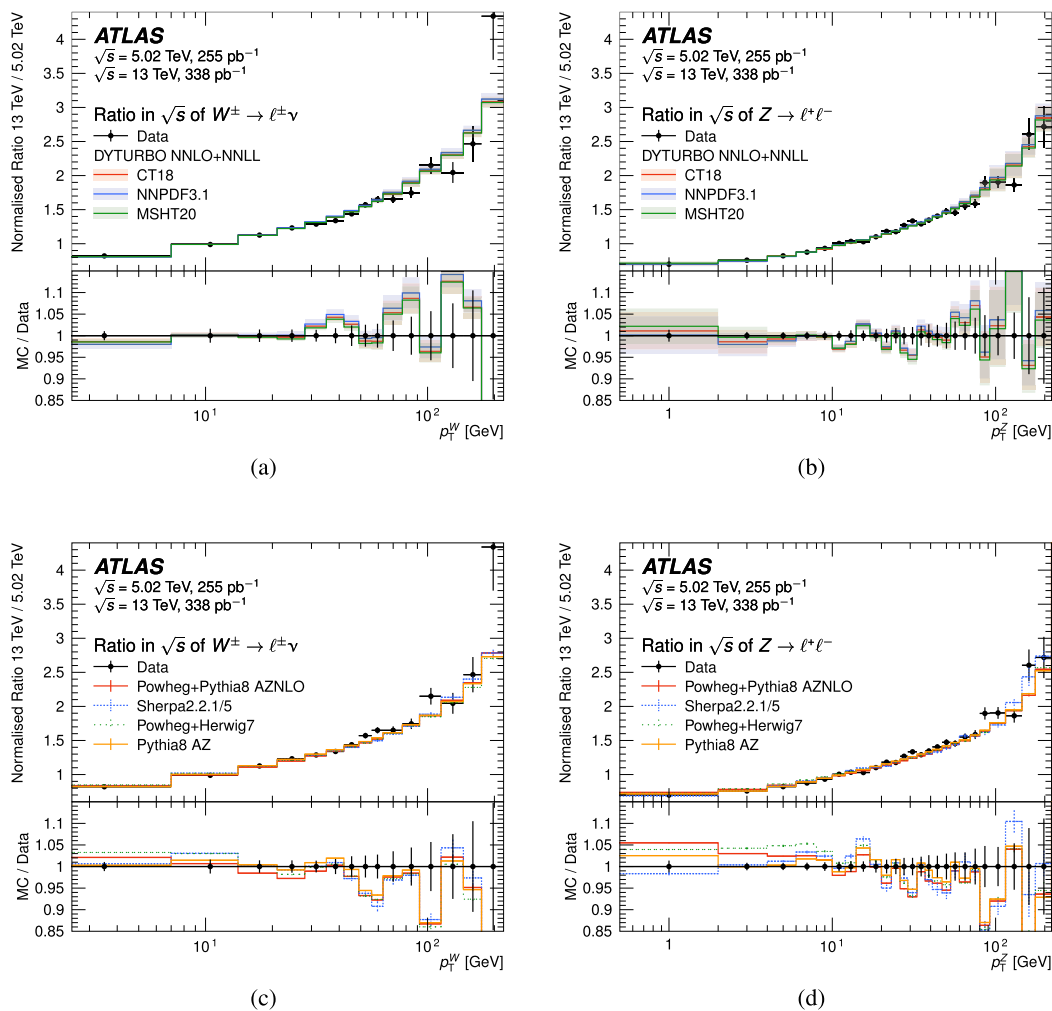
ple is simulated using a similar set-up as POWHEG+PYTHIA 8, but using HERWIG 7 [13,90] for the parton shower, hadronisation and underlying event using the default tune. A prediction with PYTHIA 8 alone matches LO matrix elements to a parton shower with the CTEQ6L1 PDF set and the AZ parameter set tuned to describe 7 TeV $p_T^{\ell\ell}$ and ϕ^* measurements [15]. Further predictions at 13 TeV with multijet-merged predictions at NLO as described in Ref. [91] are prepared with SHERPA [2.2.11] and MADGRAPH_AMC@NLO FxFx+PYTHIA 8 [92,93] and presented in Appendix C. The fiducial predictions are extracted with the RIVET toolkit [94].

To separate overall normalisation and shape effects, all differential comparisons are shown using normalised spectra. Figures 19 and 20 compare the measurements and some ratios at $\sqrt{s} = 5.02$ TeV to DYTURBO and the MC predictions, respectively. The equivalent comparisons at $\sqrt{s} = 13$ TeV are given in Figs. 21 and 22.

As expected, many features are broadly observed across all final states and in both $\sqrt{s}$ datasets. First, the data is precise and discriminating up to about $p_T^V = 100$ GeV at 5.02 TeV and $p_T^V = 200$ GeV at 13 TeV. The DYTURBO resummed predictions show the best agreement across the spectrum and generally match the data at the percent level. When focusing on the lower $p_T^V < 30$ GeV region, the W^+ measurements show overall the largest deviation from the DYTURBO predictions. The three investigated PDF sets produce only small differences in the shapes of the distributions, but theoretical uncertainties at higher p_T^V are significant, dominated by the scale variations.

The MC predictions that were tuned to $\sqrt{s} = 7$ TeV data, POWHEG+PYTHIA 8 AZNLO and PYTHIA 8 AZ, describe reasonably well the low-p_T^V region that is relevant for the measurement of the W-boson mass. However, they show worse agreement for $p_T^V > 40$ GeV. The POWHEG+HERWIG 7 pre-

dictions does not perform well across the whole spectrum. The SHERPA [2.2.1/2.2.5] predictions match the data best at higher p_T^V, but they deviate significantly in the region $p_T^V \lesssim 20\,\mathrm{GeV}$, a behaviour that was improved in SHERPA [2.2.11] by optimising the matching conditions [91], see also Appendix C.

The ratios W^+/W^- and $W^\pm/Z$ are measured to percent-level precision and show some interesting features at both $\sqrt{s}$ values. The differences between the predictions and uncertainties shrink in these ratios. The PYTHIA 8 AZ prediction is clearly ruled out by the data in the W^+/W^- ratio. However, this is an effect of mismodelled angular decay distributions and thus the fiducial acceptance. The ratios at $\sqrt{s} = 13\,\mathrm{GeV}$ show the largest differences between data and predictions at lower $p_T^V < 30\,\mathrm{GeV}$.

The ratios of normalised differential distributions at $\sqrt{s} = 13\,\mathrm{TeV}$ to $\sqrt{s} = 5.02\,\mathrm{TeV}$ are shown in Fig. 23. Here DYTURBO is in excellent agreement with the data, while several MC predictions fail to follow the energy dependence in the low p_T^V region correctly.

8 Conclusion

This paper presented an extensive set of measurements of W- and Z-boson p_T distributions at two centre-of-mass energies: $\sqrt{s} = 5.02\,\mathrm{TeV}$ and $\sqrt{s} = 13\,\mathrm{TeV}$. The measurements were performed with pp collision data delivered by the LHC and recorded by the ATLAS detector in special low pile-up conditions in 2017 and 2018.

While the p_T^Z distribution had been measured in great detail previously using the dilepton system produced in Z-boson decays, the direct measurement of the p_T^W distribution relies on the full reconstruction of the hadronic recoil in W-boson events. The dedicated datasets, reconstruction and calibration techniques allowed an unprecedented granularity of about 7 GeV in p_T^W and a final precision at the level of $1-2\%$. All measurements have been performed in the electron and muon decays of the bosons and the results are combined.

A unique feature of the analysis presented is the wide coverage of six high-precision absolute and normalised cross section distributions for the three vector boson final states W^-, W^+ and Z at two well separated centre-of-mass energies. In addition, integrated fiducial cross sections and a variety of ratios are presented. The integrated results in particular profit from the very precise luminosity measurement with an uncertainty of $0.9-1.0\%$, leading to improvements in the precision compared to existing results by a factor of two or more. The integrated results and ratios are generally compatible with DYTURBO predictions at order NNLO+NNLL.

The comparison of differential spectra to different MC simulations shows a variety of deficiencies in the description of the transverse momentum distribution; many are common for all vector bosons. The agreement is better at $\sqrt{s} = 5.02\,\mathrm{TeV}$, especially for those predictions that were tuned to Z-boson measurements at $\sqrt{s} = 7\,\mathrm{TeV}$. The ratios show generally a better agreement as expected due to the similarity in the processes. The higher-order resummed predictions from DYTURBO match the data best across the spectrum. All predictions show similar disagreements with the data in the W^+/W^- and $W^\pm/Z$ ratios, especially at $\sqrt{s} = 13\,\mathrm{TeV}$.

These detailed measurements are of great importance for future measurements of the W-boson mass that rely on a good modelling of the p_T^W spectrum. The results can be used to test and constrain various theoretical uncertainties affecting the predictions. Different contributions may be understood from the different ranges of parton momentum fractions and initial parton flavours that are probed by W^-, W^+ and Z production at $\sqrt{s} = 5.02\,\mathrm{TeV}$ and $\sqrt{s} = 13\,\mathrm{TeV}$.

Appendix

A Measurement uncertainty breakdown for all channels

The uncertainty contributions in the unfolded, normalised p_T^W and p_T^Z spectra for each decay channel are given in Figs. 24, 25, 26 and 27 for the W-boson and Z-boson analyses on the 5.02 TeV (13 TeV) datasets.

(a)

(b)

(c)

(d)
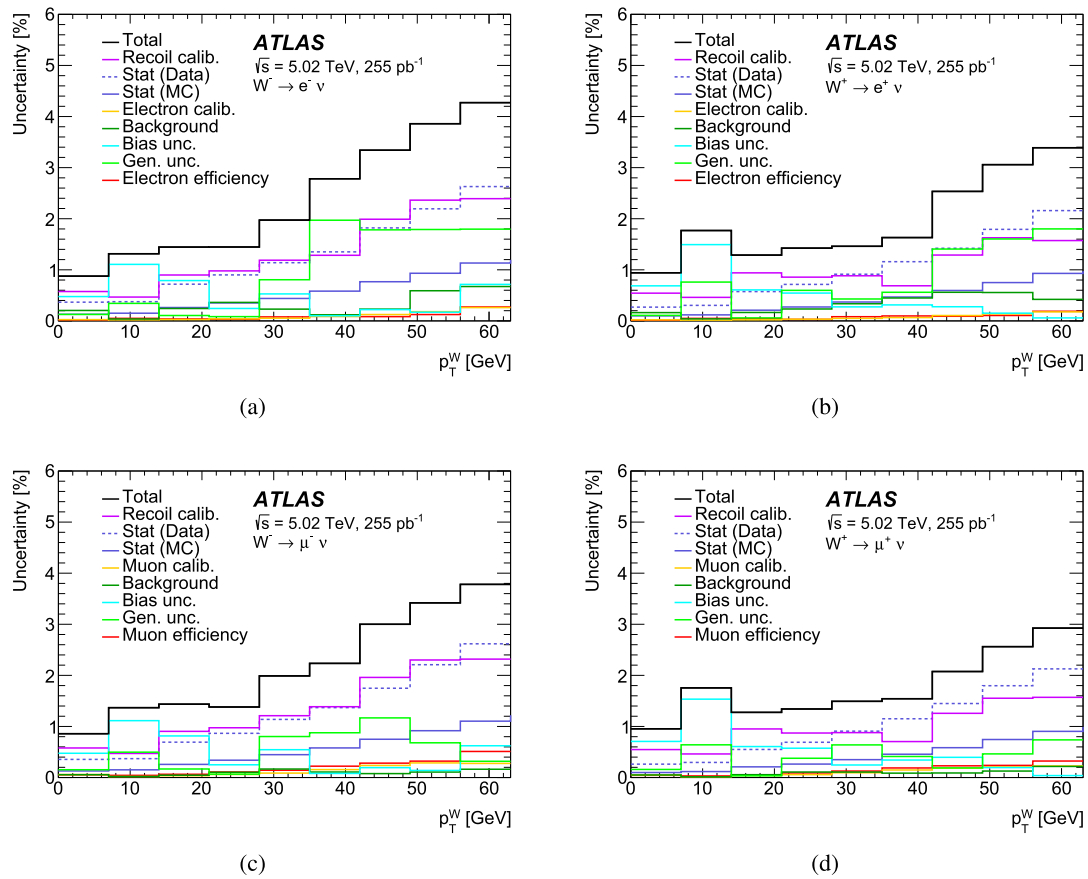
Fig. 24 Uncertainty contributions in the normalised p_T^W distribution in the **a** $W^- \rightarrow e^-\nu$, **b** $W^+ \rightarrow e^+\nu$, **c** $W^- \rightarrow \mu^-\nu$ and **d** $W^+ \rightarrow \mu^+\nu$ channels for the $\sqrt{s} = 5.02$ TeV dataset, focusing on the low $p_T^W < 63$ GeV region. The 'Background' component refers to the sum of uncertainties in the normalisation of the simulated background samples and the uncertainties in the yield and shape of the multijet back-ground estimate. The 'Electron efficiency' and 'Muon efficiency' components refer to the total uncertainty in the lepton efficiency scale factors: electron trigger, reconstruction, identification, isolation (electron channel) and muon trigger, identification, track-to-vertex association, isolation (muon channel). The uncertainties are shown as a percentage of the unfolded data per p_T bin

(a)

(b)

(c)

(d)

Fig. 25 Uncertainty contributions in the normalised p_T^W distribution in the **a** $W^- \to e^-\nu$, **b** $W^+ \to e^+\nu$, **c** $W^- \to \mu^-\nu$ and **d** $W^+ \to \mu^+\nu$ channels for the $\sqrt{s} = 13$ TeV dataset, focusing on the low $p_T^W < 63$ GeV region. The 'Background' component refers to the sum of uncertainties in the normalisation of the simulated background samples and the uncertainties in the yield and shape of the multijet background estimate. The 'Electron efficiency' and 'Muon efficiency' components refer to the total uncertainty in the lepton efficiency scale factors: electron trigger, reconstruction, identification, isolation (electron channel) and muon trigger, identification, track-to-vertex association, isolation (muon channel). The uncertainties are shown as a percentage of the unfolded data per p_T bin

(a)

(b)

Fig. 26 Uncertainty contributions in the normalised p_T^Z distribution in the **a** $Z \to ee$ and **b** $Z \to \mu\mu$ decay channels for the $\sqrt{s} = 5.02$ TeV dataset. The 'Background' component refers to the sum of uncertainties in the normalisation of the simulated background samples and the uncertainties in the yield and shape of the multijet background estimate. The 'SF tot.' component refers to the total uncertainty in the lepton efficiency scale factors: electron trigger, reconstruction, identification, isolation (electron channel) and muon trigger, identification, track-to-vertex association, isolation (muon channel). The uncertainties are shown as a percentage of the unfolded data per p_T bin

(a)

(b)

Fig. 27 Uncertainty contributions in the normalised p_T^Z distribution in the **a** $Z \to ee$ and **b** $Z \to \mu\mu$ decay channels for the $\sqrt{s} = 13$ TeV dataset. The 'Background' component refers to the sum of uncertainties in the normalisation of the simulated background samples and the uncertainties in the yield and shape of the multijet background esti-

mate. The 'SF tot.' component refers to the total uncertainty in the lepton efficiency scale factors: electron trigger, reconstruction, identification, isolation (electron channel) and muon trigger, identification, track-to-vertex association, isolation (muon channel). The uncertainties are shown as a percentage of the unfolded data per p_T bin

B Comparisons to RADISH+NNLOJET predictions and DYTURBO uncertainty composition

Figure 28 compares the measurements at $\sqrt{s} = 13$ TeV to predictions obtained by the RADISH program [9,96]. Compared to the DYTURBO predictions shown in the main body, these were computed at a higher perturbative accuracy by matching to a NNLO prediction of Z+jet production $(O(\alpha_s^3))$ from NNLOJET [97] with resummation of $\log(m_{\ell\ell}/p_T)$ terms at next-to-next-to-next-to-leading-logarithm (N^{3}LL) accuracy [98]. The NNPDF3.1 set of PDFs is used with QCD scales set to $\mu_r = \mu_f = \sqrt{(m_{\ell\ell})^2 + (p_T^V)^2}$ and the resummation scale set to $Q = m_{\ell\ell}/2$. Uncertainties in this prediction are derived from variations of μ_r and μ_f and two variations of Q by a factor of two up and down. As comparison, the DYTURBO predictions are shown as computed with the same PDF set and the uncertainty decomposed into those originating from the PDF variations and the scale variations.

At $\sqrt{s} = 5.02$ TeV the RADISH+NNLOJET predictions were not available, therefore Figs. 29 and 30 repeat the DYTURBO predictions as shown in the main body, but provide the same decomposition of the uncertainties into those estimated by QCD scale variations and those from PDFs.

C Comparisons to multijet-merged predictions

Figure 31 compares the measurements at $\sqrt{s} = 13$ TeV to three multijet-merged predictions that were discussed in detail in Ref. [91]. All samples show a similar behaviour across the W^-, W^+, Z measurements and are very close to the data for the W^+/W^- ratio. The SHERPA [2.2.11] sample improves the behaviour of the SHERPA [2.2.1] sample in the region $p_T = 20$ GeV, where matrix-element and parton shower emissions are matched. Both SHERPA samples have some room for improvement in the region of lowest $p_T \lesssim 10$ GeV. The MADGRAPH_AMC@NLO FxFx+PYTHIA 8 is very close to SHERPA [2.2.11] at higher $p_T > 40$ GeV and appears to behave better at low $p_T < 10$ GeV. It shows, however, some excess over data for $p_T = 20$–30 GeV.

D Total integrated W and Z cross sections and ratios

The total production cross section for $pp \to W \to \ell\nu$ and $pp \to Z/\gamma^* \to \ell\ell$ may be obtained from the fiducial measurements presented in this paper in Table 3 through theo-
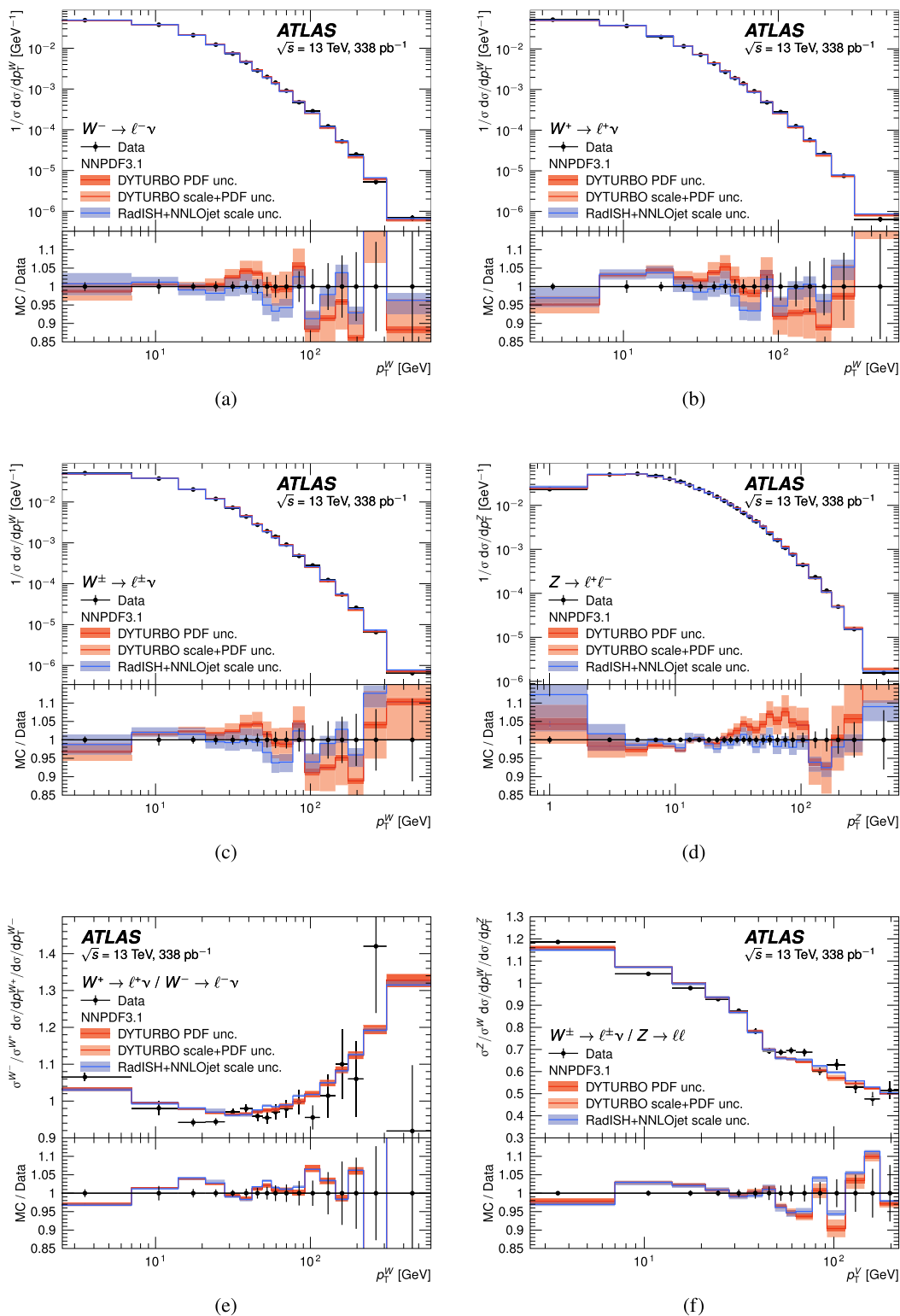
Fig. 28 Measurements of normalised differential distributions at $\sqrt{s} = 13$ TeV (black points) for **a** W^-, **b** W^+, **c** the sum $W^\pm$, **d** Z as well as **e** the ratios W^+/W^- and **f** $W^\pm/Z$ compared to RADISH+NNLOJET and DYTURBO predictions with the NNPDF3.1 PDF set as described in the text. The shaded areas show the theoretical uncertainties derived from variations of the QCD scales and PDFs, the latter only for the DYTURBO predictions. The lower panels show the ratio of prediction to data with data markers centred at one and error bars giving the total measurement uncertainties
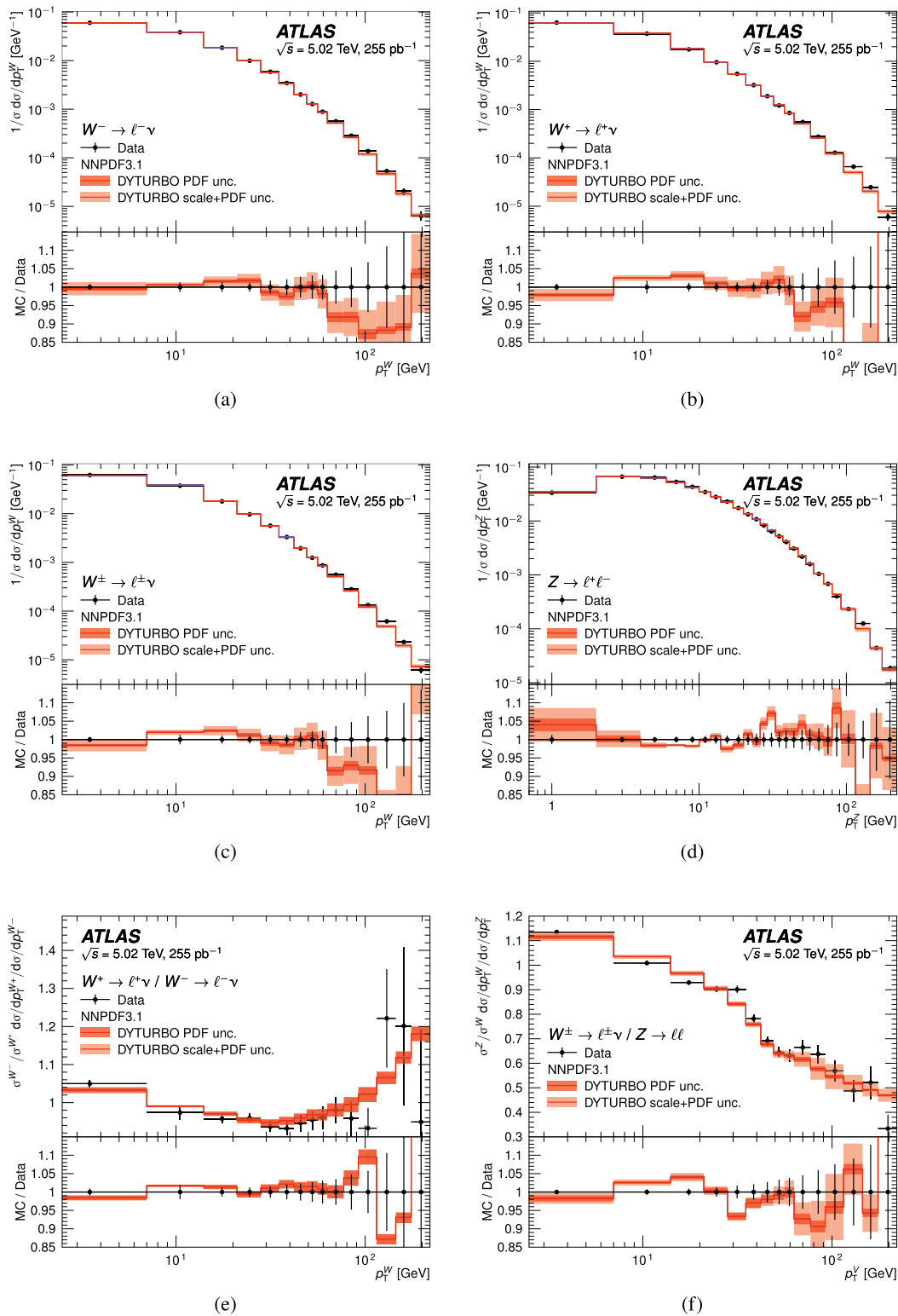
Fig. 29 Measurements of normalised differential distributions at $\sqrt{s} = 5.02$ TeV (black points) for **a** W^-, **b** W^+, **c** the sum $W^\pm$, **d** Z as well as **e** the ratios W^+/W^- and **f** $W^\pm/Z$ compared to DYTURBO predictions with different PDF sets (coloured lines) as described in the text. The lower panels show the ratio of prediction to data with data markers centred at one and error bars giving the total measurement uncertainties

(a)

(b)
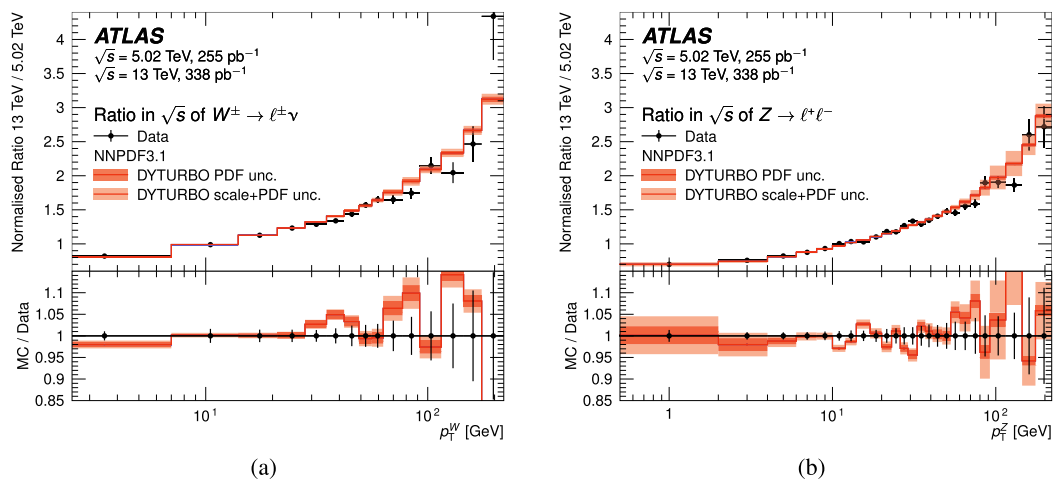
Fig. 30 Ratios of normalised differential distributions at $\sqrt{s} = 13$ TeV to $\sqrt{s} = 5.02$ TeV (black points) for **a**, **c** $W^{\pm}$ and **b**, **d** Z compared to **a**, **b** DYTURBO predictions with different PDF sets or **b**, **d** a variety of MC predictions (coloured lines) as described in the text. The lower panels show the ratio of prediction to data with data markers centred at one and error bars giving the size of the total measurement uncertainties

retically calculated acceptance factors A as $\sigma_{\text{tot}} = \sigma_{\text{fid}}/A$. For the Z/γ^* case, the total phase space retains the invariant mass range of $66 < m_{\ell\ell} < 116$ GeV. Table 9 summarises the A values as computed from the nominal POWHEG+PYTHIA 8 samples using the CT18 PDF set. The uncertainties are estimated from variations of QCD scales, PDFs and the difference to the alternative SHERPA samples. The corresponding total cross sections are given as well. The typical uncertainty on the acceptance correction is 2%. The equivalent computations for cross-section ratios are presented in Table 10.

Tables 11 and 12 display extrapolation factors E that may be used to translate the measured fiducial cross sections and ratios, respectively, to the fiducial phase space of the CMS analysis [99]:

- $W \rightarrow \ell\nu$: $p_{\text{T}}^{\ell} > 25$ GeV, $|\eta^{\ell}| < 2.4$, $p_{\text{T}}^{\nu} > 0$, and $m_{\text{T}} > 40$ GeV;
- $Z \rightarrow \ell\ell$: $p_{\text{T}}^{\ell} > 25$ GeV, $|\eta^{\ell}| < 2.4$, and 60 GeV $< m_{\ell\ell} < 120$ GeV.

As the phase spaces are similar, these factors are generally close to unity (within about 10%) and the theoretical uncertainties, computed in the same way as for A factors, are small.

(a)

(b)

(c)

(d)
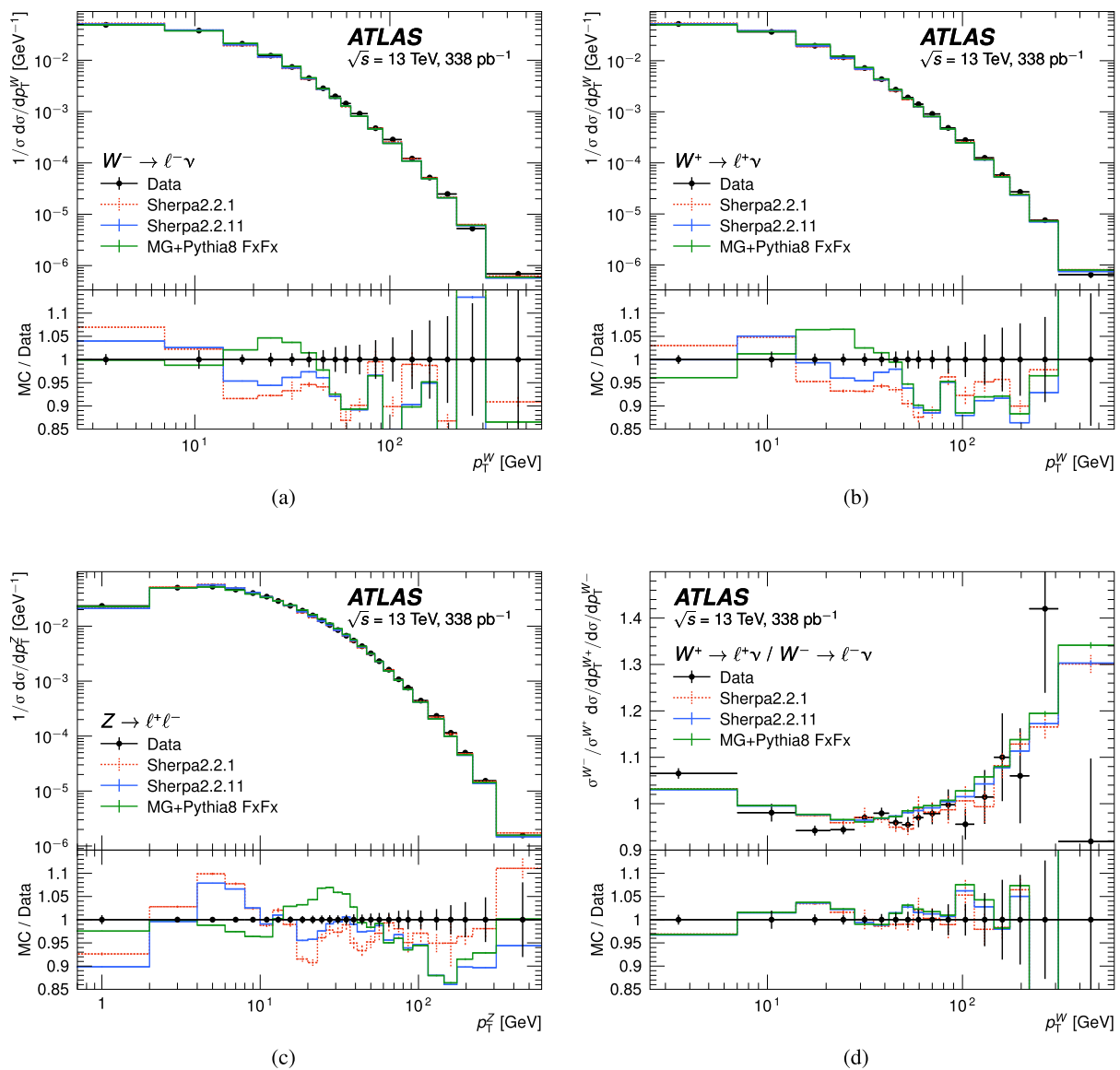
Fig. 31 Measurements of normalised differential distributions at $\sqrt{s} = 13$ TeV (black points) for **a** W^-, **b** W^+, **c** Z as well as **d** the W^+/W^- ratio compared to a variety MC predictions of multijet-merged NLO SHERPA and MADGRAPH_AMC@NLO FxFx+PYTHIA 8 samples (coloured lines) as described in the text. The lower panels show the ratio of prediction to data with data markers centred at one and error bars giving the size of the total measurement uncertainties

Table 9 Acceptance factors A to derive total production cross sections for W^-, W^+ and Z production at 5.02 and 13 TeV with total theory uncertainties. The measured fiducial cross sections and ratios are repeated from Table 3 and the resulting total cross sections are given

	$W^- \to \ell\nu$	$W^+ \to \ell\nu$	$W^\pm \to \ell\nu$	$Z \to \ell\ell$
$\sqrt{s} = 5.02$ TeV				
A	0.475 ± 0.004	0.506 ± 0.008	0.494 ± 0.006	0.492 ± 0.006
σ_{fid} [pb]	1384 ± 16	2228 ± 25	3612 ± 40	333.0 ± 4.1
σ_{tot} [pb]	2913 ± 41	4401 ± 85	7316 ± 124	677 ± 12
$\sqrt{s} = 13$ TeV				
A	0.399 ± 0.006	0.386 ± 0.009	0.391 ± 0.008	0.393 ± 0.011
σ_{fid} [pb]	3486 ± 38	4571 ± 49	8057 ± 88	780.3 ± 10.4
σ_{tot} [pb]	8740 ± 160	11850 ± 310	20580 ± 460	1986 ± 59

Table 10 Acceptance factors A to derive total production cross-section ratios at 5.02 and 13 TeV with total theory uncertainties. The measured fiducial ratios are repeated from Table 5 and the resulting total cross-section ratios are given

	W^+/W^-	$W^\pm/Z$
$\sqrt{s} = 5.02$ TeV		
$A^V/A^{V'}$	1.065 ± 0.012	1.003 ± 0.008
$\sigma_{\text{fid}}^V/\sigma_{\text{fid}}^{V'}$	1.609 ± 0.005	10.85 ± 0.08
$\sigma_{\text{tot}}^V/\sigma_{\text{tot}}^{V'}$	1.511 ± 0.017	10.82 ± 0.12
$\sqrt{s} = 13$ TeV		
$A^V/A^{V'}$	0.968 ± 0.011	0.996 ± 0.010
$\sigma_{\text{fid}}^V/\sigma_{\text{fid}}^{V'}$	1.308 ± 0.005	10.30 ± 0.11
$\sigma_{\text{tot}}^V/\sigma_{\text{tot}}^{V'}$	1.351 ± 0.017	10.34 ± 0.15

Table 11 Extrapolation factors E to translate the fiducial integrated cross sections to the phase space of the analysis performed by the CMS Collaboration [99]. The measured fiducial cross sections are repeated from Table 3 and the resulting extrapolated cross sections in the CMS fiducial volume are given

Experiment	$W^- \to \ell\nu$	$W^+ \to \ell\nu$	$Z \to \ell\ell$
$\sqrt{s} = 5.02$ TeV			
E	1.0951 ± 0.0053	1.1009 ± 0.0042	0.9637 ± 0.0008
ATLAS [pb]	1384 ± 16	2228 ± 25	333.0 ± 4.1
ATLAS@CMSfid [pb]	1516 ± 19	2453 ± 29	320.9 ± 4.0
$\sqrt{s} = 13$ TeV			
E	1.1156 ± 0.0031	1.1154 ± 0.0014	0.9621 ± 0.0011
ATLAS [pb]	3486 ± 38	4571 ± 49	780.3 ± 10.4
ATLAS@CMSfid [pb]	3889 ± 44	5099 ± 55	750.7 ± 10.0

Table 12 Extrapolation factors E to translate the fiducial integrated cross-section ratios to the phase space of the analysis performed by the CMS Collaboration [99]. The measured fiducial cross-section ratios are repeated from Table 5 and the resulting extrapolated cross-section ratios in the CMS fiducial volume are given

Experiment	W^+/W^-	$W^\pm/Z$
$\sqrt{s} = 5.02$ TeV		
$E^V/E^{V'}$	1.0052 ± 0.0013	1.1401 ± 0.0050
ATLAS	1.609 ± 0.005	10.85 ± 0.08
ATLAS@CMSfid	1.617 ± 0.005	12.37 ± 0.11
$\sqrt{s} = 13$ TeV		
$E^V/E^{V'}$	0.9998 ± 0.0033	1.1594 ± 0.0009
ATLAS	1.308 ± 0.005	10.30 ± 0.11
ATLAS@CMSfid	1.308 ± 0.007	11.94 ± 0.13

References

1. ATLAS Collaboration, Measurement of the W-boson mass and width with the ATLAS detector using proton–proton collisions at $\sqrt{s} = 7 \, TeV$. (2024). arXiv:2403.15085 [hep-ex]
2. CDF Collaboration, High-precision measurement of the W boson mass with the CDF II detector. Science **376**, 170 (2022). https://doi.org/10.1126/science.abk1781
3. D0 Collaboration, Measurement of the W boson mass with the D0 detector. Phys. Rev. D **89**, 012005 (2014). https://doi.org/10.1103/PhysRevD.89.012005. arXiv:1310.8628 [hep-ex]
4. LHCb Collaboration, Measurement of the W boson mass. JHEP **01**, 036 (2022). https://doi.org/10.1007/JHEP01(2022)036. arXiv:2109.01113 [hep-ex]
5. R. Boughezal et al., Z-boson production in association with a jet at next-to-next-to-leading order in perturbative QCD. Phys. Rev. Lett. **116**, 152001 (2016). https://doi.org/10.1103/PhysRevLett.116.152001. arXiv:1512.01291 [hep-ph]
6. A. Gehrmann-De Ridder, T. Gehrmann, E.W.N. Glover, A. Huss, T.A. Morgan, Precise QCD predictions for the production of a Z boson in association with a hadronic jet. Phys. Rev. Lett. **117**, 022001 (2016). https://doi.org/10.1103/PhysRevLett.117.022001. arXiv:1507.02850 [hep-ph]
7. R. Boughezal, X. Liu, F. Petriello, W-boson plus jet differential distributions at NNLO in QCD. Phys. Rev. D **94**, 113009 (2016). https://doi.org/10.1103/PhysRevD.94.113009. arXiv:1602.06965 [hep-ph]
8. G. Bozzi, S. Catani, D. de Florian, M. Grazzini, Transverse-momentum resummation and the spectrum of the Higgs boson at

the LHC. Nucl. Phys. B **737**, 73 (2006). https://doi.org/10.1016/j.nuclphysb.2005.12.022. arXiv:hep-ph/0508068

9. W. Bizoń et al., The transverse momentum spectrum of weak gauge bosons at N³LL+NNLO. Eur. Phys. J. C **79**, 868 (2019). https://doi.org/10.1140/epjc/s10052-019-7324-0. arXiv:1905.05171 [hep-ph]

10. T. Neumann, J. Campbell, Fiducial Drell–Yan production at the LHC improved by transverse-momentum resummation at $N^4LL_p + N^3LO$. Phys. Rev. D **107**, L011506 (2023). https://doi.org/10.1103/PhysRevD.107.L011506. arXiv:2207.07056 [hep-ph]

11. S. Camarda, L. Cieri, G. Ferrera, Drell–Yan lepton-pair production: qT resummation at N4LL accuracy. Phys. Lett. B **845**, 138125 (2023). https://doi.org/10.1016/j.physletb.2023.138125. arXiv:2303.12781 [hep-ph]

12. T. Sjöstrand, S. Mrenna, P. Skands, A brief introduction to PYTHIA 8.1. Comput. Phys. Commun. **178**, 852 (2008). https://doi.org/10.1016/j.cpc.2008.01.036. arXiv:0710.3820 [hep-ph]

13. J. Bellm et al., Herwig 7.0/Herwig++ 3.0 release note. Eur. Phys. J. C **76**, 196 (2016). https://doi.org/10.1140/epjc/s10052-016-4018-8. arXiv:1512.01178 [hep-ph]

14. E. Bothmann et al., Event generation with Sherpa 2.2. SciPost Phys. **7**, 034 (2019). https://doi.org/10.21468/SciPostPhys.7.3.034. arXiv:1905.09127 [hep-ph]

15. ATLAS Collaboration, Measurement of the $Z/\gamma*$ boson transverse momentum distribution in pp collisions at $\sqrt{s} = 7\,TeV$ with the ATLAS detector. JHEP **09**, 145 (2014). https://doi.org/10.1007/JHEP09(2014)145. arXiv:1406.3660 [hep-ex]

16. ATLAS Collaboration, Measurement of the transverse momentum and ϕ_η^* distributions of Drell–Yan lepton pairs in proton–proton collisions at $\sqrt{s} = 8\,TeV$ with the ATLAS detector. Eur. Phys. J. C **76**, 291 (2016). https://doi.org/10.1140/epjc/s10052-016-4070-4. arXiv:1512.02192 [hep-ex]

17. ATLAS Collaboration, Measurement of the transverse momentum distribution of Drell–Yan lepton pairs in proton–proton collisions at $\sqrt{s} = 13\,TeV$ with the ATLAS detector. Eur. Phys. J. C **80**, 616 (2020). https://doi.org/10.1140/epjc/s10052-020-8001-z. arXiv:1912.02844 [hep-ex]

18. CMS Collaboration, Measurement of the rapidity and transverse momentum distributions of Z bosons in pp collisions at $\sqrt{(s)} = 7\,TeV$. Phys. Rev. D **85**, 032002 (2012). https://doi.org/10.1103/PhysRevD.85.032002. arXiv:1110.4973 [hep-ex]

19. CMS Collaboration, Measurement of the Z boson differential cross section in transverse momentum and rapidity in proton-proton collisions at 8 Tev. Phys. Lett. B **749**, 187 (2015). https://doi.org/10.1016/j.physletb.2015.07.065. arXiv:1504.03511 [hep-ex]

20. CMS Collaboration, Measurement of the mass dependence of the transverse momentum of lepton pairs in Drell–Yan production in proton-proton collisions at $\sqrt{s} = 13\,TeV$. Eur. Phys. J. C **83**, 628 (2023). https://doi.org/10.1140/epjc/s10052-023-11631-7. arXiv:2205.04897 [hep-ex]

21. LHCb Collaboration, Measurement of the forward Z boson production cross-section in pp collisions at $\sqrt{s} = 7$ TeV. JHEP **08**, 039 (2015). https://doi.org/10.1007/JHEP08(2015)039. arXiv:1505.07024 [hep-ex]

22. LHCb Collaboration, Measurement of forward W and Z boson production in pp collisions at $\sqrt{s} = 8$ TeV. JHEP **01**, 155 (2016). https://doi.org/10.1007/JHEP01(2016)155. arXiv:1511.08039 [hep-ex]

23. LHCb Collaboration, Precision measurement of forward Z boson production in proton–proton collisions at $\sqrt{s} = 13\,TeV$. JHEP **07**, 026 (2022). https://doi.org/10.1007/JHEP07(2022)026. arXiv:2112.07458 [hep-ex]

24. ATLAS Collaboration, Measurement of the transverse momentum distribution of W bosons in pp collisions at $\sqrt{s} = 7\,TeV$ with the ATLAS detector. Phys. Rev. D **85**, 012005 (2012). https://doi.org/10.1103/PhysRevD.85.012005. arXiv:1108.6308 [hep-ex]

25. CMS Collaboration, Measurement of the transverse momentum spectra of weak vector bosons produced in proton–proton collisions at $\sqrt{s} = 8\,TeV$. JHEP **02**, 096 (2017). https://doi.org/10.1007/JHEP02(2017)096. arXiv:1606.05864 [hep-ex]

26. ATLAS Collaboration, The ATLAS Experiment at the CERN Large Hadron Collider. JINST **3**, S08003 (2008). https://doi.org/10.1088/1748-0221/3/08/S08003

27. ATLAS Collaboration, ATLAS insertable B-layer: technical design report. ATLAS-TDR-19; CERN-LHCC-2010-013, 2010. https://cds.cern.ch/record/1291633. Addendum: ATLAS-TDR-19-ADD-1; CERN-LHCC-2012-009, 2012. https://cds.cern.ch/record/1451888

28. B. Abbott et al., Production and integration of the ATLAS insertable B-layer. JINST **13**, T05008 (2018). https://doi.org/10.1088/1748-0221/13/05/T05008. arXiv:1803.00844 [physics.ins-det]

29. G. Avoni et al., The new LUCID-2 detector for luminosity measurement and monitoring in ATLAS. JINST **13**, P07017 (2018). https://doi.org/10.1088/1748-0221/13/07/P07017

30. ATLAS Collaboration, Performance of the ATLAS trigger system in 2015. Eur. Phys. J. C **77**, 317 (2017). https://doi.org/10.1140/epjc/s10052-017-4852-3. arXiv:1611.09661 [hep-ex]

31. ATLAS Collaboration, The ATLAS collaboration software and firmware. ATL-SOFT-PUB-2021-001, 2021. https://cds.cern.ch/record/2767187

32. ATLAS Collaboration, Luminosity determination in pp collisions at $\sqrt{s} = 13\,TeV$ using the ATLAS detector at the LHC. Eur. Phys. J. C **83**, 982 (2023). https://doi.org/10.1140/epjc/s10052-023-11747-w. arXiv:2212.09379 [hep-ex]

33. ATLAS Collaboration, Performance of electron and photon triggers in ATLAS during LHC run 2. Eur. Phys. J. C **80**, 47 (2020). https://doi.org/10.1140/epjc/s10052-019-7500-2. arXiv:1909.00761 [hep-ex]

34. ATLAS Collaboration, Performance of the ATLAS muon triggers in run 2. JINST **15**, P09015 (2020). https://doi.org/10.1088/1748-0221/15/09/p09015. arXiv:2004.13447 [physics.ins-det]

35. ATLAS Collaboration, The ATLAS simulation infrastructure. Eur. Phys. J. C **70**, 823 (2010). https://doi.org/10.1140/epjc/s10052-010-1429-9. arXiv:1005.4568 [physics.ins-det]

36. S. Agostinelli et al., GEANT4—a simulation toolkit. Nucl. Instrum. Methods A **506**, 250 (2003). https://doi.org/10.1016/S0168-9002(03)01368-8

37. NNPDF Collaboration, R.D. Ball et al., Parton distributions with LHC data. Nucl. Phys. B **867**, 244 (2013). https://doi.org/10.1016/j.nuclphysb.2012.10.003. arXiv:1207.1303 [hep-ph]

38. ATLAS Collaboration, The Pythia 8 A3 tune description of ATLAS minimum bias and inelastic measurements incorporating the Donnachie–Landshoff diffractive model. ATL-PHYS-PUB-2016-017, 2016. https://cds.cern.ch/record/2206965

39. P. Nason, A new method for combining NLO QCD with shower Monte Carlo algorithms. JHEP **11**, 040 (2004). https://doi.org/10.1088/1126-6708/2004/11/040. arXiv:hep-ph/0409146

40. S. Frixione, P. Nason, C. Oleari, Matching NLO QCD computations with parton shower simulations: the POWHEG method. JHEP **11**, 070 (2007). https://doi.org/10.1088/1126-6708/2007/11/070. arXiv:0709.2092 [hep-ph]

41. S. Alioli, P. Nason, C. Oleari, E. Re, NLO vector-boson production matched with shower in POWHEG. JHEP **07**, 060 (2008). https://doi.org/10.1088/1126-6708/2008/07/060. arXiv:0805.4802 [hep-ph]

42. S. Alioli, P. Nason, C. Oleari, E. Re, A general framework for implementing NLO calculations in shower Monte Carlo programs: the POWHEG BOX. JHEP **06**, 043 (2010). https://doi.org/10.1007/JHEP06(2010)043. arXiv:1002.2581 [hep-ph]

43. H.-L. Lai et al., New parton distributions for collider physics. Phys. Rev. D **82**, 074024 (2010). https://doi.org/10.1103/PhysRevD.82.074024. arXiv:1007.2241 [hep-ph]

44. P. Golonka, Z. Was, PHOTOS Monte Carlo: a precision tool for QED corrections in Z and W decays. Eur. Phys. J. C **45**, 97 (2006). https://doi.org/10.1140/epjc/s2005-02396-4. arXiv:hep-ph/0506026

45. NNPDF Collaboration, R.D. Ball et al., Parton distributions for the LHC run II. JHEP **04**, 040 (2015). https://doi.org/10.1007/JHEP04(2015)040. arXiv:1410.8849 [hep-ph]

46. T. Gleisberg, S. Höche, Comix, a new matrix element generator. JHEP **12**, 039 (2008). https://doi.org/10.1088/1126-6708/2008/12/039. arXiv:0808.3674 [hep-ph]

47. F. Buccioni et al., OpenLoops 2. Eur. Phys. J. C **79**, 866 (2019). https://doi.org/10.1140/epjc/s10052-019-7306-2. arXiv:1907.13071 [hep-ph]

48. F. Cascioli, P. Maierhöfer, S. Pozzorini, Scattering amplitudes with Open Loops. Phys. Rev. Lett. **108**, 111601 (2012). https://doi.org/10.1103/PhysRevLett.108.111601. arXiv:1111.5206 [hep-ph]

49. A. Denner, S. Dittmaier, L. Hofer, Collier: a Fortran-based complex one-loop library in extended regularizations. Comput. Phys. Commun. **212**, 220 (2017). https://doi.org/10.1016/j.cpc.2016.10.013. arXiv:1604.06792 [hep-ph]

50. S. Schumann, F. Krauss, A parton shower algorithm based on Catani–Seymour dipole factorisation. JHEP **03**, 038 (2008). https://doi.org/10.1088/1126-6708/2008/03/038. arXiv:0709.1027 [hep-ph]

51. S. Höche, F. Krauss, M. Schönherr, F. Siegert, A critical appraisal of NLO+PS matching methods. JHEP **09**, 049 (2012). https://doi.org/10.1007/JHEP09(2012)049. arXiv:1111.1220 [hep-ph]

52. S. Höche, F. Krauss, M. Schönherr, F. Siegert, QCD matrix elements + parton showers. The NLO case. JHEP **04**, 027 (2013). https://doi.org/10.1007/JHEP04(2013)027. arXiv:1207.5030 [hep-ph]

53. S. Catani, F. Krauss, B.R. Webber, R. Kuhn, QCD matrix elements + parton showers. JHEP **11**, 063 (2001). https://doi.org/10.1088/1126-6708/2001/11/063. arXiv:hep-ph/0109231

54. S. Höche, F. Krauss, S. Schumann, F. Siegert, QCD matrix elements and truncated showers. JHEP **05**, 053 (2009). https://doi.org/10.1088/1126-6708/2009/05/053. arXiv:0903.1219 [hep-ph]

55. S. Camarda, L. Cieri, G. Ferrera, Drell–Yan lepton-pair production: q_T resummation at N^3LL accuracy and fiducial cross sections at N^3LO. Phys. Rev. D **104**, L111503 (2021). https://doi.org/10.1103/PhysRevD.104.L111503. arXiv:2103.04974 [hep-ph]

56. S. Catani, M. Grazzini, Next-to-next-to-leading-order subtraction formalism in hadron collisions and its application to Higgs-boson production at the Large Hadron Collider. Phys. Rev. Lett. **98**, 222002 (2007). https://doi.org/10.1103/PhysRevLett.98.222002. arXiv:hep-ph/0703012

57. S. Catani, L. Cieri, G. Ferrera, D. de Florian, M. Grazzini, Vector boson production at hadron colliders: a fully exclusive QCD calculation at next-to-next-to-leading order. Phys. Rev. Lett. **103**, 082001 (2009). https://doi.org/10.1103/PhysRevLett.103.082001. arXiv:0903.2120 [hep-ph]

58. L.A. Harland-Lang, A.D. Martin, P. Motylinski, R.S. Thorne, Parton distributions in the LHC era: MMHT 2014 PDFs. Eur. Phys. J. C **75**, 204 (2015). https://doi.org/10.1140/epjc/s10052-015-3397-6. arXiv:1412.3989 [hep-ph]

59. ATLAS Collaboration, Study of top-quark pair modelling and uncertainties using ATLAS measurements at $\sqrt{s} = 13\,TeV$. ATL-PHYS-PUB-2020-023, 2020. https://cds.cern.ch/record/2730443

60. M. Beneke, P. Falgari, S. Klein, C. Schwinn, Hadronic top-quark pair production with NNLL threshold resummation. Nucl. Phys. B **855**, 695 (2012). https://doi.org/10.1016/j.nuclphysb.2011.10.021. arXiv:1109.1536 [hep-ph]

61. M. Cacciari, M. Czakon, M. Mangano, A. Mitov, P. Nason, Top-pair production at hadron colliders with next-to-next-to-leading logarithmic soft-gluon resummation. Phys. Lett. B **710**, 612 (2012). https://doi.org/10.1016/j.physletb.2012.03.013. arXiv:1111.5869 [hep-ph]

62. P. Bärnreuther, M. Czakon, A. Mitov, Percent-level-precision physics at the tevatron: next-to-next-to-leading order QCD corrections to $q\bar{q} \to t\bar{t} + X$. Phys. Rev. Lett. **109**, 132001 (2012). https://doi.org/10.1103/PhysRevLett.109.132001. arXiv:1204.5201 [hep-ph]

63. M. Czakon, A. Mitov, NNLO corrections to top-pair production at hadron colliders: the all-fermionic scattering channels. JHEP **12**, 054 (2012). https://doi.org/10.1007/JHEP12(2012)054. arXiv:1207.0236 [hep-ph]

64. M. Czakon, A. Mitov, NNLO corrections to top pair production at hadron colliders: the quark-gluon reaction. JHEP **01**, 080 (2013). https://doi.org/10.1007/JHEP01(2013)080. arXiv:1210.6832 [hep-ph]

65. M. Czakon, P. Fiedler, A. Mitov, Total top-quark pair-production cross section at hadron colliders through $\mathcal{O}(\alpha_S^4)$. Phys. Rev. Lett. **110**, 252004 (2013). https://doi.org/10.1103/PhysRevLett.110.252004. arXiv:1303.6254 [hep-ph]

66. M. Czakon, A. Mitov, Top++: a program for the calculation of the top-pair cross-section at hadron colliders. Comput. Phys. Commun. **185**, 2930 (2014). https://doi.org/10.1016/j.cpc.2014.06.021. arXiv:1112.5675 [hep-ph]

67. ATLAS Collaboration, Multi-boson simulation for 13 TeV ATLAS analyses. ATL-PHYS-PUB-2017-005, 2017. https://cds.cern.ch/record/2261933

68. ATLAS Collaboration, Electron and photon performance measurements with the ATLAS detector using the 2015–2017 LHC proton–proton collision data. JINST **14**, P12006 (2019). https://doi.org/10.1088/1748-0221/14/12/P12006. arXiv:1908.00005 [hep-ex]

69. ATLAS Collaboration, Studies of the muon momentum calibration and performance of the ATLAS detector with pp collisions at $\sqrt{s} = 13\,TeV$. Eur. Phys. J. C **83**, 686 (2023). https://doi.org/10.1140/epjc/s10052-023-11584-x. arXiv:2212.07338 [hep-ex]

70. ATLAS Collaboration, Measurement of the W-boson mass in pp collisions at $\sqrt{s} = 7\,TeV$ with the ATLAS detector. Eur. Phys. J. C **78**, 110 (2018). https://doi.org/10.1140/epjc/s10052-017-5475-4. arXiv:1701.07240 [hep-ex]. Erratum: Eur. Phys. J. C 78 (2018) 898. https://doi.org/10.1140/epjc/s10052-018-6354-3

71. ATLAS Collaboration, Alignment of the ATLAS inner detector in run 2. Eur. Phys. J. C **80**, 1194 (2020). https://doi.org/10.1140/epjc/s10052-020-08700-6. arXiv:2007.07624 [hep-ex]

72. ATLAS Collaboration, Vertex reconstruction performance of the ATLAS detector at $\sqrt{s} = 13\,TeV$. ATL-PHYS-PUB-2015-026, 2015. https://cds.cern.ch/record/2037717

73. ATLAS Collaboration, Topological cell clustering in the ATLAS calorimeters and its performance in LHC run 1. Eur. Phys. J. C **77**, 490 (2017). https://doi.org/10.1140/epjc/s10052-017-5004-5. arXiv:1603.02934 [hep-ex]

74. ATLAS Collaboration, Jet reconstruction and performance using particle flow with the ATLAS detector. Eur. Phys. J. C **77**, 466 (2017). https://doi.org/10.1140/epjc/s10052-017-5031-2. arXiv:1703.10485 [hep-ex]

75. ATLAS Collaboration, Jet energy scale and resolution measured in proton–proton collisions at $\sqrt{s} = 13\,TeV$ with the ATLAS detector. Eur. Phys. J. C **81**, 689 (2021). https://doi.org/10.1140/epjc/s10052-021-09402-3. arXiv:2007.02645 [hep-ex]

76. L. Devroye, *Non-uniform Random Variate Generation* (Springer, New York, 1986). https://doi.org/10.1007/978-1-4613-8643-8

77. ATLAS Collaboration, Precision measurement and interpretation of inclusive W^+, W^- and Z/γ^* production cross sections with the ATLAS detector. Eur. Phys. J. C **77**, 367 (2017). https://doi.org/10.1140/epjc/s10052-017-4911-9. arXiv:1612.03016 [hep-ex]

78. G. D'Agostini, A multidimensional unfolding method based on Bayes' theorem. Nucl. Instrum. Methods A **362**, 487 (1995). https://doi.org/10.1016/0168-9002(95)00274-X

79. G. D'Agostini, Improved iterative Bayesian unfolding. (2010). arXiv:1010.0632 [physics.data-an]

80. ATLAS Collaboration, Evaluating statistical uncertainties and correlations using the bootstrap method. ATL-PHYS-PUB-2021-011, 2021. https://cds.cern.ch/record/2759945

81. L. Lyons, D. Gibaut, P. Clifford, How to combine correlated estimates of a single physical quantity. Nucl. Instrum. Methods A **270**, 110 (1988). https://doi.org/10.1016/0168-9002(88)90018-6

82. A. Valassi, Combining correlated measurements of several different physical quantities. Nucl. Instrum. Methods A **500**, 391 (2003). https://doi.org/10.1016/S0168-9002(03)00329-2

83. H. Dembinski, M. Schmelling, R. Waldi, Application of the iterated weighted least-squares fit to counting experiments. Nucl. Instrum. Methods A **940**, 135 (2019). https://doi.org/10.1016/j.nima.2019.05.086. arXiv:1807.07911 [physics.data-an]

84. ATLAS Collaboration, Measurements of W and Z boson production in pp collisions at $\sqrt{s} = 5.02\,TeV$ with the ATLAS detector. Eur. Phys. J. C **79**, 128 (2019). https://doi.org/10.1140/epjc/s10052-019-6622-x. arXiv:1810.08424 [hep-ex]. Erratum: Eur. Phys. J. C 79 (2019) 374. https://doi.org/10.1140/epjc/s10052-019-6870-9

85. ATLAS Collaboration, Measurement of $W^\pm$ and Z-boson production cross sections in pp collisions at $\sqrt{s} = 13\,TeV$ with the ATLAS detector. Phys. Lett. B **759**, 601 (2016). https://doi.org/10.1016/j.physletb.2016.06.023. arXiv:1603.09222 [hep-ex]

86. ATLAS Collaboration, Measurements of top-quark pair to Z-boson cross-section ratios at $\sqrt{s} = 13, 8, 7\,TeV$ with the ATLAS detector. JHEP **02**, 117 (2017). https://doi.org/10.1007/JHEP02(2017)117. arXiv:1612.03636 [hep-ex]

87. T.-J. Hou et al., New CTEQ global analysis of quantum chromodynamics with high-precision data from the LHC. Phys. Rev. D **103**, 014013 (2021). https://doi.org/10.1103/PhysRevD.103.014013. arXiv:1912.10053 [hep-ph]

88. S. Bailey, T. Cridge, L.A. Harland-Lang, A.D. Martin, R.S. Thorne, Parton distributions from LHC, HERA, Tevatron and fixed target data: MSHT20 PDFs. Eur. Phys. J. C **81**, 341 (2021). https://doi.org/10.1140/epjc/s10052-021-09057-0. arXiv:2012.04684 [hep-ph]

89. NNPDF Collaboration, R.D. Ball et al., Parton distributions from high-precision collider data. Eur. Phys. J. C **77**, 663 (2017). https://doi.org/10.1140/epjc/s10052-017-5199-5. arXiv:1706.00428 [hep-ph]

90. J. Bellm et al., Herwig 7.1 release note. (2017). arXiv:1705.06919 [hep-ph]

91. ATLAS Collaboration, Modelling and computational improvements to the simulation of single vector-boson plus jet processes for the ATLAS experiment. JHEP **08**, 089 (2022). https://doi.org/10.1007/JHEP08(2022)089. arXiv:2112.09588 [hep-ex]

92. J. Alwall et al., The automated computation of tree-level and next-to-leading order differential cross sections, and their matching to parton shower simulations. JHEP **07**, 079 (2014). https://doi.org/10.1007/JHEP07(2014)079. arXiv:1405.0301 [hep-ph]

93. R. Frederix, S. Frixione, Merging meets matching in MC@NLO. JHEP **12**, 061 (2012). https://doi.org/10.1007/JHEP12(2012)061. arXiv:1209.6215 [hep-ph]

94. C. Bierlich et al., Robust independent validation of experiment and theory: Rivet version 3. SciPost Phys. **8**, 026 (2020). https://doi.org/10.21468/SciPostPhys.8.2.026. arXiv:1912.05451 [hep-ph]

95. ATLAS Collaboration, ATLAS computing acknowledgements. ATL-SOFT-PUB-2023-001, 2023. https://cds.cern.ch/record/2869272

96. W. Bizoń et al., Fiducial distributions in Higgs and Drell–Yan production at N^{3}LL+NNLO. JHEP **12**, 132 (2018). https://doi.org/10.1007/JHEP12(2018)132. arXiv:1805.05916 [hep-ph]

97. A. Gehrmann-De Ridder, T. Gehrmann, E.W.N. Glover, A. Huss, T.A. Morgan, NNLO QCD corrections for Drell–Yan p_T^Z and ϕ_η^* observables at the LHC. JHEP **11**, 094 (2016). https://doi.org/10.1007/JHEP11(2016)094. arXiv:1610.01843 [hep-ph]. Erratum: JHEP 10 (2018) 126. https://doi.org/10.1007/JHEP10(2018)126

98. W. Bizoń, P.F. Monni, E. Re, L. Rottoli, P. Torrielli, Momentum-space resummation for transverse observables and the Higgs $p_\perp$ at N^{3}LL+NNLO. JHEP **02**, 108 (2018). https://doi.org/10.1007/JHEP02(2018)108. arXiv:1705.09127 [hep-ph]

99. CMS Collaboration, Measurement of the inclusive cross sections for W and Z boson production in proton-proton collisions at $\sqrt{s} = 5.02$ and 13 TeV. (2023). https://cds.cern.ch/record/2868090

ATLAS Collaboration[*]

G. Aad[102], B. Abbott[120], K. Abeling[55], N. J. Abicht[49], S. H. Abidi[29], A. Aboulhorma[35e], H. Abramowicz[151], H. Abreu[150], Y. Abulaiti[117], B. S. Acharya[69a,69b,m], C. Adam Bourdarios[4], L. Adamczyk[86a], L. Adamek[155], S. V. Addepalli[26], M. J. Addison[101], J. Adelman[115], A. Adiguzel[21c], T. Adye[134], A. A. Affolder[136], Y. Afik[36], M. N. Agaras[13], J. Agarwala[73a,73b], A. Aggarwal[100], C. Agheorghiesei[27c], A. Ahmad[36], F. Ahmadov[38,z], W. S. Ahmed[104], S. Ahuja[95], X. Ai[62a], G. Aielli[76a,76b], A. Aikot[163], M. Ait Tamlihat[35e], B. Aitbenchikh[35a], I. Aizenberg[169], M. Akbiyik[100], T. P. A. Åkesson[98], A. V. Akimov[37], D. Akiyama[168], N. N. Akolkar[24], K. Al Khoury[41], G. L. Alberghi[23b], J. Albert[165], P. Albicocco[53], G. L. Albouy[60], S. Alderweireldt[52], M. Aleksa[36], I. N. Aleksandrov[38], C. Alexa[27b], T. Alexopoulos[10], F. Alfonsi[23b], M. Algren[56], M. Alhroob[120], B. Ali[132], H. M. J. Ali[91], S. Ali[148], S. W. Alibocus[92], M. Aliev[145], G. Alimonti[71a], W. Alkakhi[55], C. Allaire[66], B. M. M. Allbrooke[146], J. F. Allen[52], C. A. Allendes Flores[137f], P. P. Allport[20], A. Aloisio[72a,72b], F. Alonso[90], C. Alpigiani[138], M. Alvarez Estevez[99], A. Alvarez Fernandez[100], M. Alves Cardoso[56], M. G. Alviggi[72a,72b], M. Aly[101], Y. Amaral Coutinho[83b], A. Ambler[104], C. Amelung[36], M. Amerl[101], C. G. Ames[109], D. Amidei[106], S. P. Amor Dos Santos[130a], K. R. Amos[163], V. Ananiev[125], C. Anastopoulos[139], T. Andeen[11], J. K. Anders[36], S. Y. Andrean[47a,47b], A. Andreazza[71a,71b], S. Angelidakis[9], A. Angerami[41,ac], A. V. Anisenkov[37], A. Annovi[74a], C. Antel[56], M. T. Anthony[139], E. Antipov[145], M. Antonelli[53], F. Anulli[75a], M. Aoki[84], T. Aoki[153], J. A. Aparisi Pozo[163], M. A. Aparo[146], L. Aperio Bella[48], C. Appelt[18], A. Apyan[26], N. Aranzabal[36], C. Arcangeletti[53], A. T. H. Arce[51], E. Arena[92], J.-F. Arguin[108], S. Argyropoulos[54], J.-H. Arling[48], O. Arnaez[4], H. Arnold[114], G. Artoni[75a,75b], H. Asada[111], K. Asai[118], S. Asai[153], N. A. Asbah[61], J. Assahsah[35d], K. Assamagan[29], R. Astalos[28a], S. Atashi[160], R. J. Atkin[33a], M. Atkinson[162], H. Atmani[35f], P. A. Atmasiddha[106], K. Augsten[132], S. Auricchio[72a,72b], A. D. Auriol[20], V. A. Austrup[101], G. Avolio[36], K. Axiotis[56], G. Azuelos[108,ah], D. Babal[28b], H. Bachacou[135], K. Bachas[152,p], A. Bachiu[34], F. Backman[47a,47b], A. Badea[61], P. Bagnaia[75a,75b], M. Bahmani[18], A. J. Bailey[163], V. R. Bailey[162], J. T. Baines[134], L. Baines[94], C. Bakalis[10], O. K. Baker[172], E. Bakos[15], D. Bakshi Gupta[8], V. Balakrishnan[120], R. Balasubramanian[114], E. M. Baldin[37], P. Balek[86a], E. Ballabene[23a,23b], F. Balli[135], L. M. Baltes[63a], W. K. Balunas[32], J. Balz[100], E. Banas[87], M. Bandieramonte[129], A. Bandyopadhyay[24], S. Bansal[24], L. Barak[151], M. Barakat[48], E. L. Barberio[105], D. Barberis[57a,57b], M. Barbero[102], M. Z. Barel[114], K. N. Barends[33a], T. Barillari[110], M.-S. Barisits[36], T. Barklow[143], P. Baron[122], D. A. Baron Moreno[101], A. Baroncelli[62a], G. Barone[29], A. J. Barr[126], J. D. Barr[96], L. Barranco Navarro[47a,47b], F. Barreiro[99], J. Barreiro Guimarães da Costa[14a], U. Barron[151], M. G. Barros Teixeira[130a], S. Barsov[37], F. Bartels[63a], R. Bartoldus[143], A. E. Barton[91], P. Bartos[28a], A. Basan[100], M. Baselga[49], A. Bassalat[66,b], M. J. Basso[156a], C. R. Basson[101], R. L. Bates[59], S. Batlamous[35e], J. R. Batley[32], B. Batool[141], M. Battaglia[136], D. Battulga[18], M. Bauce[75a,75b], M. Bauer[36], P. Bauer[24], L. T. Bazzano Hurrell[30], J. B. Beacham[51], T. Beau[127], P. H. Beauchemin[158], F. Becherer[54], P. Bechtle[24], H. P. Beck[19,o], K. Becker[167], A. J. Beddall[82], V. A. Bednyakov[38], C. P. Bee[145], L. J. Beemster[15], T. A. Beermann[36], M. Begalli[83d], M. Begel[29], A. Behera[145], J. K. Behr[48], J. F. Beirer[55], F. Beisiegel[24], M. Belfkir[159], G. Bella[151], L. Bellagamba[23b], A. Bellerive[34], P. Bellos[20], K. Beloborodov[37], D. Benchekroun[35a], F. Bendebba[35a], Y. Benhammou[151], M. Benoit[29], J. R. Bensinger[26], S. Bentvelsen[114], L. Beresford[48], M. Beretta[53], E. Bergeaas Kuutmann[161], N. Berger[4], B. Bergmann[132], J. Beringer[17a], G. Bernardi[5], C. Bernius[143], F. U. Bernlochner[24], F. Bernon[36,102], T. Berry[95], P. Berta[133], A. Berthold[50], I. A. Bertram[91], S. Bethke[110], A. Betti[75a,75b], A. J. Bevan[94], M. Bhamjee[33c], S. Bhatta[145], D. S. Bhattacharya[166], P. Bhattarai[143], V. S. Bhopatkar[121], R. Bi[29,aj], R. M. Bianchi[129], G. Bianco[23a,23b], O. Biebel[109], R. Bielski[123], M. Biglietti[77a], M. Bindi[55], A. Bingul[21b], C. Bini[75a,75b], A. Biondini[92], C. J. Birch-sykes[101], G. A. Bird[20,134], M. Birman[169], M. Biros[133], S. Biryukov[146], T. Bisanz[49], E. Bisceglie[43a,43b], J. P. Biswal[134], D. Biswas[141], A. Bitadze[101], K. Bjørke[125], I. Bloch[48], C. Blocker[26], A. Blue[59], U. Blumenschein[94], J. Blumenthal[100], G. J. Bobbink[114], V. S. Bobrovnikov[37], M. Boehler[54], B. Boehm[166], D. Bogavac[36], A. G. Bogdanchikov[37], C. Bohm[47a], V. Boisvert[95], P. Bokan[48], T. Bold[86a], M. Bomben[5], M. Bona[94], M. Boonekamp[135], C. D. Booth[95], A. G. Borbély[59], I. S. Bordulev[37], H. M. Borecka-Bielska[108], G. Borissov[91], D. Bortoletto[126], D. Boscherini[23b], M. Bosman[13], J. D. Bossio Sola[36], K. Bouaouda[35a], N. Bouchhar[163], J. Boudreau[129], E. V. Bouhova-Thacker[91], D. Boumediene[40], R. Bouquet[5], A. Boveia[119], J. Boyd[36], D. Boye[29], I. R. Boyko[38], J. Bracinik[20], N. Brahimi[62d], G. Brandt[171], O. Brandt[32], F. Braren[48], B. Brau[103], J. E. Brau[123], R. Brener[169],

L. Brenner[114], R. Brenner[161], S. Bressler[169], D. Britton[59], D. Britzger[110], I. Brock[24], R. Brock[107], G. Brooijmans[41], W. K. Brooks[137f], E. Brost[29], L. M. Brown[165], L. E. Bruce[61], T. L. Bruckler[126], P. A. Bruckman de Renstrom[87], B. Brüers[48], A. Bruni[23b], G. Bruni[23b], M. Bruschi[23b], N. Bruscino[75a,75b], T. Buanes[16], Q. Buat[138], D. Buchin[110], A. G. Buckley[59], O. Bulekov[37], B. A. Bullard[143], S. Burdin[92], C. D. Burgard[49], A. M. Burger[40], B. Burghgrave[8], O. Burlayenko[54], J. T. P. Burr[32], C. D. Burton[11], J. C. Burzynski[142], E. L. Busch[41], V. Büscher[100], P. J. Bussey[59], J. M. Butler[25], C. M. Buttar[59], J. M. Butterworth[96], W. Buttinger[134], C. J. Buxo Vazquez[107], A. R. Buzykaev[37], S. Cabrera Urbán[163], L. Cadamuro[66], D. Caforio[58], H. Cai[129], Y. Cai[14a,14e], V. M. M. Cairo[36], O. Cakir[3a], N. Calace[36], P. Calafiura[17a], G. Calderini[127], P. Calfayan[68], G. Callea[59], L. P. Caloba[83b], D. Calvet[40], S. Calvet[40], T. P. Calvet[102], M. Calvetti[74a,74b], R. Camacho Toro[127], S. Camarda[36], D. Camarero Munoz[26], P. Camarri[76a,76b], M. T. Camerlingo[72a,72b], D. Cameron[36], C. Camincher[165], M. Campanelli[96], A. Camplani[42], V. Canale[72a,72b], A. Canesse[104], J. Cantero[163], Y. Cao[162], F. Capocasa[26], M. Capua[43a,43b], A. Carbone[71a,71b], R. Cardarelli[76a], J. C. J. Cardenas[8], F. Cardillo[163], T. Carli[36], G. Carlino[72a], J. I. Carlotto[13], B. T. Carlson[129,q], E. M. Carlson[156a,165], L. Carminati[71a,71b], A. Carnelli[135], M. Carnesale[75a,75b], S. Caron[113], E. Carquin[137f], S. Carrá[71a], G. Carratta[23a,23b], F. Carrio Argos[33g], J. W. S. Carter[155], T. M. Carter[52], M. P. Casado[13,i], M. Caspar[48], E. G. Castiglia[172], F. L. Castillo[4], L. Castillo Garcia[13], V. Castillo Gimenez[163], N. F. Castro[130a,130e], A. Catinaccio[36], J. R. Catmore[125], V. Cavaliere[29], N. Cavalli[23a,23b], V. Cavasinni[74a,74b], Y. C. Cekmecelioglu[48], E. Celebi[21a], F. Celli[126], M. S. Centonze[70a,70b], V. Cepaitis[56], K. Cerny[122], A. S. Cerqueira[83a], A. Cerri[146], L. Cerrito[76a,76b], F. Cerutti[17a], B. Cervato[141], A. Cervelli[23b], G. Cesarini[53], S. A. Cetin[82], Z. Chadi[35a], D. Chakraborty[115], J. Chan[170], W. Y. Chan[153], J. D. Chapman[32], E. Chapon[135], B. Chargeishvili[149b], D. G. Charlton[20], T. P. Charman[94], M. Chatterjee[19], C. Chauhan[133], S. Chekanov[6], S. V. Chekulaev[156a], G. A. Chelkov[38,a], A. Chen[106], B. Chen[151], B. Chen[165], H. Chen[14c], H. Chen[29], J. Chen[62c], J. Chen[142], M. Chen[126], S. Chen[153], S. J. Chen[14c], X. Chen[62c,135], X. Chen[14b,ag], Y. Chen[62a], C. L. Cheng[170], H. C. Cheng[64a], S. Cheong[143], A. Cheplakov[38], E. Cheremushkina[48], E. Cherepanova[114], R. Cherkaoui El Moursli[35e], E. Cheu[7], K. Cheung[65], L. Chevalier[135], V. Chiarella[53], G. Chiarelli[74a], N. Chiedde[102], G. Chiodini[70a], A. S. Chisholm[20], A. Chitan[27b], M. Chitishvili[163], M. V. Chizhov[38,r], K. Choi[11], A. R. Chomont[75a,75b], Y. Chou[103], E. Y. S. Chow[114], T. Chowdhury[33g], K. L. Chu[169], M. C. Chu[64a], X. Chu[14a,14e], J. Chudoba[131], J. J. Chwastowski[87], D. Cieri[110], K. M. Ciesla[86a], V. Cindro[93], A. Ciocio[17a], F. Cirotto[72a,72b], Z. H. Citron[169,k], M. Citterio[71a], D. A. Ciubotaru[27b], B. M. Ciungu[155], A. Clark[56], P. J. Clark[52], J. M. Clavijo Columbie[48], S. E. Clawson[48], C. Clement[47a,47b], J. Clercx[48], L. Clissa[23a,23b], Y. Coadou[102], M. Cobal[69a,69c], A. Coccaro[57b], R. F. Coelho Barrue[130a], R. Coelho Lopes De Sa[103], S. Coelli[71a], H. Cohen[151], A. E. C. Coimbra[71a,71b], B. Cole[41], J. Collot[60], P. Conde Muiño[130a,130g], M. P. Connell[33c], S. H. Connell[33c], I. A. Connelly[59], E. I. Conroy[126], F. Conventi[72a,ai], H. G. Cooke[20], A. M. Cooper-Sarkar[126], A. Cordeiro Oudot Choi[127], F. Cormier[164], L. D. Corpe[40], M. Corradi[75a,75b], F. Corriveau[104,x], A. Cortes-Gonzalez[18], M. J. Costa[163], F. Costanza[4], D. Costanzo[139], B. M. Cote[119], G. Cowan[95], K. Cranmer[170], D. Cremonini[23a,23b], S. Crépé-Renaudin[60], F. Crescioli[127], M. Cristinziani[141], M. Cristoforetti[78a,78b], V. Croft[114], J. E. Crosby[121], G. Crosetti[43a,43b], A. Cueto[99], T. Cuhadar Donszelmann[160], H. Cui[14a,14e], Z. Cui[7], W. R. Cunningham[59], F. Curcio[43a,43b], P. Czodrowski[36], M. M. Czurylo[63b], M. J. Da Cunha Sargedas De Sousa[57a,57b], J. V. Da Fonseca Pinto[83b], C. Da Via[101], W. Dabrowski[86a], T. Dado[49], S. Dahbi[33g], T. Dai[106], D. Dal Santo[19], C. Dallapiccola[103], M. Dam[42], G. D'amen[29], V. D'Amico[109], J. Damp[100], J. R. Dandoy[128], M. F. Daneri[30], M. Danninger[142], V. Dao[36], G. Darbo[57b], S. Darmora[6], S.J. Das[29,aj], S. D'Auria[71a,71b], C. David[156b], T. Davidek[133], B. Davis-Purcell[34], I. Dawson[94], H. A. Day-hall[132], K. De[8], R. De Asmundis[72a], N. De Biase[48], S. De Castro[23a,23b], N. De Groot[113], P. de Jong[114], H. De la Torre[115], A. De Maria[14c], A. De Salvo[75a], U. De Sanctis[76a,76b], A. De Santo[146], J. B. De Vivie De Regie[60], D. V. Dedovich[38], J. Degens[114], A. M. Deiana[44], F. Del Corso[23a,23b], J. Del Peso[99], F. Del Rio[63a], F. Deliot[135], C. M. Delitzsch[49], M. Della Pietra[72a,72b], D. Della Volpe[56], A. Dell'Acqua[36], L. Dell'Asta[71a,71b], M. Delmastro[4], P. A. Delsart[60], S. Demers[172], M. Demichev[38], S. P. Denisov[37], L. D'Eramo[40], D. Derendarz[87], F. Derue[127], P. Dervan[92], K. Desch[24], C. Deutsch[24], F. A. Di Bello[57a,57b], A. Di Ciaccio[76a,76b], L. Di Ciaccio[4], A. Di Domenico[75a,75b], C. Di Donato[72a,72b], A. Di Girolamo[36], G. Di Gregorio[36], A. Di Luca[78a,78b], B. Di Micco[77a,77b], R. Di Nardo[77a,77b], C. Diaconu[102], M. Diamantopoulou[34], F. A. Dias[114], T. Dias Do Vale[142], M. A. Diaz[137a,137b], F. G. Diaz Capriles[24], M. Didenko[163], E. B. Diehl[106], L. Diehl[54], S. Díez Cornell[48], C. Diez Pardos[141], C. Dimitriadi[24,161], A. Dimitrievska[17a], J. Dingfelder[24], I.-

M. Dinu[27b], S. J. Dittmeier[63b], F. Dittus[36], F. Djama[102], T. Djobava[149b], J. I. Djuvsland[16], C. Doglioni[98,101], A. Dohnalova[28a], J. Dolejsi[133], Z. Dolezal[133], K. M. Dona[39], M. Donadelli[83c], B. Dong[107], J. Donini[40], A. D'Onofrio[77a,77b], M. D'Onofrio[92], J. Dopke[134], A. Doria[72a], N. Dos Santos Fernandes[130a], P. Dougan[101], M. T. Dova[90], A. T. Doyle[59], M. A. Draguet[126], E. Dreyer[169], I. Drivas-koulouris[10], A. S. Drobac[158], M. Drozdova[56], D. Du[62a], T. A. du Pree[114], F. Dubinin[37], M. Dubovsky[28a], E. Duchovni[169], G. Duckeck[109], O. A. Ducu[27b], D. Duda[52], A. Dudarev[36], E. R. Duden[26], M. D'uffizi[101], L. Duflot[66], M. Dührssen[36], C. Dülsen[171], A. E. Dumitriu[27b], M. Dunford[63a], S. Dungs[49], K. Dunne[47a,47b], A. Duperrin[102], H. Duran Yildiz[3a], M. Düren[58], A. Durglishvili[149b], B. L. Dwyer[115], G. I. Dyckes[17a], M. Dyndal[86a], S. Dysch[101], B. S. Dziedzic[87], Z. O. Earnshaw[146], G. H. Eberwein[126], B. Eckerova[28a], S. Eggebrecht[55], E. Egidio Purcino De Souza[127], L. F. Ehrke[56], G. Eigen[16], K. Einsweiler[17a], T. Ekelof[161], P. A. Ekman[98], S. El Farkh[35b], Y. El Ghazali[35b], H. El Jarrari[35e,148], A. El Moussaouy[108], V. Ellajosyula[161], M. Ellert[161], F. Ellinghaus[171], A. A. Elliot[94], N. Ellis[36], J. Elmsheuser[29], M. Elsing[36], D. Emeliyanov[134], Y. Enari[153], I. Ene[17a], S. Epari[13], J. Erdmann[49], P. A. Erland[87], M. Errenst[171], M. Escalier[66], C. Escobar[163], E. Etzion[151], G. Evans[130a], H. Evans[68], L. S. Evans[95], M. O. Evans[146], A. Ezhilov[37], S. Ezzarqtouni[35a], F. Fabbri[59], L. Fabbri[23a,23b], G. Facini[96], V. Fadeyev[136], R. M. Fakhrutdinov[37], S. Falciano[75a], L. F. Falda Ulhoa Coelho[36], P. J. Falke[24], J. Faltova[133], C. Fan[162], Y. Fan[14a], Y. Fang[14a,14e], M. Fanti[71a,71b], M. Faraj[69a,69b], Z. Farazpay[97], A. Farbin[8], A. Farilla[77a], T. Farooque[107], S. M. Farrington[52], F. Fassi[35e], D. Fassouliotis[9], M. Faucci Giannelli[76a,76b], W. J. Fawcett[32], L. Fayard[66], P. Federic[133], P. Federicova[131], O. L. Fedin[37,a], G. Fedotov[37], M. Feickert[170], L. Feligioni[102], D. E. Fellers[123], C. Feng[62b], M. Feng[14b], Z. Feng[114], M. J. Fenton[160], A. B. Fenyuk[37], L. Ferencz[48], R. A. M. Ferguson[91], S. I. Fernandez Luengo[137f], M. J. V. Fernoux[102], J. Ferrando[48], A. Ferrari[161], P. Ferrari[113,114], R. Ferrari[73a], D. Ferrere[56], C. Ferretti[106], F. Fiedler[100], P. Fiedler[132], A. Filipčič[93], E. K. Filmer[1], F. Filthaut[113], M. C. N. Fiolhais[130a,130c,c], L. Fiorini[163], W. C. Fisher[107], T. Fitschen[101], P. M. Fitzhugh[135], I. Fleck[141], P. Fleischmann[106], T. Flick[171], M. Flores[33d,ad], L. R. Flores Castillo[64a], L. Flores Sanz De Acedo[36], F. M. Follega[78a,78b], N. Fomin[16], J. H. Foo[155], B. C. Forland[68], A. Formica[135], A. C. Forti[101], E. Fortin[36], A. W. Fortman[61], M. G. Foti[17a], L. Fountas[9,j], D. Fournier[66], H. Fox[91], P. Francavilla[74a,74b], S. Francescato[61], S. Franchellucci[56], M. Franchini[23a,23b], S. Franchino[63a], D. Francis[36], L. Franco[113], V. Franco Lima[36], L. Franconi[48], M. Franklin[61], G. Frattari[26], A. C. Freegard[94], W. S. Freund[83b], Y. Y. Frid[151], J. Friend[59], N. Fritzsche[50], A. Froch[54], D. Froidevaux[36], J. A. Frost[126], Y. Fu[62a], M. Fujimoto[118,ae], E. Fullana Torregrosa[163,*], K. Y. Fung[64a], E. Furtado De Simas Filho[83b], M. Furukawa[153], J. Fuster[163], A. Gabrielli[23a,23b], A. Gabrielli[155], P. Gadow[36], G. Gagliardi[57a,57b], L. G. Gagnon[17a], E. J. Gallas[126], B. J. Gallop[134], K. K. Gan[119], S. Ganguly[153], J. Gao[62a], Y. Gao[52], F. M. Garay Walls[137a,137b], B. Garcia[29], C. García[163], A. Garcia Alonso[114], A. G. Garcia Caffaro[172], J. E. García Navarro[163], M. Garcia-Sciveres[17a], G. L. Gardner[128], R. W. Gardner[39], N. Garelli[158], D. Garg[80], R. B. Garg[143,n], J. M. Gargan[52], C. A. Garner[155], C. M. Garvey[33a], S. J. Gasiorowski[138], P. Gaspar[83b], G. Gaudio[73a], V. Gautam[13], P. Gauzzi[75a,75b], I. L. Gavrilenko[37], A. Gavrilyuk[37], C. Gay[164], G. Gaycken[48], E. N. Gazis[10], A. A. Geanta[27b], C. M. Gee[136], C. Gemme[57b], M. H. Genest[60], S. Gentile[75a,75b], A. D. Gentry[112], S. George[95], W. F. George[20], T. Geralis[46], P. Gessinger-Befurt[36], M. E. Geyik[171], M. Ghani[167], M. Ghneimat[141], K. Ghorbanian[94], A. Ghosal[141], A. Ghosh[160], A. Ghosh[7], B. Giacobbe[23b], S. Giagu[75a,75b], T. Giani[114], P. Giannetti[74a], A. Giannini[62a], S. M. Gibson[95], M. Gignac[136], D. T. Gil[86b], A. K. Gilbert[86a], B. J. Gilbert[41], D. Gillberg[34], G. Gilles[114], N. E. K. Gillwald[48], L. Ginabat[127], D. M. Gingrich[2,ah], M. P. Giordani[69a,69c], P. F. Giraud[135], G. Giugliarelli[69a,69c], D. Giugni[71a], F. Giuli[36], I. Gkialas[9,j], L. K. Gladilin[37], C. Glasman[99], G. R. Gledhill[123], G. Glemža[48], M. Glisic[123], I. Gnesi[43b,f], Y. Go[29,aj], M. Goblirsch-Kolb[36], B. Gocke[49], D. Godin[108], B. Gokturk[21a], S. Goldfarb[105], T. Golling[56], M. G. D. Gololo[33g], D. Golubkov[37], J. P. Gombas[107], A. Gomes[130a,130b], G. Gomes Da Silva[141], A. J. Gomez Delegido[163], R. Gonçalo[130a,130c], G. Gonella[123], L. Gonella[20], A. Gongadze[149c], F. Gonnella[20], J. L. Gonski[41], R. Y. González Andana[52], S. González de la Hoz[163], S. Gonzalez Fernandez[13], R. Gonzalez Lopez[92], C. Gonzalez Renteria[17a], M. V. Gonzalez Rodrigues[48], R. Gonzalez Suarez[161], S. Gonzalez-Sevilla[56], G. R. Gonzalvo Rodriguez[163], L. Goossens[36], B. Gorini[36], E. Gorini[70a,70b], A. Gorišek[93], T. C. Gosart[128], A. T. Goshaw[51], M. I. Gostkin[38], S. Goswami[121], C. A. Gottardo[36], S. A. Gotz[109], M. Gouighri[35b], V. Goumarre[48], A. G. Goussiou[138], N. Govender[33c], I. Grabowska-Bold[86a], K. Graham[34], E. Gramstad[125], S. Grancagnolo[70a,70b], M. Grandi[146], C. M. Grant[1,135], P. M. Gravila[27f], F. G. Gravili[70a,70b], H. M. Gray[17a], M. Greco[70a,70b], C. Grefe[24], I. M. Gregor[48], P. Grenier[143], C. Grieco[13], A. A. Grillo[136], K. Grimm[31], S. Grinstein[13,t],

J.-F. Grivaz[66], E. Gross[169], J. Grosse-Knetter[55], C. Grud[106], J. C. Grundy[126], L. Guan[106], W. Guan[29], C. Gubbels[164], J. G. R. Guerrero Rojas[163], G. Guerrieri[69a,69c], F. Guescini[110], R. Gugel[100], J. A. M. Guhit[106], A. Guida[18], T. Guillemin[4], E. Guilloton[134,167], S. Guindon[36], F. Guo[14a,14e], J. Guo[62c], L. Guo[48], Y. Guo[106], R. Gupta[48], S. Gurbuz[24], S. S. Gurdasani[54], G. Gustavino[36], M. Guth[56], P. Gutierrez[120], L. F. Gutierrez Zagazeta[128], C. Gutschow[96], C. Gwenlan[126], C. B. Gwilliam[92], E. S. Haaland[125], A. Haas[117], M. Habedank[48], C. Haber[17a], H. K. Hadavand[8], A. Hadef[100], S. Hadzic[110], J. J. Hahn[141], E. H. Haines[96], M. Haleem[166], J. Haley[121], J. J. Hall[139], G. D. Hallewell[102], L. Halser[19], K. Hamano[165], M. Hamer[24], G. N. Hamity[52], E. J. Hampshire[95], J. Han[62b], K. Han[62a], L. Han[14c], L. Han[62a], S. Han[17a], Y. F. Han[155], K. Hanagaki[84], M. Hance[136], D. A. Hangal[41,ac], H. Hanif[142], M. D. Hank[128], R. Hankache[101], J. B. Hansen[42], J. D. Hansen[42], P. H. Hansen[42], K. Hara[157], D. Harada[56], T. Harenberg[171], S. Harkusha[37], M. L. Harris[103], Y. T. Harris[126], J. Harrison[13], N. M. Harrison[119], P. F. Harrison[167], N. M. Hartman[110], N. M. Hartmann[109], Y. Hasegawa[140], R. Hauser[107], C. M. Hawkes[20], R. J. Hawkings[36], Y. Hayashi[153], S. Hayashida[111], D. Hayden[107], C. Hayes[106], R. L. Hayes[114], C. P. Hays[126], J. M. Hays[94], H. S. Hayward[92], F. He[62a], M. He[14a,14e], Y. He[154], Y. He[48], N. B. Heatley[94], V. Hedberg[98], A. L. Heggelund[125], N. D. Hehir[94,*], C. Heidegger[54], K. K. Heidegger[54], W. D. Heidorn[81], J. Heilman[34], S. Heim[48], T. Heim[17a], J. G. Heinlein[128], J. J. Heinrich[123], L. Heinrich[110,af], J. Hejbal[131], L. Helary[48], A. Held[170], S. Hellesund[16], C. M. Helling[164], S. Hellman[47a,47b], R. C. W. Henderson[91], L. Henkelmann[32], A. M. Henriques Correia[36], H. Herde[98], Y. Hernández Jiménez[145], L. M. Herrmann[24], T. Herrmann[50], G. Herten[54], R. Hertenberger[109], L. Hervas[36], M. E. Hesping[100], N. P. Hessey[156a], H. Hibi[85], E. Hill[155], S. J. Hillier[20], J. R. Hinds[107], F. Hinterkeuser[24], M. Hirose[124], S. Hirose[157], D. Hirschbuehl[171], T. G. Hitchings[101], B. Hiti[93], J. Hobbs[145], R. Hobincu[27e], N. Hod[169], M. C. Hodgkinson[139], B. H. Hodkinson[32], A. Hoecker[36], J. Hofer[48], T. Holm[24], M. Holzbock[110], L. B. A. H. Hommels[32], B. P. Honan[101], J. Hong[62c], T. M. Hong[129], B. H. Hooberman[162], W. H. Hopkins[6], Y. Horii[111], S. Hou[148], A. S. Howard[93], J. Howarth[59], J. Hoya[6], M. Hrabovsky[122], A. Hrynevich[48], T. Hryn'ova[4], P. J. Hsu[65], S.-C. Hsu[138], Q. Hu[62a], Y. F. Hu[14a,14e], S. Huang[64b], X. Huang[14c], Y. Huang[139], Y. Huang[14a], Z. Huang[101], Z. Hubacek[132], M. Huebner[24], F. Huegging[24], T. B. Huffman[126], C. A. Hugli[48], M. Huhtinen[36], S. K. Huiberts[16], R. Hulsken[104], N. Huseynov[12], J. Huston[107], J. Huth[61], R. Hyneman[143], G. Iacobucci[56], G. Iakovidis[29], I. Ibragimov[141], L. Iconomidou-Fayard[66], P. Iengo[72a,72b], R. Iguchi[153], T. Iizawa[126], Y. Ikegami[84], N. Ilic[155], H. Imam[35a], M. Ince Lezki[56], T. Ingebretsen Carlson[47a,47b], G. Introzzi[73a,73b], M. Iodice[77a], V. Ippolito[75a,75b], R. K. Irwin[92], M. Ishino[153], W. Islam[170], C. Issever[18,48], S. Istin[21a,al], H. Ito[168], J. M. Iturbe Ponce[64a], R. Iuppa[78a,78b], A. Ivina[169], J. M. Izen[45], V. Izzo[72a], P. Jacka[131,132], P. Jackson[1], R. M. Jacobs[48], B. P. Jaeger[142], C. S. Jagfeld[109], G. Jain[156a], P. Jain[54], G. Jäkel[171], K. Jakobs[54], T. Jakoubek[169], J. Jamieson[59], K. W. Janas[86a], M. Javurkova[103], F. Jeanneau[135], L. Jeanty[123], J. Jejelava[149a,aa], P. Jenni[54,g], C. E. Jessiman[34], S. Jézéquel[4], C. Jia[62b], J. Jia[145], X. Jia[61], X. Jia[14a,14e], Z. Jia[14c], Y. Jiang[62a], S. Jiggins[48], J. Jimenez Pena[13], S. Jin[14c], A. Jinaru[27b], O. Jinnouchi[154], P. Johansson[139], K. A. Johns[7], J. W. Johnson[136], D. M. Jones[32], E. Jones[48], P. Jones[32], R. W. L. Jones[91], T. J. Jones[92], H. L. Joos[36,55], R. Joshi[119], J. Jovicevic[15], X. Ju[17a], J. J. Junggeburth[103], T. Junkermann[63a], A. Juste Rozas[13,t], M. K. Juzek[87], S. Kabana[137e], A. Kaczmarska[87], M. Kado[110], H. Kagan[119], M. Kagan[143], A. Kahn[41], A. Kahn[128], C. Kahra[100], T. Kaji[153], E. Kajomovitz[150], N. Kakati[169], I. Kalaitzidou[54], C. W. Kalderon[29], A. Kamenshchikov[155], N. J. Kang[136], D. Kar[33g], K. Karava[126], M. J. Kareem[156b], E. Karentzos[54], I. Karkanias[152], O. Karkout[114], S. N. Karpov[38], Z. M. Karpova[38], V. Kartvelishvili[91], A. N. Karyukhin[37], E. Kasimi[152], J. Katzy[48], S. Kaur[34], K. Kawade[140], M. P. Kawale[120], C. Kawamoto[88], T. Kawamoto[135], E. F. Kay[36], F. I. Kaya[158], S. Kazakos[107], V. F. Kazanin[37], Y. Ke[145], J. M. Keaveney[33a], R. Keeler[165], G. V. Kehris[61], J. S. Keller[34], A. S. Kelly[96], J. J. Kempster[146], K. E. Kennedy[41], P. D. Kennedy[100], O. Kepka[131], B. P. Kerridge[167], S. Kersten[171], B. P. Kerševan[93], S. Keshri[66], L. Keszeghova[28a], S. Ketabchi Haghighat[155], M. Khandoga[127], A. Khanov[121], A. G. Kharlamov[37], T. Kharlamova[37], E. E. Khoda[138], M. Kholodenko[37], T. J. Khoo[18], G. Khoriauli[166], J. Khubua[149b,*], Y. A. R. Khwaira[66], A. Kilgallon[123], D. W. Kim[47a,47b], Y. K. Kim[39], N. Kimura[96], M. K. Kingston[55], A. Kirchhoff[55], C. Kirfel[24], F. Kirfel[24], J. Kirk[134], A. E. Kiryunin[110], C. Kitsaki[10], O. Kivernyk[24], M. Klassen[63a], C. Klein[34], L. Klein[166], M. H. Klein[106], M. Klein[92,*], S. B. Klein[56], U. Klein[92], P. Klimek[36], A. Klimentov[29], T. Klioutchnikova[36], P. Kluit[114], S. Kluth[110], E. Kneringer[79], T. M. Knight[155], A. Knue[49], R. Kobayashi[88], D. Kobylianskii[169], S. F. Koch[126], M. Kocian[143], P. Kodyš[133], D. M. Koeck[123], P. T. Koenig[24], T. Koffas[34], M. Kolb[135], I. Koletsou[4], T. Komarek[122], K. Köneke[54], A. X. Y. Kong[1], T. Kono[118], N. Konstantinidis[96],

B. Konya[98], R. Kopeliansky[68], S. Koperny[86a], K. Korcyl[87], K. Kordas[152,e], G. Koren[151], A. Korn[96], S. Korn[55], I. Korolkov[13], N. Korotkova[37], B. Kortman[114], O. Kortner[110], S. Kortner[110], W. H. Kostecka[115], V. V. Kostyukhin[141], A. Kotsokechagia[135], A. Kotwal[51], A. Koulouris[36], A. Kourkoumeli-Charalampidi[73a,73b], C. Kourkoumelis[9], E. Kourlitis[110,af], O. Kovanda[146], R. Kowalewski[165], W. Kozanecki[135], A. S. Kozhin[37], V. A. Kramarenko[37], G. Kramberger[93], P. Kramer[100], M. W. Krasny[127], A. Krasznahorkay[36], J. W. Kraus[171], J. A. Kremer[48], T. Kresse[50], J. Kretzschmar[92], K. Kreul[18], P. Krieger[155], S. Krishnamurthy[103], M. Krivos[133], K. Krizka[20], K. Kroeninger[49], H. Kroha[110], J. Kroll[131], J. Kroll[128], K. S. Krowpman[107], U. Kruchonak[38], H. Krüger[24], N. Krumnack[81], M. C. Kruse[51], J. A. Krzysiak[87], O. Kuchinskaia[37], S. Kuday[3a], S. Kuehn[36], R. Kuesters[54], T. Kuhl[48], V. Kukhtin[38], Y. Kulchitsky[37,a], S. Kuleshov[137b,137d], M. Kumar[33g], N. Kumari[48], A. Kupco[131], T. Kupfer[49], A. Kupich[37], O. Kuprash[54], H. Kurashige[85], L. L. Kurchaninov[156a], O. Kurdysh[66], Y. A. Kurochkin[37], A. Kurova[37], M. Kuze[154], A. K. Kvam[103], J. Kvita[122], T. Kwan[104], N. G. Kyriacou[106], L. A. O. Laatu[102], C. Lacasta[163], F. Lacava[75a,75b], H. Lacker[18], D. Lacour[127], N. N. Lad[96], E. Ladygin[38], B. Laforge[127], T. Lagouri[137e], F. Z. Lahbabi[35a], S. Lai[55], I. K. Lakomiec[86a], N. Lalloue[60], J. E. Lambert[165], S. Lammers[68], W. Lampl[7], C. Lampoudis[152,e], A. N. Lancaster[115], E. Lançon[29], U. Landgraf[54], M. P. J. Landon[94], V. S. Lang[54], R. J. Langenberg[103], O. K. B. Langrekken[125], A. J. Lankford[160], F. Lanni[36], K. Lantzsch[24], A. Lanza[73a], A. Lapertosa[57a,57b], J. F. Laporte[135], T. Lari[71a], F. Lasagni Manghi[23b], M. Lassnig[36], V. Latonova[131], A. Laudrain[100], A. Laurier[150], S. D. Lawlor[139], Z. Lawrence[101], M. Lazzaroni[71a,71b], B. Le[101], E. M. Le Boulicaut[51], B. Leban[93], A. Lebedev[81], M. LeBlanc[101], F. Ledroit-Guillon[60], A. C. A. Lee[96], S. C. Lee[148], S. Lee[47a,47b], T. F. Lee[92], L. L. Leeuw[33c], H. P. Lefebvre[95], M. Lefebvre[165], C. Leggett[17a], G. Lehmann Miotto[36], M. Leigh[56], W. A. Leight[103], W. Leinonen[113], A. Leisos[152,s], M. A. L. Leite[83c], C. E. Leitgeb[48], R. Leitner[133], K. J. C. Leney[44], T. Lenz[24], S. Leone[74a], C. Leonidopoulos[52], A. Leopold[144], C. Leroy[108], R. Les[107], C. G. Lester[32], M. Levchenko[37], J. Levêque[4], D. Levin[106], L. J. Levinson[169], M. P. Lewicki[87], D. J. Lewis[4], A. Li[5], B. Li[62b], C. Li[62a], C.-Q. Li[62c], H. Li[62a], H. Li[62b], H. Li[14c], H. Li[14b], H. Li[62b], K. Li[138], L. Li[62c], M. Li[14a,14e], Q. Y. Li[62a], S. Li[14a,14e], S. Li[62c,62d,d], T. Li[5], X. Li[104], Z. Li[126], Z. Li[104], Z. Li[92], Z. Li[14a,14e], S. Liang[14a,14e], Z. Liang[14a], M. Liberatore[135], B. Liberti[76a], K. Lie[64c], J. Lieber Marin[83b], H. Lien[68], K. Lin[107], R. E. Lindley[7], J. H. Lindon[2], E. Lipeles[128], A. Lipniacka[16], A. Lister[164], J. D. Little[4], B. Liu[14a], B. X. Liu[142], D. Liu[62c,62d], J. B. Liu[62a], J. K. K. Liu[32], K. Liu[62c,62d], M. Liu[62a], M. Y. Liu[62a], P. Liu[14a], Q. Liu[62c,62d,138], X. Liu[62a], Y. Liu[14d,14e], Y. L. Liu[62b], Y. W. Liu[62a], J. Llorente Merino[142], S. L. Lloyd[94], E. M. Lobodzinska[48], P. Loch[7], S. Loffredo[76a,76b], T. Lohse[18], K. Lohwasser[139], E. Loiacono[48], M. Lokajicek[131,*], J. D. Lomas[20], J. D. Long[162], I. Longarini[160], L. Longo[70a,70b], R. Longo[162], I. Lopez Paz[67], A. Lopez Solis[48], J. Lorenz[109], N. Lorenzo Martinez[4], A. M. Lory[109], G. Löschcke Centeno[146], O. Loseva[37], X. Lou[47a,47b], X. Lou[14a,14e], A. Lounis[66], J. Love[6], P. A. Love[91], G. Lu[14a,14e], M. Lu[80], S. Lu[128], Y. J. Lu[65], H. J. Lubatti[138], C. Luci[75a,75b], F. L. Lucio Alves[14c], A. Lucotte[60], F. Luehring[68], I. Luise[145], O. Lukianchuk[66], O. Lundberg[144], B. Lund-Jensen[144,*], N. A. Luongo[123], M. S. Lutz[151], A. B. Lux[25], D. Lynn[29], H. Lyons[92], R. Lysak[131], E. Lytken[98], V. Lyubushkin[38], T. Lyubushkina[38], M. M. Lyukova[145], H. Ma[29], K. Ma[62a], L. L. Ma[62b], Y. Ma[121], D. M. Mac Donell[165], G. Maccarrone[53], J. C. MacDonald[100], P. C. Machado De Abreu Farias[83b], R. Madar[40], W. F. Mader[50], T. Madula[96], J. Maeda[85], T. Maeno[29], H. Maguire[139], V. Maiboroda[135], A. Maio[130a,130b,130d], K. Maj[86a], O. Majersky[48], S. Majewski[123], N. Makovec[66], V. Maksimovic[15], B. Malaescu[127], Pa. Malecki[87], V. P. Maleev[37], F. Malek[60], M. Mali[93], D. Malito[95], U. Mallik[80,*], S. Maltezos[10], S. Malyukov[38], J. Mamuzic[13], G. Mancini[53], G. Manco[73a,73b], J. P. Mandalia[94], I. Mandić[93], L. Manhaes de Andrade Filho[83a], I. M. Maniatis[169], J. Manjarres Ramos[102,ab], D. C. Mankad[169], A. Mann[109], B. Mansoulie[135], S. Manzoni[36], A. Marantis[152,s], G. Marchiori[5], M. Marcisovsky[131], C. Marcon[71a], M. Marinescu[20], M. Marjanovic[120], E. J. Marshall[91], Z. Marshall[17a], S. Marti-Garcia[163], T. A. Martin[167], V. J. Martin[52], B. Martin dit Latour[16], L. Martinelli[75a,75b], M. Martinez[13,t], P. Martinez Agullo[163], V. I. Martinez Outschoorn[103], P. Martinez Suarez[13], S. Martin-Haugh[134], V. S. Martoiu[27b], A. C. Martyniuk[96], A. Marzin[36], D. Mascione[78a,78b], L. Masetti[100], T. Mashimo[153], J. Masik[101], A. L. Maslennikov[37], L. Massa[23b], P. Massarotti[72a,72b], P. Mastrandrea[74a,74b], A. Mastroberardino[43a,43b], T. Masubuchi[153], T. Mathisen[161], J. Matousek[133], N. Matsuzawa[153], J. Maurer[27b], B. Maček[93], D. A. Maximov[37], R. Mazini[148], I. Maznas[152], M. Mazza[107], S. M. Mazza[136], E. Mazzeo[71a,71b], C. Mc Ginn[29], J. P. Mc Gowan[104], S. P. Mc Kee[106], E. F. McDonald[105], A. E. McDougall[114], J. A. Mcfayden[146], R. P. McGovern[128], G. Mchedlidze[149b], R. P. Mckenzie[33g], T. C. Mclachlan[48], D. J. Mclaughlin[96], S. J. McMahon[134],

P. C. McNamara[105], C. M. Mcpartland[92], R. A. McPherson[165,x], S. Mehlhase[109], A. Mehta[92], D. Melini[150], B. R. Mellado Garcia[33g], A. H. Melo[55], F. Meloni[48], A. M. Mendes Jacques Da Costa[101], H. Y. Meng[155], L. Meng[91], S. Menke[110], M. Mentink[36], E. Meoni[43a,43b], C. Merlassino[126], L. Merola[72a,72b], C. Meroni[71a,71b], G. Merz[106], O. Meshkov[37], J. Metcalfe[6], A. S. Mete[6], C. Meyer[68], J.-P. Meyer[135], R. P. Middleton[134], L. Mijović[52], G. Mikenberg[169], M. Mikestikova[131], M. Mikuž[93], H. Mildner[100], A. Milic[36], C. D. Milke[44], D. W. Miller[39], L. S. Miller[34], A. Milov[169], D. A. Milstead[47a,47b], T. Min[14c], A. A. Minaenko[37], I. A. Minashvili[149b], L. Mince[59], A. I. Mincer[117], B. Mindur[86a], M. Mineev[38], Y. Mino[88], L. M. Mir[13], M. Miralles Lopez[163], M. Mironova[17a], A. Mishima[153], M. C. Missio[113], A. Mitra[167], V. A. Mitsou[163], Y. Mitsumori[111], O. Miu[155], P. S. Miyagawa[94], T. Mkrtchyan[63a], M. Mlinarevic[96], T. Mlinarevic[96], M. Mlynarikova[36], S. Mobius[19], P. Moder[48], P. Mogg[109], A. F. Mohammed[14a,14e], S. Mohapatra[41], G. Mokgatitswane[33g], L. Moleri[169], B. Mondal[141], S. Mondal[132], K. Mönig[48], E. Monnier[102], L. Monsonis Romero[163], J. Montejo Berlingen[13], M. Montella[119], F. Montereali[77a,77b], F. Monticelli[90], S. Monzani[69a,69c], N. Morange[66], A. L. Moreira De Carvalho[130a], M. Moreno Llácer[163], C. Moreno Martinez[56], P. Morettini[57b], S. Morgenstern[36], M. Morii[61], M. Morinaga[153], A. K. Morley[36], F. Morodei[75a,75b], L. Morvaj[36], P. Moschovakos[36], B. Moser[36], M. Mosidze[149b], T. Moskalets[54], P. Moskvitina[113], J. Moss[31,l], E. J. W. Moyse[103], O. Mtintsilana[33g], S. Muanza[102], J. Mueller[129], D. Muenstermann[91], R. Müller[19], G. A. Mullier[161], A. J. Mullin[32], J. J. Mullin[128], D. P. Mungo[155], D. Munoz Perez[163], F. J. Munoz Sanchez[101], M. Murin[101], W. J. Murray[167,134], A. Murrone[71a,71b], J. M. Muse[120], M. Muškinja[17a], C. Mwewa[29], A. G. Myagkov[37,a], A. J. Myers[8], A. A. Myers[129], G. Myers[68], M. Myska[132], B. P. Nachman[17a], O. Nackenhorst[49], A. Nag[50], K. Nagai[126], K. Nagano[84], J. L. Nagle[29,aj], E. Nagy[102], A. M. Nairz[36], Y. Nakahama[84], K. Nakamura[84], K. Nakkalil[5], H. Nanjo[124], R. Narayan[44], E. A. Narayanan[112], I. Naryshkin[37], M. Naseri[34], S. Nasri[159], C. Nass[24], G. Navarro[22a], J. Navarro-Gonzalez[163], R. Nayak[151], A. Nayaz[18], P. Y. Nechaeva[37], F. Nechansky[48], L. Nedic[126], T. J. Neep[20], A. Negri[73a,73b], M. Negrini[23b], C. Nellist[114], C. Nelson[104], K. Nelson[106], S. Nemecek[131], M. Nessi[36,h], M. S. Neubauer[162], F. Neuhaus[100], J. Neundorf[48], R. Newhouse[164], P. R. Newman[20], C. W. Ng[129], Y. W. Y. Ng[48], B. Ngair[35e], H. D. N. Nguyen[108], R. B. Nickerson[126], R. Nicolaidou[135], J. Nielsen[136], M. Niemeyer[55], J. Niermann[36,55], N. Nikiforou[36], V. Nikolaenko[37,a], I. Nikolic-Audit[127], K. Nikolopoulos[20], P. Nilsson[29], I. Ninca[48], H. R. Nindhito[56], G. Ninio[151], A. Nisati[75a], N. Nishu[2], R. Nisius[110], J.-E. Nitschke[50], E. K. Nkadimeng[33g], T. Nobe[153], D. L. Noel[32], T. Nommensen[147], M. B. Norfolk[139], R. R. B. Norisam[96], B. J. Norman[34], J. Novak[93], T. Novak[48], L. Novotny[132], R. Novotny[112], L. Nozka[122], K. Ntekas[160], N. M. J. Nunes De Moura Junior[83b], E. Nurse[96], J. Ocariz[127], A. Ochi[85], I. Ochoa[130a], S. Oerdek[48,u], J. T. Offermann[39], A. Ogrodnik[133], A. Oh[101], C. C. Ohm[144], H. Oide[84], R. Oishi[153], M. L. Ojeda[48], M. W. O'Keefe[92], Y. Okumura[153], L. F. Oleiro Seabra[130a], S. A. Olivares Pino[137d], D. Oliveira Damazio[29], D. Oliveira Goncalves[83a], J. L. Oliver[160], A. Olszewski[87], Ö. O. Öncel[54], A. P. O'Neill[19], A. Onofre[130a,130e], P. U. E. Onyisi[11], M. J. Oreglia[39], G. E. Orellana[90], D. Orestano[77a,77b], N. Orlando[13], R. S. Orr[155], V. O'Shea[59], L. M. Osojnak[128], R. Ospanov[62a], G. Otero y Garzon[30], H. Otono[89], P. S. Ott[63a], G. J. Ottino[17a], M. Ouchrif[35d], J. Ouellette[29], F. Ould-Saada[125], M. Owen[59], R. E. Owen[134], K. Y. Oyulmaz[21a], V. E. Ozcan[21a], N. Ozturk[8], S. Ozturk[82], H. A. Pacey[126], A. Pacheco Pages[13], C. Padilla Aranda[13], G. Padovano[75a,75b], S. Pagan Griso[17a], G. Palacino[68], A. Palazzo[70a,70b], S. Palestini[36], J. Pan[172], T. Pan[64a], D. K. Panchal[11], C. E. Pandini[114], J. G. Panduro Vazquez[95], H. D. Pandya[1], H. Pang[14b], P. Pani[48], G. Panizzo[69a,69c], L. Paolozzi[56], C. Papadatos[108], S. Parajuli[44], A. Paramonov[6], C. Paraskevopoulos[10], D. Paredes Hernandez[64b], T. H. Park[155], M. A. Parker[32], F. Parodi[57a,57b], E. W. Parrish[115], V. A. Parrish[52], J. A. Parsons[41], U. Parzefall[54], B. Pascual Dias[108], L. Pascual Dominguez[151], E. Pasqualucci[75a], S. Passaggio[57b], F. Pastore[95], P. Pasuwan[47a,47b], P. Patel[87], U. M. Patel[51], J. R. Pater[101], T. Pauly[36], J. Pearkes[143], M. Pedersen[125], R. Pedro[130a], S. V. Peleganchuk[37], O. Penc[36], E. A. Pender[52], H. Peng[62a], K. E. Penski[109], M. Penzin[37], B. S. Peralva[83d], A. P. Pereira Peixoto[60], L. Pereira Sanchez[47a,47b], D. V. Perepelitsa[29,aj], E. Perez Codina[156a], M. Perganti[10], L. Perini[71a,71b,*], H. Pernegger[36], O. Perrin[40], K. Peters[48], R. F. Y. Peters[101], B. A. Petersen[36], T. C. Petersen[42], E. Petit[102], V. Petousis[132], C. Petridou[152,e], A. Petrukhin[141], M. Pettee[17a], N. E. Pettersson[36], A. Petukhov[37], K. Petukhova[133], R. Pezoa[137f], L. Pezzotti[36], G. Pezzullo[172], T. M. Pham[170], T. Pham[105], P. W. Phillips[134], G. Piacquadio[145], E. Pianori[17a], F. Piazza[71a,71b], R. Piegaia[30], D. Pietreanu[27b], A. D. Pilkington[101], M. Pinamonti[69a,69c], J. L. Pinfold[2], B. C. Pinheiro Pereira[130a], A. E. Pinto Pinoargote[100,135], L. Pintucci[69a,69c], K. M. Piper[146],

A. Pirttikoski[56], D. A. Pizzi[34], L. Pizzimento[64b], A. Pizzini[114], M.-A. Pleier[29], V. Plesanovs[54], V. Pleskot[133], E. Plotnikova[38], G. Poddar[4], R. Poettgen[98], L. Poggioli[127], I. Pokharel[55], S. Polacek[133], G. Polesello[73a], A. Poley[142,156a], R. Polifka[132], A. Polini[23b], C. S. Pollard[167], Z. B. Pollock[119], V. Polychronakos[29], E. Pompa Pacchi[75a,75b], D. Ponomarenko[113], L. Pontecorvo[36], S. Popa[27a], G. A. Popeneciu[27d], A. Poreba[36], D. M. Portillo Quintero[156a], S. Pospisil[132], M. A. Postill[139], P. Postolache[27c], K. Potamianos[167], P. A. Potepa[86a], I. N. Potrap[38], C. J. Potter[32], H. Potti[1], T. Poulsen[48], J. Poveda[163], M. E. Pozo Astigarraga[36], A. Prades Ibanez[163], J. Pretel[54], D. Price[101], M. Primavera[70a], M. A. Principe Martin[99], R. Privara[122], T. Procter[59], M. L. Proffitt[138], N. Proklova[128], K. Prokofiev[64c], G. Proto[110], S. Protopopescu[29], J. Proudfoot[6], M. Przybycien[86a], W. W. Przygoda[86b], J. E. Puddefoot[139], D. Pudzha[37], D. Pyatiizbyantseva[37], J. Qian[106], D. Qichen[101], Y. Qin[101], T. Qiu[52], A. Quadt[55], M. Queitsch-Maitland[101], G. Quetant[56], R. P. Quinn[164], G. Rabanal Bolanos[61], D. Rafanoharana[54], F. Ragusa[71a,71b], J. L. Rainbolt[39], J. A. Raine[56], S. Rajagopalan[29], E. Ramakoti[37], K. Ran[14e,48], N. P. Rapheeha[33g], H. Rasheed[27b], V. Raskina[127], D. F. Rassloff[63a], S. Rave[100], B. Ravina[55], I. Ravinovich[169], M. Raymond[36], A. L. Read[125], N. P. Readioff[139], D. M. Rebuzzi[73a,73b], G. Redlinger[29], A. S. Reed[110], K. Reeves[26], J. A. Reidelsturz[171], D. Reikher[151], A. Rej[141], C. Rembser[36], A. Renardi[48], M. Renda[27b], M. B. Rendel[110], F. Renner[48], A. G. Rennie[160], A. L. Rescia[48], S. Resconi[71a], M. Ressegotti[57a,57b], S. Rettie[36], J. G. Reyes Rivera[107], E. Reynolds[17a], O. L. Rezanova[37], P. Reznicek[133], N. Ribaric[91], E. Ricci[78a,78b], R. Richter[110], S. Richter[47a,47b], E. Richter-Was[86b], M. Ridel[127], S. Ridouani[35d], P. Rieck[117], P. Riedler[36], E. M. Riefel[47a,47b], M. Rijssenbeek[145], A. Rimoldi[73a,73b], M. Rimoldi[48], L. Rinaldi[23a,23b], T. T. Rinn[29], M. P. Rinnagel[109], G. Ripellino[161], I. Riu[13], P. Rivadeneira[48], J. C. Rivera Vergara[165], F. Rizatdinova[121], E. Rizvi[94], B. A. Roberts[167], B. R. Roberts[17a], S. H. Robertson[104,x], D. Robinson[32], C. M. Robles Gajardo[137f], M. Robles Manzano[100], A. Robson[59], A. Rocchi[76a,76b], C. Roda[74a,74b], S. Rodriguez Bosca[63a], Y. Rodriguez Garcia[22a], A. Rodriguez Rodriguez[54], A. M. Rodríguez Vera[156b], S. Roe[36], J. T. Roemer[160], A. R. Roepe-Gier[136], J. Roggel[171], O. Røhne[125], R. A. Rojas[103], C. P. A. Roland[68], J. Roloff[29], A. Romaniouk[37], E. Romano[73a,73b], M. Romano[23b], A. C. Romero Hernandez[162], N. Rompotis[92], L. Roos[127], S. Rosati[75a], B. J. Rosser[39], E. Rossi[126], E. Rossi[72a,72b], L. P. Rossi[57b], L. Rossini[54], R. Rosten[119], M. Rotaru[27b], B. Rottler[54], C. Rougier[102,ab], D. Rousseau[66], D. Rousso[32], A. Roy[162], S. Roy-Garand[155], A. Rozanov[102], Y. Rozen[150], X. Ruan[33g], A. Rubio Jimenez[163], A. J. Ruby[92], V. H. Ruelas Rivera[18], T. A. Ruggeri[1], A. Ruggiero[126], A. Ruiz-Martinez[163], A. Rummler[36], Z. Rurikova[54], N. A. Rusakovich[38], H. L. Russell[165], G. Russo[75a,75b], J. P. Rutherfoord[7], S. Rutherford Colmenares[32], K. Rybacki[91], M. Rybar[133], E. B. Rye[125], A. Ryzhov[44], J. A. Sabater Iglesias[56], P. Sabatini[163], L. Sabetta[75a,75b], H. F.-W. Sadrozinski[136], F. Safai Tehrani[75a], B. Safarzadeh Samani[134], M. Safdari[143], S. Saha[165], M. Sahinsoy[110], M. Saimpert[135], M. Saito[153], T. Saito[153], D. Salamani[36], A. Salnikov[143], J. Salt[163], A. Salvador Salas[13], D. Salvatore[43a,43b], F. Salvatore[146], A. Salzburger[36], D. Sammel[54], D. Sampsonidis[152,e], D. Sampsonidou[123], J. Sánchez[163], A. Sanchez Pineda[4], V. Sanchez Sebastian[163], H. Sandaker[125], C. O. Sander[48], J. A. Sandesara[103], M. Sandhoff[171], C. Sandoval[22b], D. P. C. Sankey[134], T. Sano[88], A. Sansoni[53], L. Santi[75a,75b], C. Santoni[40], H. Santos[130a,130b], S. N. Santpur[17a], A. Santra[169], K. A. Saoucha[116b], J. G. Saraiva[130a,130d], J. Sardain[7], O. Sasaki[84], K. Sato[157], C. Sauer[63b], F. Sauerburger[54], E. Sauvan[4], P. Savard[155,ah], R. Sawada[153], C. Sawyer[134], L. Sawyer[97], I. Sayago Galvan[163], C. Sbarra[23b], A. Sbrizzi[23a,23b], T. Scanlon[96], J. Schaarschmidt[138], P. Schacht[110], U. Schäfer[100], A. C. Schaffer[44,66], D. Schaile[109], R. D. Schamberger[145], C. Scharf[18], M. M. Schefer[19], V. A. Schegelsky[37], D. Scheirich[133], F. Schenck[18], M. Schernau[160], C. Scheulen[55], C. Schiavi[57a,57b], E. J. Schioppa[70a,70b], M. Schioppa[43a,43b], B. Schlag[143,n], K. E. Schleicher[54], S. Schlenker[36], J. Schmeing[171], M. A. Schmidt[171], K. Schmieden[100], C. Schmitt[100], S. Schmitt[48], L. Schoeffel[135], A. Schoening[63b], P. G. Scholer[54], E. Schopf[126], M. Schott[100], J. Schovancova[36], S. Schramm[56], F. Schroeder[171], T. Schroer[56], H.-C. Schultz-Coulon[63a], M. Schumacher[54], B. A. Schumm[136], Ph. Schune[135], A. J. Schuy[138], H. R. Schwartz[136], A. Schwartzman[143], T. A. Schwarz[106], Ph. Schwemling[135], R. Schwienhorst[107], A. Sciandra[136], G. Sciolla[26], F. Scuri[74a], C. D. Sebastiani[92], K. Sedlaczek[115], P. Seema[18], S. C. Seidel[112], A. Seiden[136], B. D. Seidlitz[41], C. Seitz[48], J. M. Seixas[83b], G. Sekhniaidze[72a], S. J. Sekula[44], L. Selem[60], N. Semprini-Cesari[23a,23b], D. Sengupta[56], V. Senthilkumar[163], L. Serin[66], L. Serkin[69a,69b], M. Sessa[76a,76b], H. Severini[120], F. Sforza[57a,57b], A. Sfyrla[56], E. Shabalina[55], R. Shaheen[144], J. D. Shahinian[128], D. Shaked Renous[169], L. Y. Shan[14a], M. Shapiro[17a], A. Sharma[36], A. S. Sharma[164], P. Sharma[80], S. Sharma[48], P. B. Shatalov[37], K. Shaw[146], S. M. Shaw[101], A. Shcherbakova[37], Q. Shen[5,62c],

P. Sherwood[96], L. Shi[96], X. Shi[14a], C. O. Shimmin[172], J. D. Shinner[95], I. P. J. Shipsey[126], S. Shirabe[56,h], M. Shiyakova[38,v], J. Shlomi[169], M. J. Shochet[39], J. Shojaii[105], D. R. Shope[125], B. Shrestha[120], S. Shrestha[119,ak], E. M. Shrif[33g], M. J. Shroff[165], P. Sicho[131], A. M. Sickles[162], E. Sideras Haddad[33g], A. Sidoti[23b], F. Siegert[50], Dj. Sijacki[15], R. Sikora[86a], F. Sili[90], J. M. Silva[20], M. V. Silva Oliveira[29], S. B. Silverstein[47a], S. Simion[66], R. Simoniello[36], E. L. Simpson[59], H. Simpson[146], L. R. Simpson[106], N. D. Simpson[98], S. Simsek[82], S. Sindhu[55], P. Sinervo[155], S. Singh[155], S. Sinha[48], S. Sinha[101], M. Sioli[23a,23b], I. Siral[36], E. Sitnikova[48], S. Yu. Sivoklokov[37,*], J. Sjölin[47a,47b], A. Skaf[55], E. Skorda[20], P. Skubic[120], M. Slawinska[87], V. Smakhtin[169], B. H. Smart[134], J. Smiesko[36], S. Yu. Smirnov[37], Y. Smirnov[37], L. N. Smirnova[37,a], O. Smirnova[98], A. C. Smith[41], E. A. Smith[39], H. A. Smith[126], J. L. Smith[92], R. Smith[143], M. Smizanska[91], K. Smolek[132], A. A. Snesarev[37], S. R. Snider[155], H. L. Snoek[114], S. Snyder[29], R. Sobie[165,x], A. Soffer[151], C. A. Solans Sanchez[36], E. Yu. Soldatov[37], U. Soldevila[163], A. A. Solodkov[37], S. Solomon[26], A. Soloshenko[38], K. Solovieva[54], O. V. Solovyanov[40], V. Solovyev[37], P. Sommer[36], A. Sonay[13], W. Y. Song[156b], J. M. Sonneveld[114], A. Sopczak[132], A. L. Sopio[96], F. Sopkova[28b], V. Sothilingam[63a], S. Sottocornola[68], R. Soualah[116b], Z. Soumaimi[35e], D. South[48], N. Soybelman[169], S. Spagnolo[70a,70b], M. Spalla[110], D. Sperlich[54], G. Spigo[36], S. Spinali[91], D. P. Spiteri[59], M. Spousta[133], E. J. Staats[34], A. Stabile[71a,71b], R. Stamen[63a], A. Stampekis[20], M. Standke[24], E. Stanecka[87], M. V. Stange[50], B. Stanislaus[17a], M. M. Stanitzki[48], B. Stapf[48], E. A. Starchenko[37], G. H. Stark[136], J. Stark[102,ab], D. M. Starko[156b], P. Staroba[131], P. Starovoitov[63a], S. Stärz[104], R. Staszewski[87], G. Stavropoulos[46], J. Steentoft[161], P. Steinberg[29], B. Stelzer[142,156a], H. J. Stelzer[129], O. Stelzer-Chilton[156a], H. Stenzel[58], T. J. Stevenson[146], G. A. Stewart[36], J. R. Stewart[121], M. C. Stockton[36], G. Stoicea[27b], M. Stolarski[130a], S. Stonjek[110], A. Straessner[50], J. Strandberg[144], S. Strandberg[47a,47b], M. Stratmann[171], M. Strauss[120], T. Strebler[102], P. Strizenec[28b], R. Ströhmer[166], D. M. Strom[123], L. R. Strom[48], R. Stroynowski[44], A. Strubig[47a,47b], S. A. Stucci[29], B. Stugu[16], J. Stupak[120], N. A. Styles[48], D. Su[143], S. Su[62a], W. Su[62d], X. Su[62a,66], K. Sugizaki[153], V. V. Sulin[37], M. J. Sullivan[92], D. M. S. Sultan[78a,78b], L. Sultanaliyeva[37], S. Sultansoy[3b], T. Sumida[88], S. Sun[106], S. Sun[170], O. Sunneborn Gudnadottir[161], N. Sur[102], M. R. Sutton[146], H. Suzuki[157], M. Svatos[131], M. Swiatlowski[156a], T. Swirski[166], I. Sykora[28a], M. Sykora[133], T. Sykora[133], D. Ta[100], K. Tackmann[48,u], A. Taffard[160], R. Tafirout[156a], J. S. Tafoya Vargas[66], E. P. Takeva[52], Y. Takubo[84], M. Talby[102], A. A. Talyshev[37], K. C. Tam[64b], N. M. Tamir[151], A. Tanaka[153], J. Tanaka[153], R. Tanaka[66], M. Tanasini[57a,57b], Z. Tao[164], S. Tapia Araya[137f], S. Tapprogge[100], A. Tarek Abouelfadl Mohamed[107], S. Tarem[150], K. Tariq[14a], G. Tarna[27b,102], G. F. Tartarelli[71a], P. Tas[133], M. Tasevsky[131], E. Tassi[43a,43b], A. C. Tate[162], G. Tateno[153], Y. Tayalati[35e,w], G. N. Taylor[105], W. Taylor[156b], H. Teagle[92], A. S. Tee[170], R. Teixeira De Lima[143], P. Teixeira-Dias[95], J. J. Teoh[155], K. Terashi[153], J. Terron[99], S. Terzo[13], M. Testa[53], R. J. Teuscher[155,x], A. Thaler[79], O. Theiner[56], N. Themistokleous[52], T. Theveneaux-Pelzer[102], O. Thielmann[171], D. W. Thomas[95], J. P. Thomas[20], E. A. Thompson[17a], P. D. Thompson[20], E. Thomson[128], Y. Tian[55], V. Tikhomirov[37,a], Yu. A. Tikhonov[37], S. Timoshenko[37], D. Timoshyn[133], E. X. L. Ting[1], P. Tipton[172], S. H. Tlou[33g], A. Tnourji[40], K. Todome[154], S. Todorova-Nova[133], S. Todt[50], M. Togawa[84], J. Tojo[89], S. Tokár[28a], K. Tokushuku[84], O. Toldaiev[68], R. Tombs[32], M. Tomoto[84,111], L. Tompkins[143,n], K. W. Topolnicki[86b], E. Torrence[123], H. Torres[102,ab], E. Torró Pastor[163], M. Toscani[30], C. Tosciri[39], M. Tost[11], D. R. Tovey[139], A. Traeet[16], I. S. Trandafir[27b], T. Trefzger[166], A. Tricoli[29], I. M. Trigger[156a], S. Trincaz-Duvoid[127], D. A. Trischuk[26], B. Trocmé[60], C. Troncon[71a], L. Truong[33c], M. Trzebinski[87], A. Trzupek[87], F. Tsai[145], M. Tsai[106], A. Tsiamis[152,e], P. V. Tsiareshka[37], S. Tsigaridas[156a], A. Tsirigotis[152,s], V. Tsiskaridze[155], E. G. Tskhadadze[149a], M. Tsopoulou[152,e], Y. Tsujikawa[88], I. I. Tsukerman[37], V. Tsulaia[17a], S. Tsuno[84], O. Tsur[150], K. Tsuri[118], D. Tsybychev[145], Y. Tu[64b], A. Tudorache[27b], V. Tudorache[27b], A. N. Tuna[36], S. Turchikhin[57a,57b], I. Turk Cakir[3a], R. Turra[71a], T. Turtuvshin[38,y], P. M. Tuts[41], S. Tzamarias[152,e], P. Tzanis[10], E. Tzovara[100], F. Ukegawa[157], P. A. Ulloa Poblete[137b,137c], E. N. Umaka[29], G. Unal[36], M. Unal[11], A. Undrus[29], G. Unel[160], J. Urban[28b], P. Urquijo[105], G. Usai[8], R. Ushioda[154], M. Usman[108], Z. Uysal[21b], L. Vacavant[102], V. Vacek[132], B. Vachon[104], K. O. H. Vadla[125], T. Vafeiadis[36], A. Vaitkus[96], C. Valderanis[109], E. Valdes Santurio[47a,47b], M. Valente[156a], S. Valentinetti[23a,23b], A. Valero[163], E. Valiente Moreno[163], A. Vallier[102,ab], J. A. Valls Ferrer[163], D. R. Van Arneman[114], T. R. Van Daalen[138], A. Van Der Graaf[49], P. Van Gemmeren[6], M. Van Rijnbach[36,125], S. Van Stroud[96], I. Van Vulpen[114], M. Vanadia[76a,76b], W. Vandelli[36], M. Vandenbroucke[135], E. R. Vandewall[121], D. Vannicola[151], L. Vannoli[57a,57b], R. Vari[75a], E. W. Varnes[7], C. Varni[17b], T. Varol[148], D. Varouchas[66], L. Varriale[163], K. E. Varvell[147], M. E. Vasile[27b], L. Vaslin[40], G. A. Vasquez[165], A. Vasyukov[38], F. Vazeille[40],

T. Vazquez Schroeder[36], J. Veatch[31], V. Vecchio[101], M. J. Veen[103], I. Veliscek[126], L. M. Veloce[155], F. Veloso[130a,130c], S. Veneziano[75a], A. Ventura[70a,70b], S. Ventura Gonzalez[135], A. Verbytskyi[110], M. Verducci[74a,74b], C. Vergis[24], M. Verissimo De Araujo[83b], W. Verkerke[114], J. C. Vermeulen[114], C. Vernieri[143], M. Vessella[103], M. C. Vetterli[142,ah], A. Vgenopoulos[152,e], N. Viaux Maira[137f], T. Vickey[139], O. E. Vickey Boeriu[139], G. H. A. Viehhauser[126], L. Vigani[63b], M. Villa[23a,23b], M. Villaplana Perez[163], E. M. Villhauer[52], E. Vilucchi[53], M. G. Vincter[34], G. S. Virdee[20], A. Vishwakarma[52], A. Visibile[114], C. Vittori[36], I. Vivarelli[146], E. Voevodina[110], F. Vogel[109], P. Vokac[132], Yu. Volkotrub[86a], J. Von Ahnen[48], E. Von Toerne[24], B. Vormwald[36], V. Vorobel[133], K. Vorobev[37], M. Vos[163], K. Voss[141], J. H. Vossebeld[92], M. Vozak[114], L. Vozdecky[94], N. Vranjes[15], M. Vranjes Milosavljevic[15], M. Vreeswijk[114], N. K. Vu[62c,62d], R. Vuillermet[36], O. Vujinovic[100], I. Vukotic[39], S. Wada[157], C. Wagner[103], J. M. Wagner[17a], W. Wagner[171], S. Wahdan[171], H. Wahlberg[90], M. Wakida[111], J. Walder[134], R. Walker[109], W. Walkowiak[141], A. Wall[128], T. Wamorkar[6], A. Z. Wang[170], C. Wang[100], C. Wang[62c], H. Wang[17a], J. Wang[64a], R.-J. Wang[100], R. Wang[61], R. Wang[6], S. M. Wang[148], S. Wang[62b], T. Wang[62a], W. T. Wang[80], W. Wang[14a], X. Wang[14c], X. Wang[162], X. Wang[62c], Y. Wang[62d], Y. Wang[14c], Z. Wang[106], Z. Wang[51,62c,62d], Z. Wang[106], A. Warburton[104], R.J. Ward[20], N. Warrack[59], A. T. Watson[20], H. Watson[59], M. F. Watson[20], E. Watton[59,134], G. Watts[138], B. M. Waugh[96], C. Weber[29], H. A. Weber[18], M. S. Weber[19], S. M. Weber[63a], C. Wei[62a], Y. Wei[126], A. R. Weidberg[126], E. J. Weik[117], J. Weingarten[49], M. Weirich[100], C. Weiser[54], C. J. Wells[48], T. Wenaus[29], B. Wendland[49], T. Wengler[36], N. S. Wenke[110], N. Wermes[24], M. Wessels[63a], A. M. Wharton[91], A. S. White[61], A. White[8], M. J. White[1], D. Whiteson[160], L. Wickremasinghe[124], W. Wiedenmann[170], C. Wiel[50], M. Wielers[134], C. Wiglesworth[42], D. J. Wilbern[120], H. G. Wilkens[36], D. M. Williams[41], H. H. Williams[128], S. Williams[32], S. Willocq[103], B. J. Wilson[101], P. J. Windischhofer[39], F. I. Winkel[30], F. Winklmeier[123], B. T. Winter[54], J. K. Winter[101], M. Wittgen[143], M. Wobisch[97], Z. Wolffs[114], J. Wollrath[160], M. W. Wolter[87], H. Wolters[130a,130c], A. F. Wongel[48], S. D. Worm[48], B. K. Wosiek[87], K. W. Woźniak[87], S. Wozniewski[55], K. Wraight[59], C. Wu[20], J. Wu[14a,14e], M. Wu[64a], M. Wu[113], S. L. Wu[170], X. Wu[56], Y. Wu[62a], Z. Wu[135], J. Wuerzinger[110,af], T. R. Wyatt[101], B. M. Wynne[52], S. Xella[42], L. Xia[14c], M. Xia[14b], J. Xiang[64c], M. Xie[62a], X. Xie[62a], S. Xin[14a,14e], A. Xiong[123], J. Xiong[17a], D. Xu[14a], H. Xu[62a], L. Xu[62a], R. Xu[128], T. Xu[106], Y. Xu[14b], Z. Xu[52], Z. Xu[14a], B. Yabsley[147], S. Yacoob[33a], Y. Yamaguchi[154], E. Yamashita[153], H. Yamauchi[157], T. Yamazaki[17a], Y. Yamazaki[85], J. Yan[62c], S. Yan[126], Z. Yan[25], H. J. Yang[62c,62d], H. T. Yang[62a], S. Yang[62a], T. Yang[64c], X. Yang[62a], X. Yang[14a], Y. Yang[44], Y. Yang[62a], Z. Yang[62a], W.-M. Yao[17a], Y. C. Yap[48], H. Ye[14c], H. Ye[55], J. Ye[14a], S. Ye[29], X. Ye[62a], Y. Yeh[96], I. Yeletskikh[38], B. Yeo[17b], M. R. Yexley[96], P. Yin[41], K. Yorita[168], S. Younas[27b], C. J. S. Young[36], C. Young[143], C. Yu[14a,14e], Y. Yu[62a], M. Yuan[106], R. Yuan[62b], L. Yue[96], M. Zaazoua[62a], B. Zabinski[87], E. Zaid[52], T. Zakareishvili[149b], N. Zakharchuk[34], S. Zambito[56], J. A. Zamora Saa[137b,137d], J. Zang[153], D. Zanzi[54], O. Zaplatilek[132], C. Zeitnitz[171], H. Zeng[14a], J. C. Zeng[162], D. T. Zenger Jr[26], O. Zenin[37], T. Ženiš[28a], S. Zenz[94], S. Zerradi[35a], D. Zerwas[66], M. Zhai[14a,14e], B. Zhang[14c], D. F. Zhang[139], J. Zhang[62b], J. Zhang[6], K. Zhang[14a,14e], L. Zhang[14c], P. Zhang[14a,14e], R. Zhang[170], S. Zhang[106], T. Zhang[153], X. Zhang[62c], X. Zhang[62b], Y. Zhang[62c,5], Y. Zhang[96], Z. Zhang[17a], Z. Zhang[66], H. Zhao[138], P. Zhao[51], T. Zhao[62b], Y. Zhao[136], Z. Zhao[62a], A. Zhemchugov[38], J. Zheng[14c], K. Zheng[162], X. Zheng[62a], Z. Zheng[143], D. Zhong[162], B. Zhou[106], H. Zhou[7], N. Zhou[62c], Y. Zhou[7], C. G. Zhu[62b], J. Zhu[106], Y. Zhu[62c], Y. Zhu[62a], X. Zhuang[14a], K. Zhukov[37], V. Zhulanov[37], N. I. Zimine[38], J. Zinsser[63b], M. Ziolkowski[141], L. Živković[15], A. Zoccoli[23a,23b], K. Zoch[61], T. G. Zorbas[139], O. Zormpa[46], W. Zou[41], L. Zwalinski[36]

[1] Department of Physics, University of Adelaide, Adelaide, Australia

[2] Department of Physics, University of Alberta, Edmonton, AB, Canada

[3] (a)Department of Physics, Ankara University, Ankara, Turkey; (b)Division of Physics, TOBB University of Economics and Technology, Ankara, Turkey

[4] LAPP, Université Savoie Mont Blanc, CNRS/IN2P3, Annecy, France

[5] APC, Université Paris Cité, CNRS/IN2P3, Paris, France

[6] High Energy Physics Division, Argonne National Laboratory, Argonne, IL, USA

[7] Department of Physics, University of Arizona, Tucson, AZ, USA

[8] Department of Physics, University of Texas at Arlington, Arlington, TX, USA

[9] Physics Department, National and Kapodistrian University of Athens, Athens, Greece

[10] Physics Department, National Technical University of Athens, Zografou, Greece

[11] Department of Physics, University of Texas at Austin, Austin, TX, USA

[12] Institute of Physics, Azerbaijan Academy of Sciences, Baku, Azerbaijan

[13] Institut de Física d'Altes Energies (IFAE), Barcelona Institute of Science and Technology, Barcelona, Spain

[14] [a]Institute of High Energy Physics, Chinese Academy of Sciences, Beijing, China; [b]Physics Department, Tsinghua University, Beijing, China; [c]Department of Physics, Nanjing University, Nanjing, China; [d]School of Science, Shenzhen Campus of Sun Yat-sen University, Guangzhou, China; [e]University of Chinese Academy of Science (UCAS), Beijing, China

[15] Institute of Physics, University of Belgrade, Belgrade, Serbia

[16] Department for Physics and Technology, University of Bergen, Bergen, Norway

[17] [a]Physics Division, Lawrence Berkeley National Laboratory, Berkeley, CA, USA; [b]University of California, Berkeley, CA, USA

[18] Institut für Physik, Humboldt Universität zu Berlin, Berlin, Germany

[19] Albert Einstein Center for Fundamental Physics and Laboratory for High Energy Physics, University of Bern, Bern, Switzerland

[20] School of Physics and Astronomy, University of Birmingham, Birmingham, UK

[21] [a]Department of Physics, Bogazici University, Istanbul, Turkey; [b]Department of Physics Engineering, Gaziantep University, Gaziantep, Turkey; [c]Department of Physics, Istanbul University, Istanbul, Turkey

[22] [a]Facultad de Ciencias y Centro de Investigaciónes, Universidad Antonio Nariño, Bogotá, Colombia; [b]Departamento de Física, Universidad Nacional de Colombia, Bogotá, Colombia

[23] [a]Dipartimento di Fisica e Astronomia A. Righi, Università di Bologna, Bologna, Italy; [b]INFN Sezione di Bologna, Bologna, Italy

[24] Physikalisches Institut, Universität Bonn, Bonn, Germany

[25] Department of Physics, Boston University, Boston, MA, USA

[26] Department of Physics, Brandeis University, Waltham, MA, USA

[27] [a]Transilvania University of Brasov, Brasov, Romania; [b]Horia Hulubei National Institute of Physics and Nuclear Engineering, Bucharest, Romania; [c]Department of Physics, Alexandru Ioan Cuza University of Iasi, Iasi, Romania; [d]National Institute for Research and Development of Isotopic and Molecular Technologies, Physics Department, Cluj-Napoca, Romania; [e]National University of Science and Technology Politechnica, Bucharest, Romania; [f]West University in Timisoara, Timisoara, Romania; [g]Faculty of Physics, University of Bucharest, Bucharest, Romania

[28] [a]Faculty of Mathematics, Physics and Informatics, Comenius University, Bratislava, Slovak Republic; [b]Department of Subnuclear Physics, Institute of Experimental Physics of the Slovak Academy of Sciences, Kosice, Slovak Republic

[29] Physics Department, Brookhaven National Laboratory, Upton, NY, USA

[30] Universidad de Buenos Aires, Facultad de Ciencias Exactas y Naturales, Departamento de Física, y CONICET, Instituto de Física de Buenos Aires (IFIBA), Buenos Aires, Argentina

[31] California State University, Los Angeles, CA, USA

[32] Cavendish Laboratory, University of Cambridge, Cambridge, UK

[33] [a]Department of Physics, University of Cape Town, Cape Town, South Africa; [b]iThemba Labs, Western Cape, South Africa; [c]Department of Mechanical Engineering Science, University of Johannesburg, Johannesburg, South Africa; [d]National Institute of Physics, University of the Philippines Diliman, Philippines, South Africa; [e]Department of Physics, University of South Africa, Pretoria, South Africa; [f]University of Zululand, KwaDlangezwa, South Africa; [g]School of Physics, University of the Witwatersrand, Johannesburg, South Africa

[34] Department of Physics, Carleton University, Ottawa, ON, Canada

[35] [a]Faculté des Sciences Ain Chock, Université Hassan II de Casablanca, Casablanca, Morocco; [b]Faculté des Sciences, Université Ibn-Tofail, Kénitra, Morocco; [c]Faculté des Sciences Semlalia, Université Cadi Ayyad, LPHEA, Marrakech, Morocco; [d]LPMR, Faculté des Sciences, Université Mohamed Premier, Oujda, Morocco; [e]Faculté des sciences, Université Mohammed V, Rabat, Morocco; [f]Institute of Applied Physics, Mohammed VI Polytechnic University, Ben Guerir, Morocco

[36] CERN, Geneva, Switzerland

[37] Affiliated with an Institute Covered by a Cooperation Agreement with CERN, Geneva, Switzerland

[38] Affiliated with an International Laboratory Covered by a Cooperation Agreement with CERN, Geneva, Switzerland

[39] Enrico Fermi Institute, University of Chicago, Chicago, IL, USA

[40] LPC, Université Clermont Auvergne, CNRS/IN2P3, Clermont-Ferrand, France

[41] Nevis Laboratory, Columbia University, Irvington, NY, USA

[42] Niels Bohr Institute, University of Copenhagen, Copenhagen, Denmark

[43] (a)Dipartimento di Fisica, Università della Calabria, Rende, Italy; (b)INFN Gruppo Collegato di Cosenza, Laboratori Nazionali di Frascati, Frascati, Italy

[44] Physics Department, Southern Methodist University, Dallas, TX, USA

[45] Physics Department, University of Texas at Dallas, Richardson, TX, USA

[46] National Centre for Scientific Research "Demokritos", Agia Paraskevi, Greece

[47] (a)Department of Physics, Stockholm University, Stockholm, Sweden; (b)Oskar Klein Centre, Stockholm, Sweden

[48] Deutsches Elektronen-Synchrotron DESY, Hamburg and Zeuthen, Germany

[49] Fakultät Physik , Technische Universität Dortmund, Dortmund, Germany

[50] Institut für Kern- und Teilchenphysik, Technische Universität Dresden, Dresden, Germany

[51] Department of Physics, Duke University, Durham, NC, USA

[52] SUPA-School of Physics and Astronomy, University of Edinburgh, Edinburgh, UK

[53] INFN e Laboratori Nazionali di Frascati, Frascati, Italy

[54] Physikalisches Institut, Albert-Ludwigs-Universität Freiburg, Freiburg, Germany

[55] II. Physikalisches Institut, Georg-August-Universität Göttingen, Göttingen, Germany

[56] Département de Physique Nucléaire et Corpusculaire, Université de Genève, Geneva, Switzerland

[57] (a)Dipartimento di Fisica, Università di Genova, Geneva, Italy; (b)INFN Sezione di Genova, Geneva, Italy

[58] II. Physikalisches Institut, Justus-Liebig-Universität Giessen, Giessen, Germany

[59] SUPA-School of Physics and Astronomy, University of Glasgow, Glasgow, UK

[60] LPSC, Université Grenoble Alpes, CNRS/IN2P3, Grenoble INP, Grenoble, France

[61] Laboratory for Particle Physics and Cosmology, Harvard University, Cambridge, MA, USA

[62] (a)Department of Modern Physics and State Key Laboratory of Particle Detection and Electronics, University of Science and Technology of China, Hefei, China; (b)Institute of Frontier and Interdisciplinary Science and Key Laboratory of Particle Physics and Particle Irradiation (MOE), Shandong University, Qingdao, China; (c)School of Physics and Astronomy, Shanghai Jiao Tong University, Key Laboratory for Particle Astrophysics and Cosmology (MOE), SKLPPC, Shanghai, China; (d)Tsung-Dao Lee Institute, Shanghai, China

[63] (a)Kirchhoff-Institut für Physik, Ruprecht-Karls-Universität Heidelberg, Heidelberg, Germany; (b)Physikalisches Institut, Ruprecht-Karls-Universität Heidelberg, Heidelberg, Germany

[64] (a)Department of Physics, Chinese University of Hong Kong, Shatin, N.T., Hong Kong, China; (b)Department of Physics, University of Hong Kong, Pok Fu Lam, Hong Kong, China; (c)Department of Physics and Institute for Advanced Study, Hong Kong University of Science and Technology, Clear Water Bay, Kowloon, Hong Kong, China

[65] Department of Physics, National Tsing Hua University, Hsinchu, Taiwan

[66] IJCLab, Université Paris-Saclay, CNRS/IN2P3, 91405, Orsay, France

[67] Centro Nacional de Microelectrónica (IMB-CNM-CSIC), Barcelona, Spain

[68] Department of Physics, Indiana University, Bloomington, IN, USA

[69] (a)INFN Gruppo Collegato di Udine, Sezione di Trieste, Udine, Italy; (b)ICTP, Trieste, Italy; (c)Dipartimento Politecnico di Ingegneria e Architettura, Università di Udine, Udine, Italy

[70] (a)INFN Sezione di Lecce, Lecce, Italy; (b)Dipartimento di Matematica e Fisica, Università del Salento, Lecce, Italy

[71] (a)INFN Sezione di Milano, Milan, Italy; (b)Dipartimento di Fisica, Università di Milano, Milan, Italy

[72] (a)INFN Sezione di Napoli, Naples, Italy; (b)Dipartimento di Fisica, Università di Napoli, Naples, Italy

[73] (a)INFN Sezione di Pavia, Pavia, Italy; (b)Dipartimento di Fisica, Università di Pavia, Pavia, Italy

[74] (a)INFN Sezione di Pisa, Pisa, Italy; (b)Dipartimento di Fisica E. Fermi, Università di Pisa, Pisa, Italy

[75] (a)INFN Sezione di Roma, Rome, Italy; (b)Dipartimento di Fisica, Sapienza Università di Roma, Rome, Italy

[76] (a)INFN Sezione di Roma Tor Vergata, Rome, Italy; (b)Dipartimento di Fisica, Università di Roma Tor Vergata, Rome, Italy

[77] (a)INFN Sezione di Roma Tre, Rome, Italy; (b)Dipartimento di Matematica e Fisica, Università Roma Tre, Rome, Italy

[78] (a)INFN-TIFPA, Povo, Italy; (b)Università degli Studi di Trento, Trento, Italy

[79] Universität Innsbruck, Department of Astro and Particle Physics, Innsbruck, Austria

[80] University of Iowa, Iowa City, IA, USA

[81] Department of Physics and Astronomy, Iowa State University, Ames, IA, USA

[82] Istinye University, Sariyer, Istanbul, Turkey

[83] (a)Departamento de Engenharia Elétrica, Universidade Federal de Juiz de Fora (UFJF), Juiz de Fora, Brazil; (b)Universidade Federal do Rio De Janeiro COPPE/EE/IF, Rio de Janeiro, Brazil; (c)Instituto de Física, Universidade de São Paulo, São Paulo, Brazil; (d)Rio de Janeiro State University, Rio de Janeiro, Brazil

[84] KEK, High Energy Accelerator Research Organization, Tsukuba, Japan

[85] Graduate School of Science, Kobe University, Kobe, Japan

[86] (a)Faculty of Physics and Applied Computer Science, AGH University of Krakow, Krakow, Poland; (b)Marian Smoluchowski Institute of Physics, Jagiellonian University, Krakow, Poland

[87] Institute of Nuclear Physics Polish Academy of Sciences, Krakow, Poland

[88] Faculty of Science, Kyoto University, Kyoto, Japan

[89] Research Center for Advanced Particle Physics and Department of Physics, Kyushu University, Fukuoka , Japan

[90] Instituto de Física La Plata, Universidad Nacional de La Plata and CONICET, La Plata, Argentina

[91] Physics Department, Lancaster University, Lancaster, UK

[92] Oliver Lodge Laboratory, University of Liverpool, Liverpool, UK

[93] Department of Experimental Particle Physics, Jožef Stefan Institute and Department of Physics, University of Ljubljana, Ljubljana, Slovenia

[94] School of Physics and Astronomy, Queen Mary University of London, London, UK

[95] Department of Physics, Royal Holloway University of London, Egham, UK

[96] Department of Physics and Astronomy, University College London, London, UK

[97] Louisiana Tech University, Ruston, LA, USA

[98] Fysiska institutionen, Lunds universitet, Lund, Sweden

[99] Departamento de Física Teorica C-15 and CIAFF, Universidad Autónoma de Madrid, Madrid, Spain

[100] Institut für Physik, Universität Mainz, Mainz, Germany

[101] School of Physics and Astronomy, University of Manchester, Manchester, UK

[102] CPPM, Aix-Marseille Université, CNRS/IN2P3, Marseille, France

[103] Department of Physics, University of Massachusetts, Amherst, MA, USA

[104] Department of Physics, McGill University, Montreal, QC, Canada

[105] School of Physics, University of Melbourne, Victoria, Australia

[106] Department of Physics, University of Michigan, Ann Arbor, MI, USA

[107] Department of Physics and Astronomy, Michigan State University, East Lansing, MI, USA

[108] Group of Particle Physics, University of Montreal, Montreal, QC, Canada

[109] Fakultät für Physik, Ludwig-Maximilians-Universität München, München, Germany

[110] Max-Planck-Institut für Physik (Werner-Heisenberg-Institut), Munich, Germany

[111] Graduate School of Science and Kobayashi-Maskawa Institute, Nagoya University, Nagoya, Japan

[112] Department of Physics and Astronomy, University of New Mexico, Albuquerque, NM, USA

[113] Institute for Mathematics, Astrophysics and Particle Physics, Radboud University/Nikhef, Nijmegen, The Netherlands

[114] Nikhef National Institute for Subatomic Physics and University of Amsterdam, Amsterdam, The Netherlands

[115] Department of Physics, Northern Illinois University, DeKalb, IL, USA

[116] (a)New York University Abu Dhabi, Abu Dhabi, United Arab Emirates; (b)University of Sharjah, Sharjah, United Arab Emirates

[117] Department of Physics, New York University, New York, NY, USA

[118] Ochanomizu University, Otsuka, Bunkyo-ku, Tokyo, Japan

[119] Ohio State University, Columbus, OH, USA

[120] Homer L. Dodge Department of Physics and Astronomy, University of Oklahoma, Norman, OK, USA

[121] Department of Physics, Oklahoma State University, Stillwater, OK, USA

[122] Palacký University, Joint Laboratory of Optics, Olomouc, Czech Republic

[123] Institute for Fundamental Science, University of Oregon, Eugene, OR, USA

[124] Graduate School of Science, Osaka University, Osaka, Japan

[125] Department of Physics, University of Oslo, Oslo, Norway

[126] Department of Physics, Oxford University, Oxford, UK

[127] LPNHE, Sorbonne Université, Université Paris Cité, CNRS/IN2P3, Paris, France

[128] Department of Physics, University of Pennsylvania, Philadelphia, PA, USA

[129] Department of Physics and Astronomy, University of Pittsburgh, Pittsburgh, PA, USA

[130] [a]Laboratório de Instrumentação e Física Experimental de Partículas-LIP, Lisbon, Portugal; [b]Departamento de Física, Faculdade de Ciências, Universidade de Lisboa, Lisbon, Portugal; [c]Departamento de Física, Universidade de Coimbra, Coimbra, Portugal; [d]Centro de Física Nuclear da Universidade de Lisboa, Lisbon, Portugal; [e]Departamento de Física, Universidade do Minho, Braga, Portugal; [f]Departamento de Física Teórica y del Cosmos, Universidad de Granada, Granada, Spain; [g]Departamento de Física, Instituto Superior Técnico, Universidade de Lisboa, Lisbon, Portugal

[131] Institute of Physics of the Czech Academy of Sciences, Prague, Czech Republic

[132] Czech Technical University in Prague, Prague, Czech Republic

[133] Charles University, Faculty of Mathematics and Physics, Prague, Czech Republic

[134] Particle Physics Department, Rutherford Appleton Laboratory, Didcot, UK

[135] IRFU, CEA, Université Paris-Saclay, Gif-sur-Yvette, France

[136] Santa Cruz Institute for Particle Physics, University of California Santa Cruz, Santa Cruz, CA, USA

[137] [a]Departamento de Física, Pontificia Universidad Católica de Chile, Santiago, Chile; [b]Millennium Institute for Subatomic Physics at High Energy Frontier (SAPHIR), Santiago, Chile; [c]Instituto de Investigación Multidisciplinario en Ciencia y Tecnología, y Departamento de Física, Universidad de La Serena, La Serena, Chile; [d]Department of Physics, Universidad Andres Bello, Santiago, Chile; [e]Instituto de Alta Investigación, Universidad de Tarapacá, Arica, Chile; [f]Departamento de Física, Universidad Técnica Federico Santa María, Valparaíso, Chile

[138] Department of Physics, University of Washington, Seattle, WA, USA

[139] Department of Physics and Astronomy, University of Sheffield, Sheffield, UK

[140] Department of Physics, Shinshu University, Nagano, Japan

[141] Department Physik, Universität Siegen, Siegen, Germany

[142] Department of Physics, Simon Fraser University, Burnaby, BC, Canada

[143] SLAC National Accelerator Laboratory, Stanford, CA, USA

[144] Department of Physics, Royal Institute of Technology, Stockholm, Sweden

[145] Department of Physics and Astronomy, Stony Brook University, Stony Brook, NY, USA

[146] Department of Physics and Astronomy, University of Sussex, Brighton, UK

[147] School of Physics, University of Sydney, Sydney, Australia

[148] Institute of Physics, Academia Sinica, Taipei, Taiwan

[149] [a]E. Andronikashvili Institute of Physics, Iv. Javakhishvili Tbilisi State University, Tbilisi, Georgia; [b]High Energy Physics Institute, Tbilisi State University, Tbilisi, Georgia; [c]University of Georgia, Tbilisi, Georgia

[150] Department of Physics, Technion, Israel Institute of Technology, Haifa, Israel

[151] Raymond and Beverly Sackler School of Physics and Astronomy, Tel Aviv University, Tel Aviv, Israel

[152] Department of Physics, Aristotle University of Thessaloniki, Thessaloniki, Greece

[153] International Center for Elementary Particle Physics and Department of Physics, University of Tokyo, Tokyo, Japan

[154] Department of Physics, Tokyo Institute of Technology, Tokyo, Japan

[155] Department of Physics, University of Toronto, Toronto, ON, Canada

[156] [a]TRIUMF, Vancouver, BC, Canada; [b]Department of Physics and Astronomy, York University, Toronto, ON, Canada

[157] Division of Physics and Tomonaga Center for the History of the Universe, Faculty of Pure and Applied Sciences, University of Tsukuba, Tsukuba, Japan

[158] Department of Physics and Astronomy, Tufts University, Medford, MA, USA

[159] United Arab Emirates University, Al Ain, United Arab Emirates

[160] Department of Physics and Astronomy, University of California Irvine, Irvine, CA, USA

[161] Department of Physics and Astronomy, University of Uppsala, Uppsala, Sweden

[162] Department of Physics, University of Illinois, Urbana, IL, USA

[163] Instituto de Física Corpuscular (IFIC), Centro Mixto Universidad de Valencia-CSIC, Valencia, Spain

[164] Department of Physics, University of British Columbia, Vancouver, BC, Canada

[165] Department of Physics and Astronomy, University of Victoria, Victoria, BC, Canada

[166] Fakultät für Physik und Astronomie, Julius-Maximilians-Universität Würzburg, Würzburg, Germany

[167] Department of Physics, University of Warwick, Coventry, UK

[168] Waseda University, Tokyo, Japan

[169] Department of Particle Physics and Astrophysics, Weizmann Institute of Science, Rehovot, Israel

[170] Department of Physics, University of Wisconsin, Madison, WI, USA

[171] Fakultät für Mathematik und Naturwissenschaften, Fachgruppe Physik, Bergische Universität Wuppertal, Wuppertal, Germany

[172] Department of Physics, Yale University, New Haven, CT, USA

[a] Also Affiliated with an Institute Covered by a Cooperation Agreement with CERN, Geneva, Switzerland

[b] Also at An-Najah National University, Nablus, Palestine

[c] Also at Borough of Manhattan Community College, City University of New York, New York, NY, USA

[d] Also at Center for High Energy Physics, Peking University, Beijing, China

[e] Also at Center for Interdisciplinary Research and Innovation (CIRI-AUTH), Thessaloniki, Greece

[f] Also at Centro Studi e Ricerche Enrico Fermi, Rome, Italy

[g] Also at CERN, Geneva, Switzerland

[h] Also at Département de Physique Nucléaire et Corpusculaire, Université de Genève, Geneva, Switzerland

[i] Also at Departament de Fisica de la Universitat Autonoma de Barcelona, Barcelona, Spain

[j] Also at Department of Financial and Management Engineering, University of the Aegean, Chios, Greece

[k] Also at Department of Physics, Ben Gurion University of the Negev, Beer Sheva, Israel

[l] Also at Department of Physics, California State University, Sacramento, USA

[m] Also at Department of Physics, King's College London, London, UK

[n] Also at Department of Physics, Stanford University, Stanford, CA, USA

[o] Also at Department of Physics, University of Fribourg, Fribourg, Switzerland

[p] Also at Department of Physics, University of Thessaly, Volos, Greece

[q] Also at Department of Physics, Westmont College, Santa Barbara, USA

[r] Also at Faculty of Physics, Sofia University, St. Kliment Ohridski, Sofia, Bulgaria

[s] Also at Hellenic Open University, Patras, Greece

[t] Also at Institucio Catalana de Recerca i Estudis Avancats, ICREA, Barcelona, Spain

[u] Also at Institut für Experimentalphysik, Universität Hamburg, Hamburg, Germany

[v] Also at Institute for Nuclear Research and Nuclear Energy (INRNE) of the Bulgarian Academy of Sciences, Sofia, Bulgaria

[w] Also at Institute of Applied Physics, Mohammed VI Polytechnic University, Ben Guerir, Morocco

[x] Also at Institute of Particle Physics (IPP), Toronto, Canada

[y] Also at Institute of Physics and Technology, Mongolian Academy of Sciences, Ulaanbaatar, Mongolia

[z] Also at Institute of Physics, Azerbaijan Academy of Sciences, Baku, Azerbaijan

[aa] Also at Institute of Theoretical Physics, Ilia State University, Tbilisi, Georgia

[ab] Also at L2IT, Université de Toulouse, CNRS/IN2P3, UPS, Toulouse, France

[ac] Also at Lawrence Livermore National Laboratory, Livermore, USA

[ad] Also at National Institute of Physics, University of the Philippines Diliman, Philippines, Philippines

[ae] Also at Ochanomizu University, Bunkyo-ku, Otsuka, Tokyo, Japan

[af] Also at Technical University of Munich, Munich, Germany

[ag] Also at The Collaborative Innovation Center of Quantum Matter (CICQM), Beijing, China

[ah] Also at TRIUMF, Vancouver, BC, Canada

[ai] Also at Università di Napoli Parthenope, Naples, Italy

[aj] Department of Physics, Also at University of Colorado Boulder, Colorado, USA

[ak] Also at Washington College, Chestertown, MD, USA

[al] Also at Yeditepe University, Physics Department, Istanbul, Turkey

 * Deceased